Nonequilibrium exciton physics in hybrid lead-halide perovskites and anatase titanium dioxide

Thèse N° 9216

Présentée le 22 février 2019

à la Faculté des sciences de base
Laboratoire de spectroscopie ultrarapide
Programme doctoral en photonique

pour l'obtention du grade de Docteur ès Sciences

par

TANIA PALMIERI

Acceptée sur proposition du jury

Prof. N. Grandjean, président du jury
Prof. M. Chergui, directeur de thèse
Prof. M. Saba, rapporteur
Dr A. Petrozza, rapporteuse
Prof. A. Hagfeldt, rapporteur

2019

ÉCOLE POLYTECHNIQUE
FÉDÉRALE DE LAUSANNE

Acknowledgements

Contrary to popular belief, only a little piece of what we call “the PhD” is made of the degree you are awarded after writing and defending the thesis. These are only the last steps of a long life-changing path, during which you learn to be a scientist, but also to fight and overcome your own weaknesses day after day. These pages contain several sentences, formulas, and graphs, meant to embody four years of scientific research. What cannot be printed on a page is instead the trace of all the people that, one way or the other, contributed to this achievement.

The first person I would like to thank is Prof Majed Chergui, my thesis advisor, because he was able to radiate enthusiasm and positiveness even during the hardest moments. Something important I have learnt from Majed is that a scientific exchange is always an opportunity to teach and learn something new, regardless the roles or the different years of experience. This is why I feel privileged, because I always knew I was working *with* him, rather than *for* him.
Special thanks also go to Edoardo, because his dedication and enthusiasm made everything thrilling. His contribution to my growth in all these years is priceless.
My PhD has been also a unique opportunity to collaborate with many other excellent scientists. I would like to acknowledge Dr Giulia Grancini for being such an inspiring scientist, and for all our discussions which mainly took place on a train to Milan. I am also very grateful to Dr Endre Horvath and Dr Marton Kollar, who had the patience to grow the most beautiful perovskite crystals for my experiments; Prof Angel Rubio, Dr Adriel Dominguez, Prof Pascal Ruello and Dr Alexander Steinhoff, for their enthusiastic involvement in the projects and the precious discussion.
Many thanks also to Dr Frank Van Mourik, probably the best laser therapist on Earth, for sharing with me the secrets of femtosecond lasers and for his invaluable help during the darkest days of the setup.

My colleagues from LSU deserve a special mention, because we have always made our best to create a friendly work environment, taking good care of each other. Michele had the “great honour” of sharing the office with me during the last (and probably the hardest) year. Thanks for being the wise friend who explains me how real life works (on the top of his long-standing experience). Thanks to Malte for listening to me and cheering me up in many blue moments. To Luca and Oliviero for keeping the italianness levels very high and make me feel home. To Ben, Lars, Thomas R., Thomas B., Rebecca, Francesco, Dominik, Serhii, Natalia, Lijie, Giulia,

Annick, and to all the LSU people who left and with whom I shared work, words and moments. During these years, I have had the unique opportunity of being part of the EPFL Photonics Chapter. This was my first experience in an association, and I want to thank all the people I worked with, for sharing all the management-related stress but also for so many cheers after successful events.

Lovely memories are related to all the people I have met outside the working hours. Starting from Sara and Stefania, the very first friends I have made just arrived in Lausanne, and I'm so glad that our friendship survived the distance and brought us close again. It is impossible to make an exhaustive list of people who crossed my life here: Giulia, Eirini, Lea, Gloria, Ghil, Enri-ginger, Hana, Fede, Gigi, Alberto, Davide, Michela, Nicole, Giulia, Ema, Riccardo, Gianluca, Ketki, ... and those who were still there for me in Italy: Marzia, Pando, Luca, Alberto, Elena, Lus, Andrea... and to everyone I haven't mentioned but with whom I shared beers, dinners, hikes, lakes, ski trips, moments, secrets, who brought something good to my life and made me feel (almost) home.

Thanks to M. for blowing confetti on my hair everyday and for all the little things of which he is not aware.

All my achievements would have never been possible without the love of my family. Thanks for always believing in me and being so close despite the distance.
Arrivare fin qui non sarebbe stato possibile senza l'amore della mia famiglia. Grazie per aver creduto in me e per essere stati sempre cosi vicini nonostante la distanza.

Lausanne, 1st November 2018 T. P.

Abstract

The strength of the electron-hole interaction in bulk semiconductors is not only determined by the dielectric environment, but also depends on the presence of other quasiparticles - free charge carriers or phonons - that populate the system. In the former case, a high density of charge carriers is expected to screen the Coulomb attractive force, eventually driving the transition from an insulating exciton gas to a conductive electron-hole plasma. In the case of lattice vibrations, the coupling between the exciton and the phonon field can give rise to significant modulations of the exciton amplitude and binding energy. Understanding how excitons react to these perturbations is of pivotal importance, as the strength of the Coulomb interaction affects the way light is absorbed and emitted, and determines how energy is converted and transported in several optoelectronic technologies.

The aim of this thesis is to investigate the nonequilibrium exciton physics in highly-excited semiconductors. For this scope, we will combine different steady-state and ultrafast optical techniques, spectro-temporal analysis, and advanced theory calculations, with the aim of investigating the fundamental processes that lead to the renormalization of the excitonic states in hybrid lead-halide perovskites and titanium dioxide.

In our experiments, we use an ultrashort laser pulse to excite the system above the fundamental energy gap; a broadband pulse then monitors the optical properties in the exciton spectral region at different time delays upon photoexcitation. The temporal evolution of the exciton parameters are retrieved via quantitative lineshape analysis, which is achieved by modelling the steady-state optical quantities and combining them with the time-resolved spectra.

Thanks to this approach, we are able to elucidate the dynamics of exciton renormalization in hybrid perovskites and titanium dioxide in presence of elevated carrier densities and coherent strain pulses, and disentangle the many-body effects that lye at the origin of the observed optical nonlinearities.

Keywords: Ultrafast optical spectroscopy, excitons, Mott transition, exciton-phonon coupling, hybrid lead-halide perovskites, titanium dioxide.

Sommario

La forza dell'interazione elettrone-lacuna nei semiconduttori è determinata non solo dalle proprietà dielettriche del materiale, ma anche dalla presenza di altre quasiparticelle - portatori di carica e fononi - che popolano il sistema. Nel primo caso, alte densità di portatori possono schermare la forza attrattiva di Coulomb e indurre la transizione da un gas eccitonico isolante ad un plasma conduttivo di elettroni e lacune. Nel caso di vibrazioni reticolari, l'accoppiamento tra gli eccitoni e il campo fononico può causare notevoli modulazioni in ampiezza ed energia dell'eccitone. Comprendere come gli eccitoni reagiscono a queste perturbazioni è di importanza cruciale, in quanto la forza dell'interazione influenza come la luce venga assorbita ed emessa, e determina le modalità di conversione e trasporto dell'energia in molte tecnologie optoelettroniche.

L'obiettivo di questa tesi è lo studio della fisica eccitonica al nonequilibrio in semiconduttori fortemente fotoeccitati. A questo scopo, verranno combinate tecniche ottiche statiche e risolte in tempo, analisi spettro-temporale e calcoli teorici avanzati per investigare i processi fondamentali che portano alla rinormalizzazione degli stati eccitonici in perovskiti ibride e diossido di titanio.

Nei nostri esperimenti, un impulso laser ultracorto viene utilizzato per eccitare il sistema ad energie superiori al bandgap; successivamente, un secondo impulso a banda larga monitora le proprietà ottiche del materiale nella regione spettrale dell'eccitone a tempi diversi dopo l'eccitazione. L'evoluzione temporale dell'eccitone viene quantificata attraverso l'analisi spettrale, nella quale le quantità ottiche all'equilibrio vengono modellizzate e combinate con gli spettri risolti in tempo.

Questo approccio permette di fare luce sulla dinamica di rinormalizzazione degli stati eccitonici in perovskiti ibride e diossido di titanio in presenza di densità di carica elevate e di deformazione impulsata del materiale, isolando in maniera chiara gli effetti a molti corpi all'origine delle nonlinearità ottiche osservate.

Parole chiave: Spettroscopia ottica ultraveloce, eccitoni, transizione di Mott, accoppiamento eccitone-fonone, perovskiti ibride, diossido di titanio.

Contents

List of Figures

List of Tables

Introduction

Excitons are neutral quasiparticles that form in a material when a photoexcited electron (e) and hole (h) are attracted by each other *via* the Coulomb force. To some extent, these objects can be considered as the solid-state counterpart of the hydrogen atom, where the role of the proton is played by the hole, and the strength of e-h attraction is determined by the surrounding environment. The existence of such Coulomb interaction dictates the optoelectronic behaviour of low-dimensional systems, organic materials, or bulk semiconductors at sufficiently low temperatures. Here, the presence of excitonic states affects the way light is absorbed and emitted, and determines how energy is converted and transported.

The nature of the fundamental photoexcitations plays a central role when the material is implemented in a device. Clear examples are offered by solar energy conversion technologies, where the strength of e-h attraction determines the operation mechanism of the photovoltaic cell, or by light-emitting devices, where exciton recombination constitutes the main mechanism for light emission at low temperatures. From the fundamental point of view, excitons represent the ideal playground to explore novel quantum states of matter and investigate collective phenomena. This is the case for Bose-Einstein condensates, expected to form due to the bosonic nature of excitons, or for polaritons, hybrid light-matter quasiparticles arising from the strong coupling of excitons and phonons.

In the following pages, we focus on another fascinating aspect of excitons, that is their high sensitivity to the potential field of other quasiparticles - free charge carriers or phonons - that populate the system. In the former case, a large density of doped or photoinjected charge carriers can screen the e-h interaction and eventually trigger a phase transition from an insulating exciton gas to a conducting e-h plasma. In the case of lattice vibrations, the coupling between the exciton and the phonon field can give rise to significant modulations of the e-h interaction, an effect of great relevance for acousto-optic technologies.

A powerful tool for investigating the photophysical properties of semiconductors is represented by optical spectroscopy, as the two-particle excitation spectrum provides extensive information on light-matter interaction at the microscopic scale. However, in the scenario presented above, the optoelectronic properties of the material are no more determined by single e-h pairs. Instead, they are the result of a complex interplay between the populations of free charge carriers, excitons, and phonons. This interplay is usually established on a

timescale between few fs and tens of ps, simultaneous to the generation and relaxation of the nonequilibrium electronic and phononic distributions. Steady-state spectroscopies can provide only limited insights into these dynamic processes, as they are sensitive to time-averaged quantities. However, thanks to the advances in ultrafast lasers and optical techniques, the nonequilibrium properties of semiconductors can now be accessed with fs time-resolution by means of ultrafast optical spectroscopy. Within this approach, an ultrashort laser pulse sets the material out of equilibrium; the photoinduced changes in optical properties are then monitored at different time delays after the excitation by a probe pulse. When performed in a broadband fashion (*i.e.* covering a wide spectral region), a rich body of information can be accessed simultaneously in the time- and energy domains. In this way, the spectral fingerprint of each excitation can be readily recognized and disentangled in the transient optical spectrum.

Understanding the nonequilibrium exciton physics in highly-excited semiconductors represents the main objective of my thesis. I combine different steady-state and ultrafast optical techniques, spectro-temporal analysis, and advanced theory calculations, to investigate the fundamental processes that lead to the renormalization of the excitonic states in two classes of semiconductors, namely hybrid lead-halide perovskites and titanium dioxide (TiO_2).

Hybrid perovskites represent one of the most novel technologies for solar energy conversion. Thanks to the unique combination of low-cost solution processability, efficient charge transport, strong light absorption, and tunable optical properties, hybrid perovskites have become the main actors in photovoltaic research, and hold huge promises for optoelectronic applications. Another superior material for converting light into other forms of energy is anatase TiO_2. Although its photophysics boasts several decades of research, the nature of the excitonic interactions in TiO_2 is a recent discovery, that triggers and renews the interest towards the exciton physics in this wide-gap transition metal oxide.

The novelty of the research presented in this thesis is manifold. First, we make use of state-of-the-art ultrafast spectroscopies with broadband probe in the ultraviolet (UV) region, which give access to the dynamics of wide-gap insulators directly at the band edge. Thanks to these advances, the nonequilibrium exciton physics of TiO_2 and many other materials are investigated, which was not possible with the use of lower-energy optical spectroscopies. Moreover, we implement and apply an analytical method which allows to quantify with high precision the time-dependent changes in exciton oscillator strength, linewidth, and peak energy. To achieve this, we combine steady-state and time-resolved optical quantities, which are then described *via* a phenomenological model. The lineshape analysis greatly facilitates the interpretation of pump-probe data of semiconductors at the band edge, where the photoinduced spectral features originate from different sources of optical nonlinearities which act simultaneously upon light excitation. Within this approach, we are able to relate precisely the transient spectral features to the renormalization of the exciton parameters, and access the time evolution of any optical quantity of interest.

The structure of this thesis aims to guide the reader from the fundamental concepts on which we define our research question, to the details of the experimental methods, and to the results of our investigations.

Chapter 1 reviews the fundamental optical properties of bulk semiconductors in presence of interacting e-h pairs and the many-body effects at play in these materials in presence of high charge-carrier densities. Then, we explain how the dynamics of the fundamental photoexcitations in semiconductors can be investigated *via* ultrafast spectroscopy. Finally, we introduce the two materials that constitute the subject of our studies, hybrid organic-inorganic perovskites and anatase TiO_2, with a particular focus on the exciton physics.

Chapter 2 provides a brief overview on the experimental techniques and materials. Here, we present the technical details of the broadband transient reflectivity set-ups in the visible and UV regions used to study the ultrafast response of hybrid perovskites and anatase TiO_2 respectively. A brief description of the synthesis of these materials is presented.

In **Chapter 3**, we investigate exciton physics in single crystals of methylammonium lead bromide perovskites. We combine different experimental techniques, quantitative lineshape analysis, and state-of-the-art many-body theory to study the interplay between a photoexcited e-h plasma and the excitonic states in this material. We show that signatures of e-h correlations still persist in the response of single-crystals photoexcited above the nominal Mott density, where the complete exciton dissociation is expected, revealing the robustness of these collective excitations against high e-h densities.

Chapter 4 investigates the influence of many-body effects on the exciton states in anatase TiO_2 single crystals. In particular, we use ultrafast broadband UV spectroscopy to create a high density of e-h pairs and monitor the changes in optical properties, and compare the exciton renormalization dynamics in pristine and n-doped crystals. We observe that the photoexcited e-h plasma reduces the strength of e-h interaction via long-range Coulomb screening, while preventing the complete disappearance of the exciton lineshape.

In **Chapter 5**, we demonstrate how coherent strain pulses can modulate the exciton properties in anatase TiO_2 single crystals. By performing ultrafast broadband UV spectroscopy, we reveal the modulation of the exciton peak amplitude and a giant exciton shift due to coherent acoustic phonons launched by the pump pulse. We rely on advanced many-body perturbation theory calculations and study the influence of the coherent acoustic field onto the excitonic correlations, providing significant insights into the exciton-phonon coupling mechanism in this material.

1 Fundamentals

This Chapter presents the fundamental concepts on which we lay the foundations of this research work. Section 1.1 reviews the optical properties of bulk semiconductors in presence of interacting e-h pairs. In Section 1.2, we introduce the many-body effects at play in these materials in presence of high charge-carrier densities and their influence on the e-h interaction. The relaxation processes of photoexcited carriers and their investigation *via* ultrafast spectroscopy will be presented in Section 1.3. Finally, in Sections 1.4 and 1.5, we introduce the two classes of materials investigated in this thesis, namely hybrid organic-inorganic perovskites and anatase titanium dioxide, with a particular focus on the exciton physics in these systems.

1.1 Optical properties of bulk semiconductors

1.1.1 Free carrier absorption

In typical semiconductors, the absorption of a photon of energy $\hbar\omega > E_g$, E_g being the bandgap energy, promotes an electronic transition from the valence band (VB) to the conduction band (CB). The process of *interband absorption*, shown schematically in Figure 1.1, creates a hole (h^+) in the VB and an electron (e^-) in the conduction band. For momentum conservation laws, the e^- momentum does not change significantly during photon absorption, which translates into vertical transition in the $E-k$ diagram. In direct-gap semiconductors (Figure 1.1(a)), a photon energy $\hbar\omega = E_g$ is sufficient for interband transition, since the top of the VB and the bottom of the CB are found at $k = 0$. In indirect-gap materials, the process is possible only *via* the involvement of a phonon of momentum q, as depicted in Figure 1.1(b). Because of the involvement of a third particle, the probability of indirect transitions is significantly lower than direct ones; for this reason, the direct or indirect nature of the bandgap represents one of the most relevant parameter in semiconductor applications.

In a direct 3D semiconductor, the absorption coefficient $\alpha(\hbar\omega)$ can be calculated starting from two assumptions:

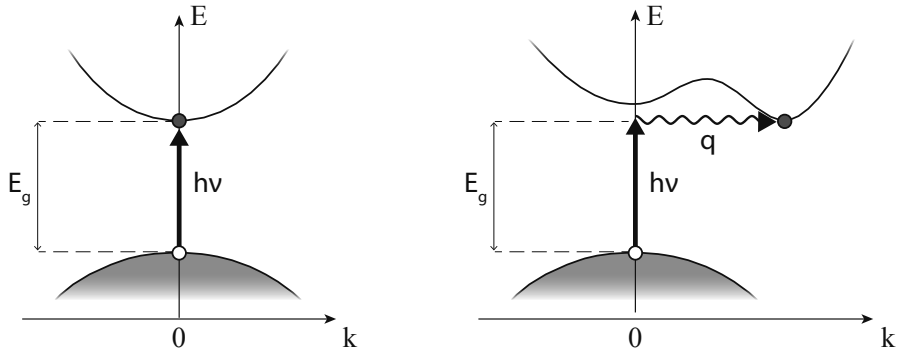

(a) direct bandgap (b) indirect bandgap

Figure 1.1 – Interband transitions in solids for (a) direct gap and (b) indirect gap. The vertical arrow represents photon absorption, the wiggled line represents phonon absorption or emission.

- the transition occurs between one VB and one CB (*two-band approximation*);
- in the vicinity of band extrema, the dispersion can be considered parabolic, which allows to treat the carriers as quasi-free particles characterized by an effective mass m_a^* (*effective mass approximation*):

$$m_{a,\text{eff}} = m_a^* = \hbar \left(\frac{\partial^2 E(\mathbf{k})}{\partial k^2}\bigg|_{k=0} \right)^{-1}, \qquad a = e, h \tag{1.1}$$

- the light excitation pulse is longer than the carrier scattering time, thus the carriers can be always be considered in thermal equilibrium among themselves (*quasi-equilibrium approximation*).

Under these approximations, and in case of a unexcited semiconductor, $\alpha(\omega)$[1] has the form [1]:

$$\alpha(\omega) = \alpha_0 \frac{\hbar\omega}{E_0} \left(\frac{\hbar\omega - E_g}{E_0} \right)^{1/2} \Theta\left(\hbar\omega - E_g\right) \tag{1.2}$$

In the equation, $\Theta\left(\hbar\omega - E_g\right)$ is the Heaviside function, while the term α_0 corresponds the prefactor of the joint density of states (DOS) for 3D crystals, defined by

$$\alpha_0 = \frac{4\pi^2 |d_{\text{cv}}|^2}{\hbar n_b c} \frac{4\pi}{(2\pi a_0)^3} = \frac{2|d_{\text{cv}}|^2}{\hbar n_b c} \frac{1}{{a_0}^3} \tag{1.3}$$

The energy E_0 and the length a_0 are scaling parameters:

$$E_0 = \frac{\hbar^2}{2 m_r {a_0}^2}, \qquad a_0 = \frac{\hbar^2 \epsilon_0}{e^2 m_r} \tag{1.4}$$

[1] The quantities are expressed in CGS units.

and m_r the e-h reduced mass:

$$\frac{1}{m_r} = \frac{1}{m_e^*} + \frac{1}{m_h^*}. \tag{1.5}$$

1.1.2 Excitons

Equation (1.2) describes the absorption properties of a semiconductor under the assumption that the photoexcited e-h pairs are *non-interacting*. Nevertheless, as the particles are generated in the same point in real space, they can attract each other *via* the Coulomb force and strongly modify the absorption properties of the material close to the absorption edge. The interacting e-h pair can be treated as a new quasiparticle, the *exciton*.

Classification

Depending on the spread of the wavefunction, excitonic quasiparticles are classified into different type of excitons [2], depicted in Figure 1.2.

- *Frenkel excitons* are localized states strongly bound to a specific atom or molecule (Figure 1.2(a)); their wavefunction is highly localized in space, usually restricted to a single unit cell. Frenkel excitons are usually found in molecular solids, in which they move *via* a hopping mechanism.
- *Wannier-Mott excitons* instead are mainly observed in semiconductors, where the high dielectric constant contributes to the screening of the e-h interaction. The resulting wavefunction is delocalized over many atoms (Figure 1.2(b)), which allows the excitons to move freely inside the crystal.
- *Charge-transfer excitons* mostly occurs in ionic crystals, where the e^- is transferred from a lattice anion to a nearest neighbour cation.

In all cases, the energy required to ionize the bound e-h pair is referred to as *exciton binding energy* (E_b). While Frenkel excitons are characterized by E_b in the order or 0.1-1 eV, Wannier excitons have E_b of tens of meV, which makes them less stable at room temperature (RT) where $k_B T \sim 25$ meV. For these reasons, the estimation of E_b is critical to determine the nature of the fundamental excitations (free carriers or excitons) in a material at a given temperature. Because Wannier excitons represent the typical fundamental excitations of direct-gap semiconductors, we focus on this type of excitons in the following discussion.

Dispersion relation

A simple and intuitive way to treat the interacting e-h pair is to adopt a modified Bohr model of the hydrogen atom, with two main differences: i) in excitons, the role of the proton is played

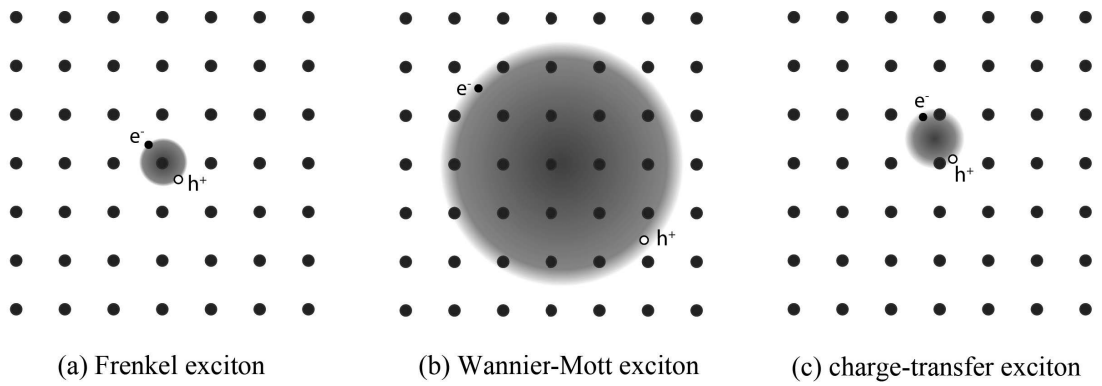

Figure 1.2 – Schematic representation of (a) Frenkel excitons, (b) Wannier-Mott excitons, and (c) charge-transfer excitons.

by the hole; ii) the attractive force between e^- and h^+ in a semiconductor is screened by the dielectric constant ϵ. Therefore, within the effective mass approximation, the e-h Coulomb interaction results in a Coulomb potential term [2]:

$$V_c(\mathbf{r}) = -e^2/\epsilon|\mathbf{r}_e + \mathbf{r}_h| \tag{1.6}$$

and to a series of hydrogen-like discrete states appearing below the gap. By treating separately the relative motion of the e-h and the motion of the center of mass, the dispersion relation of the excitonic quasiparticle can be written as [2]:

$$E_X(n,\mathbf{K}) = E_g - E_X(n) + E_{\text{kin}} = E_g - \frac{Ry^*}{n^2} + \frac{\hbar^2\mathbf{K}^2}{2(m_e + m_h)} \tag{1.7}$$

where $n = 1,2,3,\ldots$ is the principal quantum number; $\mathbf{K} = \mathbf{k}_e + \mathbf{k}_h$ the exciton wavevector (not to be confused with $\mathbf{k}$, which describes the single particle state); Ry^* the exciton Rydberg energy

$$Ry^* = 13.5\text{eV}\frac{\mu}{m_0}\frac{1}{\epsilon^2} \tag{1.8}$$

and μ the exciton reduced mass

$$\frac{1}{\mu} = \frac{1}{m_e^*} + \frac{1}{m_h^*}. \tag{1.9}$$

The exciton Bohr radius a_B is linked to the hydrogen Bohr radius a_H via the relation

$$a_B = a_H\epsilon\frac{m_0}{\mu} \tag{1.10}$$

Figure 1.3 compares the independent e^- and h^+ dispersion (single-particle picture) and the excitonic dispersion (two-particle picture). The presence of excitonic states yields to the

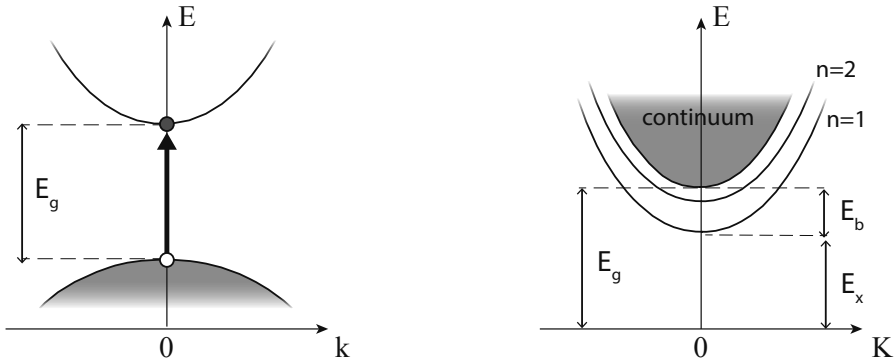

(a) free carrier picture (b) exciton picture

Figure 1.3 – Electron-hole excitation in the case of (a) non-interaction (one-electron approximation) and (b) interacting pairs.

lowering of the onset of the transition by a factor $E_1 - E_g = Ry^*$. This quantity corresponds to the exciton binding energy E_b introduced above. In other words, E_b can be considered as the difference between the *electronic gap*, which is the fundamental energy gap for single-particle excitation, and the *optical gap*, *i. e.* the minimum energy required for a two-particle excitation.

Optical absorption

The presence of excitons has important consequences on the optical spectra of semiconductors. With respect to the free-carrier absorption coefficient of Equation (1.2), the spectrum of Wannier excitons is described by the Elliott formula [3] and has the form:

$$\begin{aligned}\alpha(\omega) &= \alpha_0 \frac{\hbar\omega}{E_b}\left(\alpha_{\text{exc}} + \alpha_{\text{cont}}\right) \\ &= \alpha_0 \frac{\hbar\omega}{E_b}\left[\sum_{n=1}^{\infty} \frac{4\pi}{n^3}\delta\left(\Delta + \frac{1}{n^2}\right) + \Theta(\Delta)\frac{\pi e^{\frac{\pi}{\sqrt{\Delta}}}}{\sinh\left(\frac{\pi}{\sqrt{\Delta}}\right)}\right]\end{aligned} \tag{1.11}$$

In Equation (1.11), α_0 is the joint-DOS prefactor defined in Equation (1.3), E_b is the exciton binding energy, equal to the Rydberg energy already defined in Equation (1.8), and the quantity Δ is defined as

$$\Delta = \frac{\hbar\omega - E_g}{E_b} \tag{1.12}$$

Figure 1.4 shows the absorption spectrum for a 3D semiconductor (GaAs) with inclusion of excitonic effects. With respect to the free-carrier absorption described by Equation (1.2), the absorption spectrum shows a series of discrete lines, whose oscillator strength decreases as $1/n^3$. Because the creation of an exciton lowers the internal energy of the excited e-h pair by a

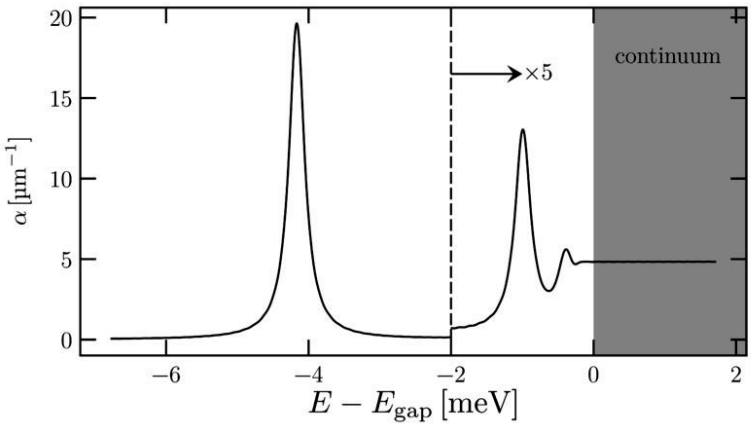

Figure 1.4 – Computed absorption coefficient of bulk GaAs. In presence of linewidth broadening, the higher exciton states merge in the continuum. Reproduced from [4].

quantity E_b with respect to two independent quasiparticles, the first optical excitation of the semiconductor shifts to lower energies with respect to E_g.

Moreover, by comparing Equations (1.2) and (1.11), we notice that the continuum part can be rewritten as

$$\alpha_{\text{cont}} = \alpha_{\text{free}} C(\omega) \tag{1.13}$$

where the tern $C(\omega)$ is referred to as Sommerfeld or Coulomb enhancement factor [1, 5]

$$C(\omega) = \frac{\frac{\pi}{\sqrt{\Delta}} e^{\frac{\pi}{\sqrt{\Delta}}}}{\sinh\left(\frac{\pi}{\sqrt{\Delta}}\right)} \tag{1.14}$$

In contrast to the square-root dependence of the free carrier absorption, at the band edge $\Delta \to 0$ and $C(\omega) \to 2\pi/\sqrt{\Delta}$, so the two dependences cancel each other and the continuum assumes a constant value. In conclusion, the presence of Coulomb correlation has two main consequences on the optical absorption of a semiconductor. First, the appearance of excitonic lines lowers the optical gap of the material; second, the absorption is enhanced not only in correspondence of the resonances, but also in the free-carrier absorption region *via* Coulomb enhancement.

In this thesis, we will recall these concepts and make use of Elliott theory in Chapter 3 to deconvolve the band-edge absorption into exciton and continuum contributions, and estimate the strength of e-h Coulomb interaction.

1.2 High-density effects

When the density of excited e-h pairs becomes significant, the description presented in Section 1.1 no more reflects the behaviour of the material. In fact, Equations (1.2) and (1.11) hold under the assumption of low excitation densities; in this *low-density regime*, the linear optical properties are determined by single e-h pairs (either in the exciton or free-carrier state) whose density is small compared by the total e^- density [6].

With increasing excitation densities, excitons are still good quasiparticles, but their interaction with the photoexcited charges is no more negligible. In this *intermediate-density regime*, exciton-exciton and exciton-carrier scattering processes may lead to linewidth broadening, appearance of new luminescence bands, bleaching/amplification of the absorption, and formation of new quasiparticles as biexcitons (two electrons and two holes) or trions (two electrons and one hole, or viceversa) [6].

By further increasing the density, exchange and correlation potentials as well as band-filling effects renormalize the single-particle energies and cause a sizeable shift of the optical absorption edge. In parallel, as the screening length of free e-h pairs becomes comparable with the exciton Bohr radius, Coulomb screening starts to be at play and modifies the strength of the e-h interaction. In highly-excited semiconductors, these many-body effects contribute simultaneously to the renormalization of the single-particle and two-particle excitation spectra, and give rise to large optical nonlinearities at the absorption edge. Moreover, in ultracold materials, excitonic Bose-Einstein condensation (BEC) is predicted in **k**-space, which occurs when all particles occupy the lowest quantum state.

At even higher excitation densities, we enter the *high-density regime*: here, excitons lose their identity as individual quasiparticles and a new collective phase is formed, which is referred to as *electron-hole plasma* (EHP). In the highly-excited e-h gas, single electrons and holes are not bound to each other as excitons, yet strong correlations can exist between their Fermi sea, which cause strong changes in the optical absorption spectrum of the material [6].

The general scenario for many-body effects in semiconductors is shown schematically in Figure 1.5, which highlights the link between the excitation density and the optical properties of the material. A selection of many-body effects and optical nonlinearities characteristic of the high density regime will be treated in the following.

1.2.1 Bandgap renormalization

Bandgap renormalization (BGR) refers to the energy lowering of the single-particle states as a result of exchange and correlation effects [6]. The former are a direct consequence of Pauli exclusion principle, which forbids two electrons of the same spin to sit in the same unit cell, and causes a redistribution the charges in order to increase their average energy and minimize the repulsive energy. Moreover, correlation effects can further decrease the energy of the e-h

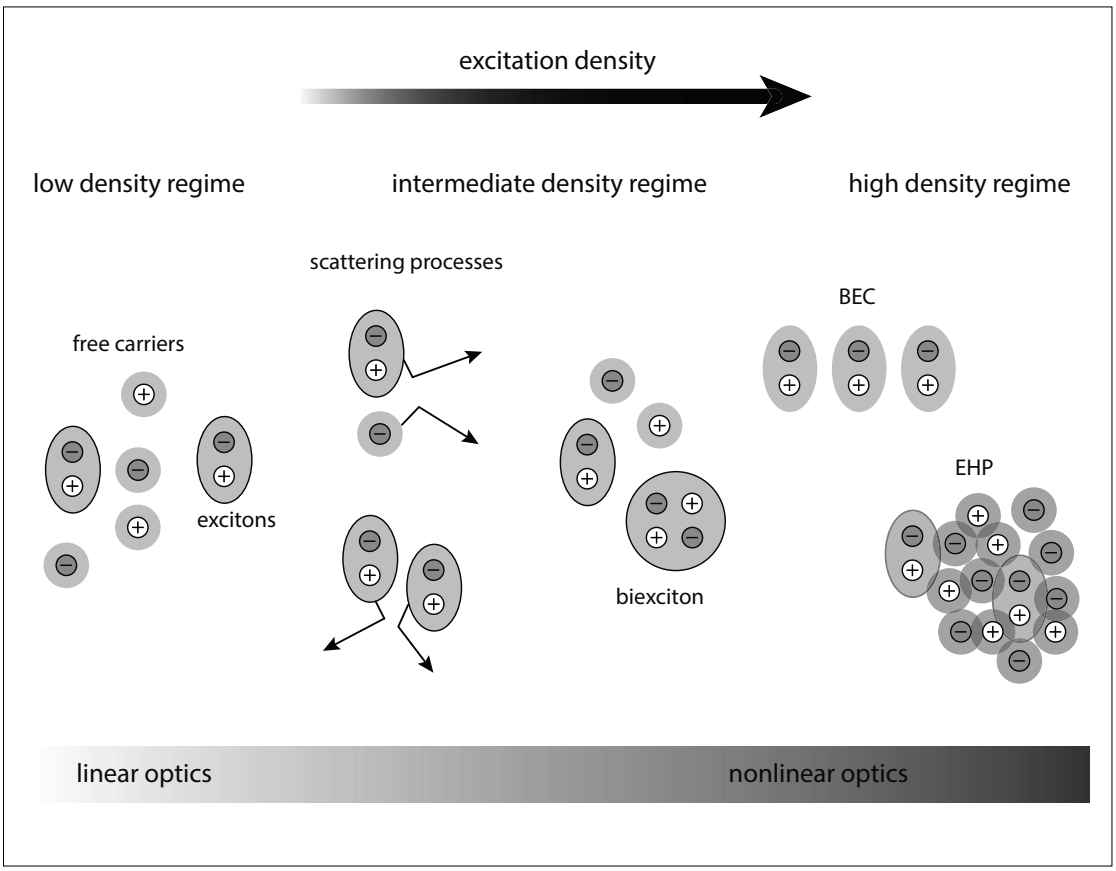

Figure 1.5 – General scenario for many-body effects in semiconductors (BEC = Bose-Einstein condensation, EHP = electron-hole plasma). Inspired by Ref. [6].

system by spatially redistributing the positive and negative charges in the system.

The overall variation in single-particle energy ΔE_{BGR} is then expressed[2] by the sum of the two contributions [7]:

$$\Delta E_{\mathrm{BGR}} = \Delta E_{\mathrm{ee}} + \Delta E_{\mathrm{ei}} \tag{1.15}$$

where ΔE_{ee} can be approximated by

$$\Delta E_{\mathrm{ee}} = -\frac{e^2 k_F}{2\pi^2 \epsilon_0 \epsilon_s} - \frac{e^2 k_{TF}}{8\pi \epsilon_0 \epsilon_s}\left[1 - \frac{4}{\pi}\arctan\left(\frac{k_F}{k_{TF}}\right)\right] \tag{1.16}$$

and ΔE_{ei} by

$$\Delta E_{\mathrm{ei}} = -\frac{e^2 n}{\epsilon_0 \epsilon_s a_B k_{TF}^3} \tag{1.17}$$

[2]The quantities are expressed in SI units.

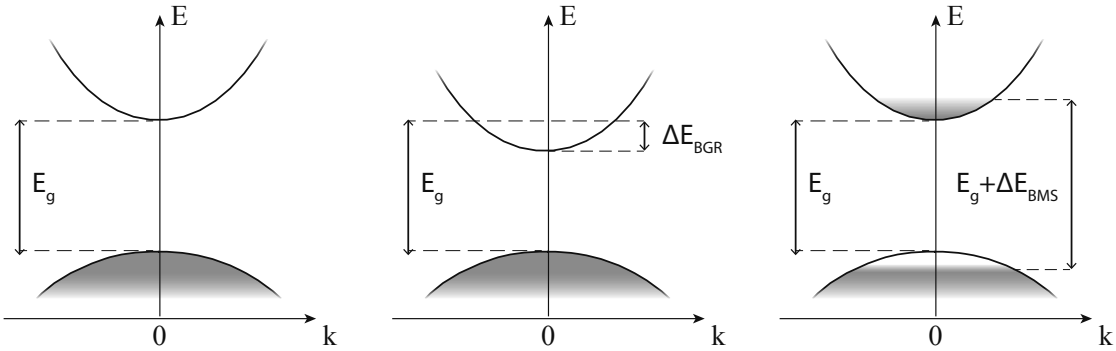

(a) low density regime (b) bandgap renormalization (b) Burstain-Moss shift

Figure 1.6 – Schematic of many-body effects in the single-particle approximation: band dispersion in (a) the low-density regime and in presence of (b) bandgap renormalization and (c) Burstein-Moss effect.

Here, k_F is the Fermi vector:

$$k_F = (3\pi^2 n)^{1/3} \tag{1.18}$$

k_{TF} the Thomas-Fermi screening vector:

$$k_{TF} = 2\sqrt{k_F/(\pi a^*_{B^-})} \tag{1.19}$$

and $a^*_{B^-}$ is the screened Bohr radius of the e$^-$:

$$a^*_{B^-} = \frac{4\pi\epsilon\epsilon_0\hbar^2}{m^*_e e^2} \tag{1.20}$$

In the single-particle picture, BGR results in a shrinkage of the gap with increasing densities, as depicted in Figure 1.6(b). On the optical spectrum, this effects manifests itself as a rigid shift of the absorption edge to lower energies. The same rigid shift occurs in presence of e-h correlations, but no further renormalization of the exciton peak is expected in this case [8].

1.2.2 Phase-space filling and Burstein-Moss shift

Another effect at play at high excitation densities is the so-called Burstein-Moss shift (BMS), which refers to the apparent blueshift of the absorption edge as a result of phase-space filling (PSF). As depicted in Figure 1.6(c), when the bottom (top) of the CB (VB) is occupied by a density of carriers, new degenerate Fermi levels are established. Because the states between quasi-Fermi levels are occupied, these states do not participate to optical transitions due to Pauli blocking. On the optical spectra, band filling results in an apparent shift in absorption

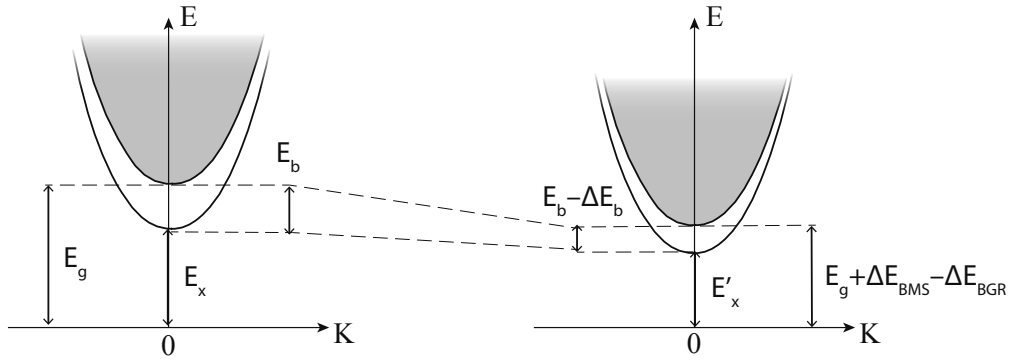

Figure 1.7 – Exciton dispersion in the low density regime and in presence of many-body effects.

onset to higher energies by a quantity [7]:

$$\Delta E_{\mathrm{BMS}} = \frac{\hbar^2 k_F^2}{2m_{eh}} \tag{1.21}$$

where m_{eh} and k_F were defined in Equations (1.4) and (1.18), respectively.

1.2.3 Coulomb screening

In presence of e-h interaction, the exciton energy $E_x = E_g - E_b$ will change following the renormalization of the singe-particle states. In addition to the shift, free charges can screen the e-h Coulomb interaction leading to linewidth broadening and reduction in E_b. The latter quantity can be expressed as [7]:

$$\Delta E_b = \frac{3e^2 k_F}{(4\pi^2)\epsilon_0 \epsilon} \tag{1.22}$$

A scheme of the overall effect of BGR, BMS and CS in the two-particle picture is shown in Figure 1.7. Figure 1.8 shows an example of energy shifts produced in GaN (E_g = 3.38 eV, ϵ_s = 9.38, a_B = 2.76 nm, $a^*_{B^-}$ = 2.15 nm, $m_{eh} = 0.16 m_e$), readapted from the work in Ref. [7]. In general, in the low excitation regime, ΔE_{BMS} and ΔE_{BGR} compensate each other, and no evident shift is detected [9–12]. Conversely, in the high-excitation regime such compensation is no more valid and an overall shift appears, whose sign depends on the dominant effect at the given excitation density. In GaN, at around $9\times10^{18}\mathrm{cm}^{-3}$, the effect of BMS (Equation (1.21), blue curve) overcomes that of BGR (Equation (1.15), red curve), and the sign of their combined contribution (yellow curve) turns from negative (red shift) to positive (blue shift). The green line depicts instead the renormalization of E_b according to Equation (1.22), which combined with the single-particle renormalization effects results in an overall exciton energy E_x (violet curve).

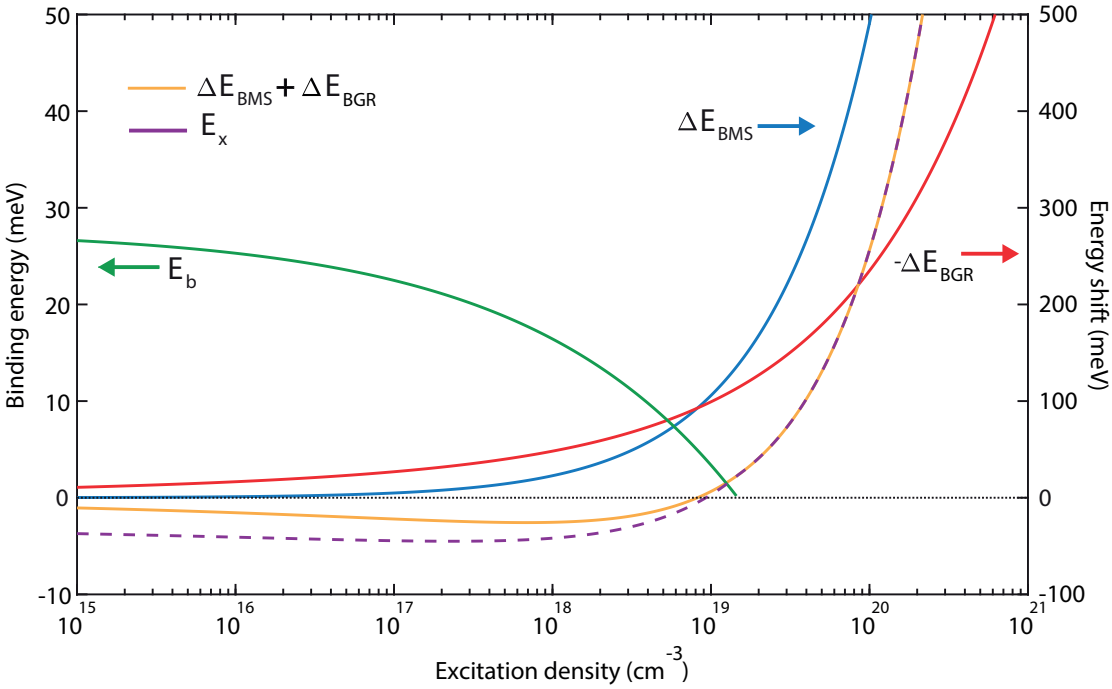

Figure 1.8 – Contributions of Burstain-Moss shift (BMS, blue curve), bandgap renormalization (BGR, red curve) and Coulomb-screening (CS) of E_b (green curve), to the exciton transition energy E_x as results from Equations (1.15), (1.21) and (1.22) evaluated for GaN. The calculations are reproduced following Ref. [7].

1.2.4 Excitonic Mott transition

One of the most important effects that characterizes the high-density regime is the transition from an insulating exciton gas at low densities into a fully ionized EHP, which is typically referred to as the Mott transition [13]. In fact, in presence of increasing high carrier densities, E_b is expected to be reduced by Coulomb screening until the vanishing of the e-h interaction. This causes the gradual broadening and eventually the suppression of the excitonic peak, and is accompanied by a strong modification of the optical spectrum at the absorption onset.

In the literature, there exist several criteria to estimate the critical density at which the insulator-to-metal transition occurs. A first simple estimate can be obtained by considering the e-h density in the excitation volume for which the average carrier distance is comparable with the exciton Bohr radius:

$$n_M a_b^3 \approx 1 \tag{1.23}$$

However, a more precise estimate of n_M would require the inclusion of the screening length of the free-carriers. To start, we consider an exciton in a sea of free electrons and holes of density n_p. In presence of free carrier screening, the exciton Coulomb potential term of Equation (1.6)

transforms in a Yukawa-type potential [6, 14]:

$$V_Y(\mathbf{r}) = \frac{1}{4\pi\epsilon_0\epsilon(\omega, n_p)} \exp\left(-\frac{|\mathbf{r}_e + \mathbf{r}_h|}{l}\right) \frac{e^2}{|\mathbf{r}_e + \mathbf{r}_h|} \tag{1.24}$$

where now ϵ is energy- and density dependent, and accounts for the exciton dynamical screening. The quantity l appearing in Equation (1.24) is the screening length of the free carriers. Differently from the Coulomb potential, the Yukawa potential has only a finite number of bound states; in particular, the spectrum becomes a continuum if l falls below a certain limit l_c, which is linked to a_B *via* the relation:

$$a_B = 1.19 l_c \tag{1.25}$$

Depending on the conditions, the screening length of a EHP of density n_p can be calculated in different ways. If the e-h gas is described by Boltzmann statistics, one can consider the Debye-Hückel length l_{DH}:

$$l_{DH} = \left(\frac{\epsilon_0\epsilon k_B T}{8\pi e^2 n_p}\right)^{1/2} \tag{1.26}$$

By using this expression, the density at which excitons cease to exist is:

$$n_M = 1.19^2 \frac{\epsilon_0\epsilon k_B T}{e^2 a_B^2} = 1.19^2 \frac{k_B T}{2 a_B^3 E_b} \tag{1.27}$$

It is clear that the assumptions of Boltzmann statistics are valid at high temperature, yet they cannot be applied for low temperatures, where the carrier gas is degenerate. In this case, a more appropriate choice for the screening length is the Thomas-Fermi one, l_{TF}:

$$l_{TF} = \left[\frac{\epsilon_0\epsilon\hbar^2}{3e^2} \frac{1}{m_e + m_h} \left(3\pi^2\right)^{2/3} n_p^{-1/3}\right]^{1/2} \tag{1.28}$$

which results in a critical density equal to

$$n_M = \left(\frac{1.19}{a_B}\right)^6 \left(\frac{\epsilon_0\epsilon\hbar^2}{3e^2} \frac{1}{m_e + m_h}\right)^3 \left(3\pi^2\right)^2 = a_B^{-3} \frac{\pi 1.19^6}{4^3 \cdot 3} \left(\frac{m_e m_h}{(m_e + m_h)^2}\right)^3 \tag{1.29}$$

A number of other methods exist to the estimation of the critical density (see for instance Chapter 21 in Ref. [6]). However, all these criteria are based on different model assumptions, which usually yield to over- or underestimation of n_M by one or two orders of magnitude [6]; therefore, the exact criterion for the calculation of n_M remains a matter of discussion. In general, this problem can be overcame by using more sophisticated many-body theories to describe the interaction between a dense e-h plasma and the excitonic states [6]. We will address this issue in Chapter 3, in the frame of the study of the Mott transition in hybrid

organic-inorganic perovskites.

1.3 Dynamics of photoexcited carriers

In classical semiconductors at thermodynamic equilibrium, the absorption of photons of above-gap energy $h\nu > E_g$ results in the creation of nonequilibrium e-h populations with a certain excess energy and elevated temperatures, which directly affects the optical properties of the material. We consider here the case of excitation by an ultrashort laser pulse, whose duration is much shorter than the carrier scattering time; in this case, we can treat the excitation to be instantaneous [5]. In a second stage, the photoexcited system relaxes to thermodynamic equilibrium *via* different stages, which are temporally overlapping but characterized by different timescales [5, 15]. These processes are depicted schematically in Figure 1.9 and are discussed in detail in the following.

1.3.1 Early-time relaxation

- *Coherent regime (<200 fs).* Upon illumination by an ultrashort laser pulse, the excitations in the material will retain some phase relationship with the coherent radiation and among themselves. The coherence is subsequently destroyed through scattering processes in hundreds of fs.

- *Non-thermal regime (≤2 ps).* Immediately following the excitation (Figure 1.9(a)), the distributions of electrons and holes are *non-thermal. i. e.* they cannot be described by a single temperature. The redistribution of energy and the evolution to thermal distributions occurs on the sub-ps timescales *via* various scattering processes, with carrier-carrier interaction being the most efficient. This process of energy exchange among charge carriers is called *thermalization.* The thermalized population can be described by Fermi-Dirac functions characterized by equilibrium temperatures T_e and T_h (Figure 1.9(b)). Eventually, e-h will thermalize among themselves to reach a common temperature T_C.

- *Hot carrier regime (1-100 ps).* After thermalization, the carrier temperature T_C is still much larger than the lattice temperature T_L, and the system is in the *hot carrier regime.* In hundreds of ps, interaction with phonon modes brings all the populations (free carriers, excitons, phonons) in thermal equilibrium with the lattice (Figure 1.9c). In typical semiconductors, electrons and holes lose their excess energy and cool to the edge of their respective bands *via* the emission of optical phonons. This scattering is typically mediated by the Fröhlich interaction of charge carriers with longitudinal optical (LO) phonons with energy $\hbar\omega_{LO}$.

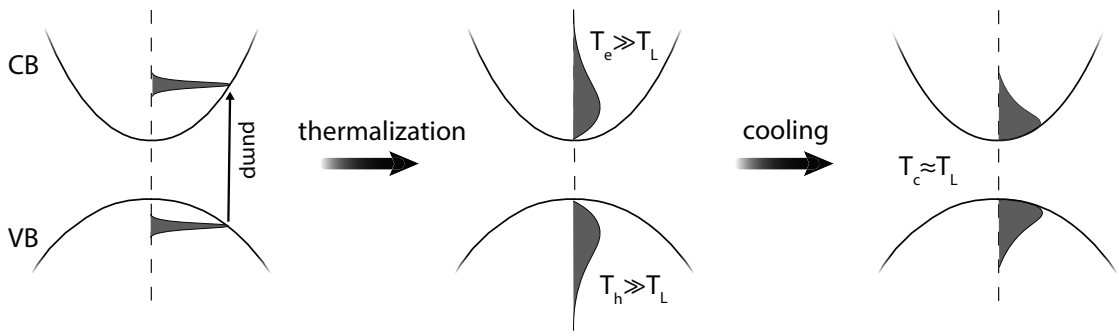

(a) non-thermal population (b) hot population (c) cold population

Figure 1.9 – Schematic illustration of carrier relaxation processes. (a) Initially, the ultrashort pulse creates a non-thermal carrier energy distribution. (b) Then, a thermalized distribution with $T_e, T_h \gg T_L$ is reached *via* carrier-carrier scattering. (c) Finally, though carrier-phonon scattering, the carriers cool down until the equilibrium with the lattice temperature is reached. Inspired by [16].

1.3.2 Recombination

Once the carriers have reached the band edge and are in equilibrium with each other, the relaxed e-h pairs will start recombining to reach the initial thermodynamic equilibrium. The recombination occurs *via* one-, two-, and three body processes expressed through the rate equation [17]:

$$\frac{dn}{dt} = -k_3 n^3 - k_2 n^2 - k_1 n \tag{1.30}$$

In Equation (1.30), n is the charge carrier density; k_1 is the rate associated with monomolecular trap-assisted recombination, which involves a single particle (e^- or h^+); k_2 is associated to two-body processes, thus describes intrinsic e-h recombination, which is accompanied by emission of a photon; finally, k_3 reflects Auger recombination processes involving three particles, where the energy resulting from e-h recombination is transferred to a third particle. In the ideal case of absence of defects or impurities ($k_1 \approx 0$), the dominant processes are the two-body radiative and the three-body non-radiative band-to-band recombination. Equation (1.30) also indicates that trap-assisted recombination dominates at low excitation densities, and that Auger processes only occur at high enough densities. In this regard, mapping the evolution of the decay times as a function of n is a powerful approach to unravel the recombination dynamics of the material and reveal the relative contribution of traps, excitons and free carriers, which is crucial to the optimal performance in semiconductor-based light-emitting devices.

1.3.3 Studying carrier dynamics *via* ultrafast spectroscopy

To access the relaxation dynamics of a system upon photoexcitation, an ideal tool is represented by ultrafast spectroscopy. This term comprises a wide range of techniques, specifically

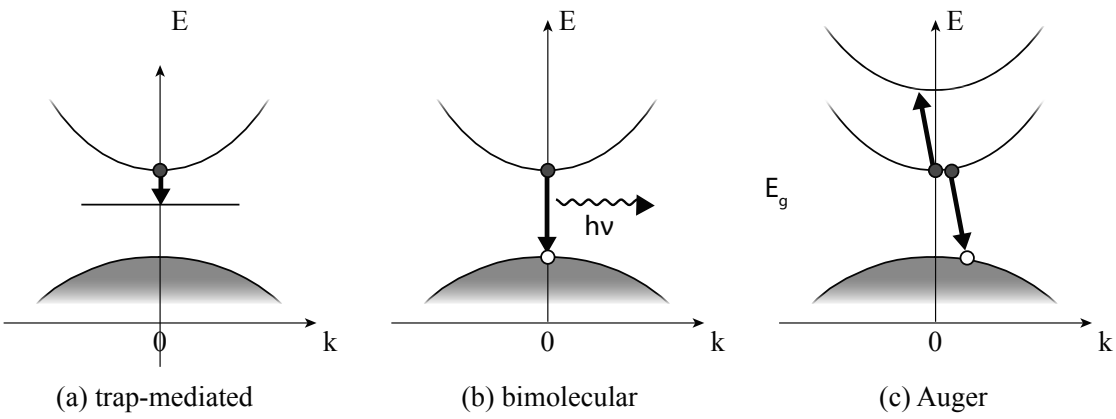

(a) trap-mediated (b) bimolecular (c) Auger

Figure 1.10 – Typical recombination mechanisms in semiconductors: (a) monomolecular (trap-assisted) recombination, (b) bimolecular (radiative) recombination, (c) Auger (non-radiative) recombination. Readapted from Ref. [17].

designed to access different observables related to the properties of materials. Such time-resolved (TR) techniques are based on the use of two synchronized pulses, the pump and the probe. Typically, the pump is an ultrashort laser pulse, which photoexcites instantaneously the material and creates an nonequilibrium distribution of excitations. These transient states are then monitored at different time delays with the probe pulse, whose nature determines the type of information that can be accessed. Examples of physical quantities that can be detected in the nonequilibrium regime are: the single-particle excitation spectrum (TR-angle resolved photoemission); the two-particle excitation spectrum (transient absorption/reflectance, THz, second harmonic generation, TR-photoluminescence); the X-ray spectrum (TR-X-ray absorption); structural changes (X-ray diffraction, electron diffraction); inelastic scattering (TR-Raman, TR- Inelastic X-ray scattering, electron energy-loss); real-space imaging (scanning tunnelling and transmission electron microscopy). In this thesis, we focus on ultrafast optical spectroscopy in the visible and ultraviolet (UV) spectral region, which correspond to the bandgap energies of hybrid perovskites and titanium dioxide, respectively.

The simplest form of ultrafast spectroscopy is the so-called *degenerate pump-probe*, where a single pulse is divided into two so that the probe and excitation pulses present the same spectral and temporal characteristics. When ultrafast spectroscopy is performed in a *broadband* fashion (*i. e.* the probe covers a wide spectral region), a rich body of information can be accessed simultaneously in the time- and energy domain. In several systems, the possibility of combining broadband detection with a tunable pump energy is intriguing. In semiconductors, the choice of the pump photon energies $h\nu \geq E_g$ determines the k-point in the Brillouin zone where the e-h density is created: resonant excitation with $h\nu = E_g$ will excite a dense e-h or exciton population at the edge of the bands; non-resonant excitation, *i. e.* for $h\nu > E_g$, mainly excites free e-h pairs that might eventually decay in excitons.

The photoexcitation of free or bound e-h transiently modifies the electronic properties of the system, which reflects in a change of its optical properties. Because such changes are on

the order of few percents with respect to the equilibrium quantity, one usually monitors the *differential* spectrum, which is given by the difference between the equilibrium and perturbed spectra. The main effect of photoexcited e-h densities is to induce a transparency in the material at specific energies, which in a transient absorption spectrum (ΔA) results in a negative signal (bleach). The intensity of the bleach is proportional to the density of carriers at one specific time delay, and its dynamics can be related to the relaxation dynamics of the carriers at the band edge (see Section 1.5.2 or Ref. [18] for a detailed discussion).

An ultrashort laser pulses can generate very high excitation densities in the material. The photoexcited system then represents the ideal playground to investigate many-body effect and the photoinduced optical nonlinearities. In the case of excitonic materials, the ultrafast exciton renormalization (that is, a change in peak energy, linewidth, or oscillator strength) is readily reflected in the transient spectrum and can be extracted using *ad hoc* lineshape analysis. These concepts will be applied in Chapters 3 and 4, in which we address the study of ultrafast exciton dynamics by using ultrafast spectroscopy techniques.

1.4 Organometal halide perovskites

Organo-lead halide perovskites (HOPs) semiconductors have revolutionized the recent research activity on new-generation photovoltaics (PV), holding huge promise to harness solar energy at low cost. The combined efforts towards the optimization of processing methods, chemical compositions and cell architecture, has led to an unprecedented growth in photoconversion efficiency from 3.8% to more than 23% in less than 10 years of research [19, 20]. In parallel, the remarkable properties of HOPs have opened the door to a variety of optoelectronic applications beyond photovoltaics [21]. In this Section, we review the main applications and physical properties of metal-halide perovskites; a particular focus is put on the nature of optical excitations in these materials, which is one of the cornerstones on which this thesis work is based.

1.4.1 The emergence of hybrid perovskites

In their first appearance in the solar cells community, methylammonium lead triiodide ($CH_3NH_3PbI_3$) perovskites were introduced as light harvesters in the dye-sensitized solar cells (DSSC) configuration [19], depicted schematically in Figure 1.11(a). In this configuration, the perovskite acts as absorbing layer, in which e-h are generated upon photon absorption and transferred respectively to the electron-transporting material (ETM, usually mesoporous TiO_2) and to the hole-transporting material (HTM).

Despite the low efficiency and poor stability of the early devices, the excellent e-h mobilities of HOPs [22–24] yielded to a rapid evolution from a *sensitized* cell, where the perovskite functions mainly as a light harvester and charge transport occurs in other materials, to a new concept of *thin film* perovskite solar cell (Figure 1.11(b)), where most charge transport occurs in the bulk

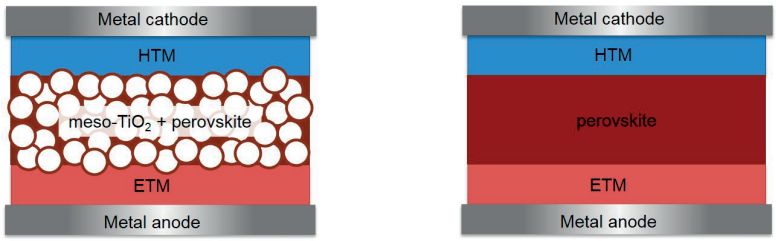

(a) DSSC (b) Planar etherojunction

Figure 1.11 – Schematic of a perovskite solar cell in the (a) DSSC configuration, where charge generation and extraction occur at the perovskite/EHT interface, and (b) planar heterojunction, where charge generation, migration and extraction occur in the perovskite layer.

of the perovskite itself [25, 26]. Nowadays, perovskite solar cells approach the performances of silicon-based technologies and promise to challenge the PV market thanks to the scaling up of the fabrication methods of these solution-processed semiconductors.

On the other hand, according to the Schockley-Quieisser formulation, an efficient solar material should also be a good light emitter, *i. e.* the only recombination channel should ultimately be the radiative one [21, 27]. This suggests that, beyond their use in PV devices, HOPs are ideal candidates for high-performance, light-emitting applications such as light-emitting diodes (LEDs). In fact, in 2014 the first LEDs incorporating the 3D mixed anions perovskites have been demonstrated [28], initiating another strand of research on the use of HOPs in optoelectronics. Another interesting example of the use of HOPs is lasing, reported at RT in the 3D material thanks to a stable and color-tunable amplified spontaneous emission [29, 30]. The evolution of HOP-based PV and optoelectronic devices has been the subject of many excellent reviews [31–34]. In the following, we focus on the fundamental photophysical properties of HOP.

1.4.2 Crystal structure

The word “perovskite” originally refers to the material $CaTiO_3$, named after the Russian mineralogist Perovski. Generally, with “perovskite” we refer to the class of materials with crystal structure ABX_3, where X is an anion and A and B are two cations of different sizes, A being larger than B. The 3D structure, shown in Figure 1.12, is based on corner-sharing BX_6 octahedra, the B cation sitting in the center and the X atoms at the corners. The A cations are located at the interstices, surrounded by eight octahedra [32].

In HOPs, whose first report dates back to 1958, the larger cation is an organic molecule, the smaller cation is usually Pb, and the anion is a halogen (I, Br or Cl). Among the several combinations of organic and inorganic components, the relevant compounds for energy conversion are the methylammonium (CH_3NH_3, MA) lead triiodide $MAPbI_3$. Variations from the most common MA cation include formamidinium ($NH_2CH{=}NH_2^+$, FA) and mixed MA-FA

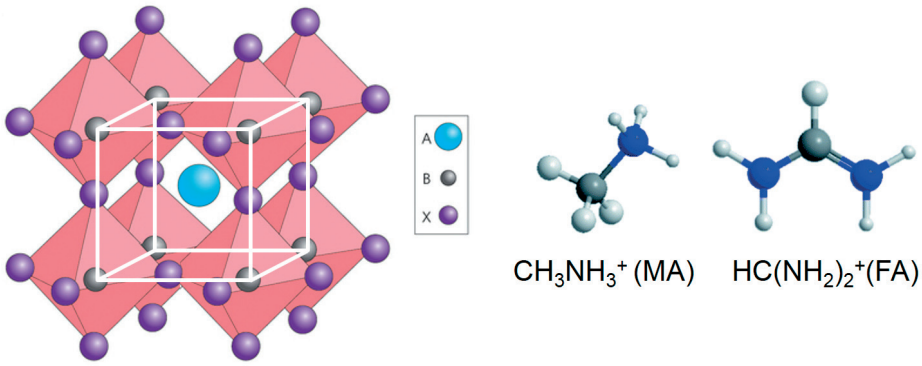

Figure 1.12 – Cubic perovskite crystal structure. For perovskites relevant to PV, the large cation A is usually methylammonium ($CH_3NH_3^+$, MA) or formamidinium ($NH_2CH{=}NH_2^+$, FA) the small cation B is Pb and the anion X is a halogen ion (I, Cl or Br). Readapted from Ref. [32].

species [32], which are emerging with excellent performances. For the B cation, Pb-based perovskites are so far the best performing materials [31]. The resulting $MAPbX_3$ crystals are direct-gap semiconductors, with E_g equal to 1.6 eV (X=I), 2.4 eV (X=Br) and 3.1 eV (X=Cl) [19, 35, 36], which be easily tuned by modifying the relative content of each halide [23, 37]. The bandgap energy of $MAPbI_3$, the prototypical HOP on which most of the studies have focused, corresponds to an absorption onset of 800 nm, making this material a good light absorber over the whole visible solar emission spectrum [31].

Perovskite-like crystals exhibits structural phase transitions upon temperature variations [38, 39]. For instance, $MAPbI_3$ can be found in three different structures: a high-temperature cubic phase above 327 K, a tetragonal phase between 327 K and 162 K, and a low-temperature orthorhombic phase below 162 K [40, 41]. Phase transition temperatures of the Br compound are found to be 151 K, 156.5 K and 236.3 K. Thus, at RT $MAPbI_3$ and $MAPbBr_3$ show tetragonal and cubic structures respectively [42].

1.4.3 Band structure and optical spectra

To clarify the electronic properties of HOPs, several groups reported band structure calculations mainly using density-functional theory (DFT) [43–48]. To describe the real electronic structure of band insulators, quasiparticle corrections at the GW level are needed [49–51]. The presence of heavy ions like Pb in the hybrid perovskites also requires spin-orbit-coupling (SOC) corrections to be taken into account, which lead to the splitting of the lowest CB of these materials. Figure 1.13(a) schematically represents the band structure of $MAPbI_3$ at RT. The direct gap is found at the R point of the Brillouin zone; the lowest CB is dominated by $6p$ orbitals of Pb, while the highest VB is made of contributions of Pb $6p$- and I $5p$ hybridized orbitals [43, 44, 52]. The organic cations instead provide weak dispersionless contributions deep in the VB and high in the CB [53]; nevertheless, this molecule is a dipole nearly free to

move, and can indirectly change the optoelectronic properties by influencing the Pb-X lattice, as well as by introducing orientational disorder and lattice polarizability [48]. In Figure 1.13(a), the arrows represent allowed interband transitions, which translate the absorption spectrum of Figure 1.13(b) (reported for $MAPbI_3$, E_g=1.6 eV).

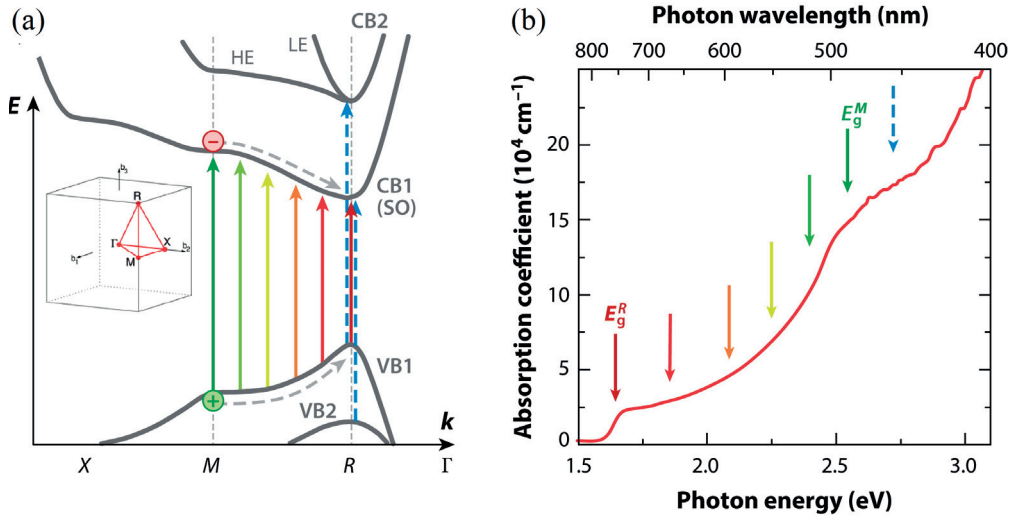

Figure 1.13 – (a) Schematic electronic band structure of $MAPbX_3$, where the arrows represent allowed interband transitions and the dashed arrows the partly-allowed transitions at the R point (HE = heavy electrons, LE = light electrons, SO = split-off). The inset shows the 3D Brillouin zone for a cubic crystal structure. (b) Typical absorption spectrum of $MAPbI_3$ at RT. Readapted from Ref. [17].

1.4.4 Controversial nature of photoexcited species

An interesting aspect of HOP research is the gap between the fast advance in technology and the slower progress in understanding their fundamental physical properties. The knowledge of the microscopic processes that enhance or limit the performances is critical to the design of efficient devices, and can offer at the same time the opportunity to explore novel physical properties of these hybrid materials. In this regard, the mixed organic-inorganic nature makes one wonder whether the behaviour of these materials is more akin to organic or inorganic semiconductors, which in turn reflects to the question whether the fundamental excitations are best represented as excitons or free carriers.

In excitonic solar cells, where the active layer is an organic material, a donor/acceptor heterojunction interface with a large energy offset is required to provide the internal electrochemical driving force for the dissociation of Frenkel excitons; conversely, in inorganic solar cells the thermal energy at RT is sufficiently large to promote spontaneous dissociation of the bulk excitation into free carriers with minimal energy loss [54]. On the other hand, large E_b might be desirable in perovskite-based light-emitting devices, as a higher E_b results in larger e-h capture rates for radiative recombination [28, 55]. Moreover, excitons also play a central role

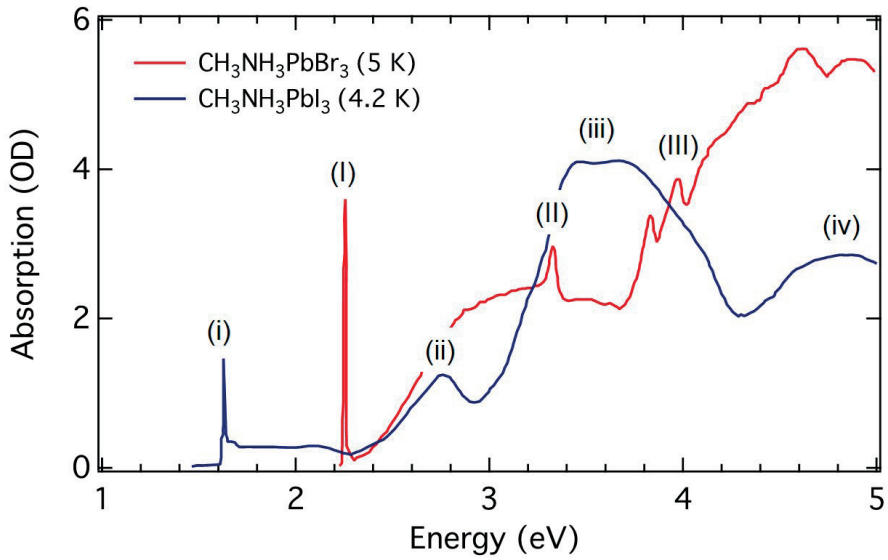

Figure 1.14 – Optical absorption spectra of $MAPbX_3$ (X=I, Br) single-crystals calculated from the reflectivity spectra using Kramers-Kronig relations. Readapted from Refs. [43, 69].

in spintronic devices, as the manipulation of the spin degrees of freedom of the bound species in Rashba-split semiconductors is key to the development of spin-polarized circuits [56–58].

Given the relevance of the subject, a plethora of studies have focused on understanding the extent to which the exciton scenario describes the physics of these systems [54, 59–68]. Although they moved in the spotlight only in the 2000s, a large part of our solid-state physics understanding of HOPs dates back to the 1990s, thanks to the pioneering works on Pb-based perovskite crystals [59, 69, 70]. In Figure 1.14 we report the absorption spectra of $MAPbI_3$ and $MAPbBr_3$ single crystals at 4.2 K and 5 K, respectively. The absorption is calculated from the reflectivity spectra using Kramers-Kronig relations [35, 43, 69]. In the Br compound, sharp excitonic lines appear at 2.26 eV (I), 3.33 eV (II), and 3.9 eV (III). The low-temperature spectrum of $MAPbI_3$ shows similar structures, where the bands at 1.63 eV (i), 2.8 eV (ii), and 3.6 eV (iii) have also been assigned to excitonic transition with lower oscillator strength. From these spectra, E_b of 50 meV and 75 meV for the I and Br compound were estimated for the first excitonic line. Such E_b is sufficiently low to describe the excitons within the Wannier-Mott model [71, 72], providing a first clue on the behaviour of these materials: HOPs are more akin to typical inorganic semiconductors rather than to organic molecular solids.

With binding energies in the order of $k_B T$, the role of excitons in the RT operating device is one of the hot topics in the HOPs community. The major obstacle regards the estimation of E_b at RT, which might differ from the low-temperature value because of the phase transitions [17]. More recent studies reported a much smaller E_b of few meV, in accordance with the high low-frequency dielectric constant, calculated to be ~70 by combining spectroscopic ellipsometry and low-frequency impedance measurements [54, 62]. Thanks to time-resolved

spectroscopies, which have been extensively used to clarify the nature of charge carriers, a general consensus has been reached for the $MAPbI_3$ material, suggesting the predominance of free-carriers as photoexcited species in the operating device [17, 47, 60, 62, 66, 73, 74].

Nevertheless, the emerging free carrier picture in $MAPbI_3$ should not be generalized for all the compounds. In fact, well-resolved excitonic resonances dominate the RT electrodynamics of bulk $MAPbBr_3$ ($E_b = 60 - 70$ meV) and $MAPbCl_3$ ($E_b = 41$ meV) because of the reduced dielectric constant [43, 64, 75–78]. An exciton binding energy of several hundreds of meV also characterizes the response of perovskites in the quasi-two-dimensional limit due to the decreased dimensionality and quantum confinement [79–81]. In the latter cases, bound states still persist as robust entities at RT, since the thermal energy alone is not sufficient to dissociate the bound e-h pair.

While free carriers are beneficial for PV applications, the presence of RT excitons in HOPs opens to the use of these materials in many other optoelectronic device, whose operation is based on bound e-h pairs. However, a fundamental difference exists between the photoexcitation regimes of the active material in these devices: while photogenerated carrier densities in a PV cell are of the order of 10^{14}-10^{15}cm^{-3}, injected or photogenerated charge densities in optoelectronic devices can reach densities as high as 10^{18}-10^{20}cm^{-3} [17]. In these regime, excitons might cease to be good quasiparticles, and the high-density phenomena discussed in Section 1.2 start to be at play. The behaviour of hybrid perovskites in the high-excitation regime is the focus of our study in Chapter 3.

1.5 Anatase TiO_2

Transition metal oxides (TMOs) are a superior class of materials for converting light into other forms of energies. Among these, anatase titanium dioxide (TiO_2) stands out as a cheap, non-toxic, stable, and highly reactive material, and attracts huge interest for a variety of applications.

In solar energy conversion (Figure 1.15(a)), TiO_2 has been routinely used as transparent conductive material in DSSC [82], and more recently in HOP-based solar cells [83]. On the one hand, mesoporous TiO_2 serves as a scaffold and provides high surface area for the interaction with the dye; on the other hand, the electronic levels of TiO_2 are optimally aligned for electron injection from most of commercial dyes, and offer high mobility for photogenerated charge collection. Anatase TiO_2 is also known as an excellent photocatalyst [84, 85]. In these applications, absorption of UV light creates free charges, which participate to the chemical reaction at the surface by transferring the charge to the absorbed species (Figure 1.15(b)). In TiO_2, the photogenerated holes tend to migrate on the surface of materials, enhancing the collection of free electrons from the external compounds [86].

At the heart of these technologies are the processes of charge generation, thermalization, localization, and transport. In the last decade first significant steps have been made toward the

understanding of the photophysics of this material, mainly by the application of time-resolved spectroscopies (Section 1.5.2). However, it was only recently that our group demonstrated the existence of strongly bound excitons in anatase TiO_2 [87]; these quasiparticles represent a novel spectroscopic observable, which encodes the details of several electronic process. The study of excitons in wide-gap semiconductors is possible thanks to time-resolved techniques using a broadband UV probe, which has the potential of accessing the nonequilibrium dynamics of the material in the region where spectral weight is removed upon above-gap photoexcitation. In this way, the investigation of the photophysics of TiO_2 directly at the band edge has the potential to refine the ultrafast spectroscopy picture that has been established in the last decades.

In the following, we review the fundamental electronic and optical properties of TiO_2, with a highlight on the physics of the recently-discovered strongly bound excitons. Then, we provide a brief overview on the outcome of ultrafast optical studies of this material, with a focus on our ultrafast UV spectroscopy investigation of anatase TiO_2 nanoparticles (NPs), which are discussed extensively elsewhere ([18, 88, 89], can be found at the end of the thesis) and which put the basis for the work presented in Chapters 4 and 5.

1.5.1 Band structure and optical spectra

Anatase TiO_2 crystallizes in a tetragonal unit cell based on corner- or edge-sharing TiO_6 octahedra (Figure 1.16(a)). Because of the pronounced difference between the lattice constants (a = 3.78 Å and c = 9.51 Å), TiO_2 is characterized by strong anisotropy in its optical and electronic properties. This is reflected by an almost flat dispersion along the Γ–Z direction in the Brillouin zone (Figure 1.16(b)), as well as by very different RT dielectric functions for orthogonal incident electric fields, $\mathbf{E} \perp c$ and $\mathbf{E} \parallel c$ (Figure 1.17).

The ϵ_2 spectrum (blue curves in Figure 1.17) is characterized by three sharp resonances. Peak (I), found at around 3.82 eV, is assigned to a strongly bound exciton with a high E_b =180 meV at low temperature. The corresponding states arise along the Γ–Z direction, where the

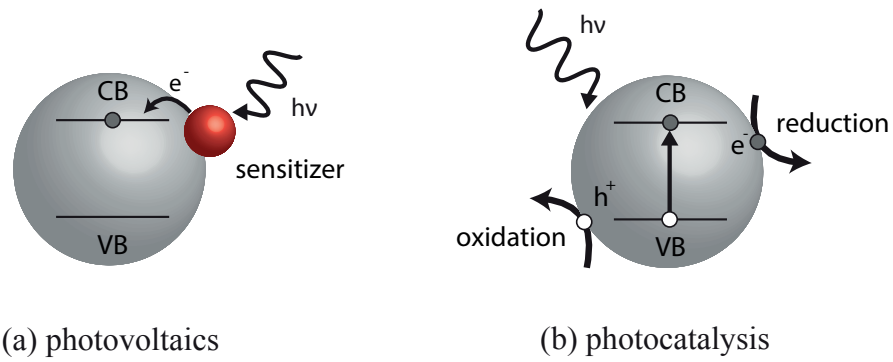

Figure 1.15 – Schematic of the charge carrier pathways upon light absorption in TiO_2-based (a) photovoltaic and (b) photocatalysis applications.

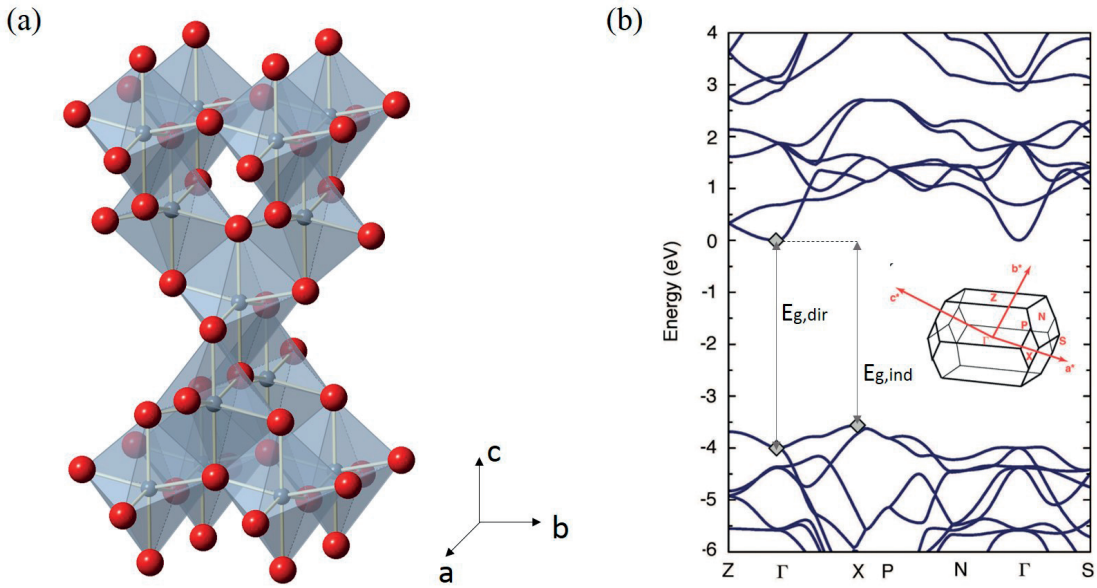

Figure 1.16 – (a) Crystal structure of anatase TiO_2 with highlighted TiO_6 octahedra, where blue atoms represent titanium and red atoms represent oxygen. (b) *Ab initio* calculation of the electronic structure of anatase TiO_2; the inset in displays the 3D Brillouin zone. Readapted from Ref. [87].

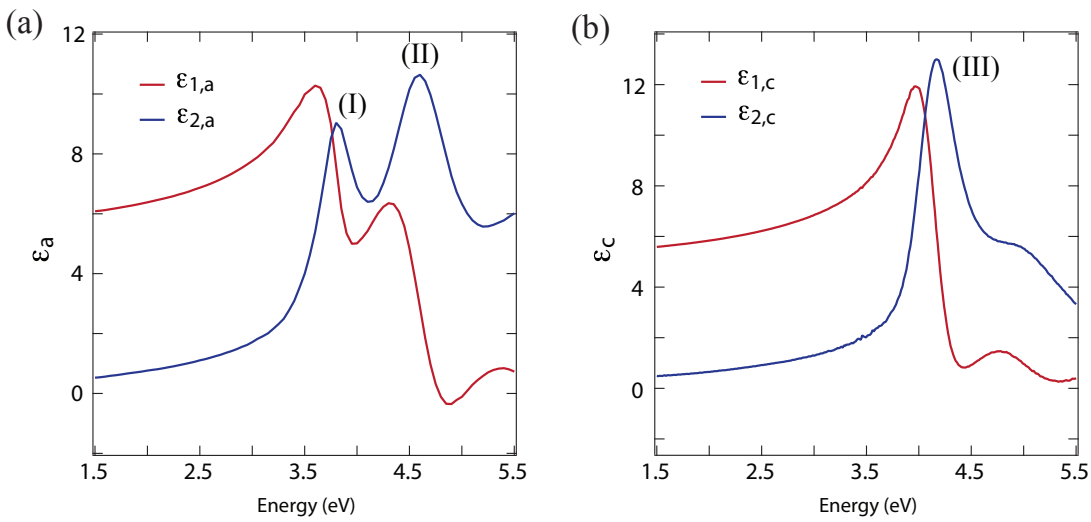

Figure 1.17 – Complex dielectric function of the (010)-oriented TiO_2 single crystal at RT for (a) $\mathbf{E} \perp c$ and (b) $\mathbf{E} \parallel c$. The real part $\epsilon_1(\omega)$ and the imaginary part $\epsilon_2(\omega)$ are plotted in red and blue respectively. Peak (I) and (III) correspond to the 2D exciton (a-exciton) and a localized exciton (c-exciton) respectively, while peak (II) is assigned to a resonant excitation not contributing to the bound state. Readapted from Ref. [87].

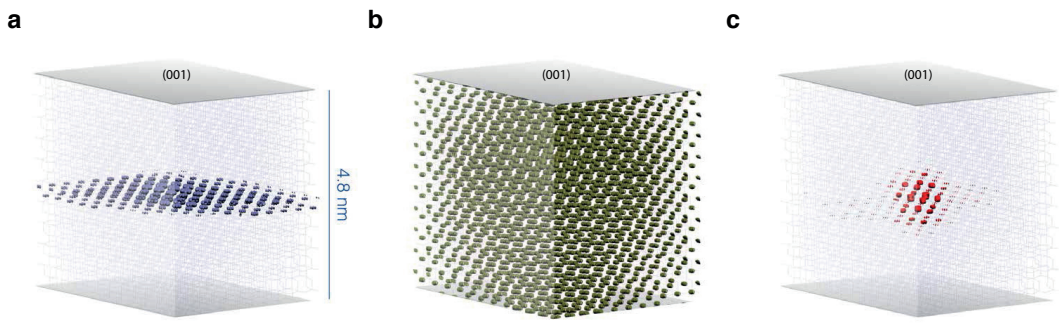

Figure 1.18 – Wavefunctions of the fundamental charge excitations in anatase TiO_2; the coloured region represents the excitonic squared modulus wavefunction. (a) Bound exciton (I) (a-exciton) at 3.76 eV. (b) Resonance (II) at 4.37 eV. (c) Bound exciton (III) (c-exciton) at 4.28 eV. Reproduced from Ref. [87].

bands are almost parallel (Figure 1.16(a)), and the transition is dipole allowed when the light polarization lies along the (001) crystallographic plane. Because of the strong anisotropy, the exciton wavefunction is confined in a single (001) atomic plane (Figure 1.18(a)), and represents one of the first examples of 2D excitons in a 3D crystal lattice [87]. The feature at 4.57 eV (peak (II)) is assigned to a resonant excitation not forming a bound state (Figure 1.18(b)), while the prominent feature in $\epsilon_{2,c}$ (peak (III)) represents a localized exciton with a spherical wavefunction (Figure 1.18(c)); the low-temperature E_b is 150 meV, and the transition is allowed for light polarized perpendicular to the (001) plane. As they are formed by holes in oxygen $2p$ states and electrons in titanium $3d$ states, these quasiparticles are classified as charge-transfer excitons [87].

Remarkably, the bound states in TiO_2 are very robust against sample quality and temperature, and are also observed in defect-rich NPs and films used in RT applications [87]. Conventional TiO_2 NPs are expected to show a bulk-like behaviour, as their size (≥5 nm) is larger than the exciton Bohr radius (3.2 nm), thus excluding confinements effects. Remarkably, despite their featureless absorption spectrum, the non-equilibrium optical spectra of TiO_2 NPs shows clear spectral fingerprint of both (I) and (III) excitons (in the following referred to as *a-exciton* and *c-exciton* respectively). Because of the random orientation of the crystallographic axis, both excitons appear simultaneously in a colloidal NP solution [87].

1.5.2 Ultrafast dynamics

Because of its central role in photocatalysis and photovoltaics, in the last decades the charge carrier dynamics in TiO_2 has intensely been studied. Ultrafast broadband optical spectroscopies from the THz to the visible has been used to reveal the details of e-h recombination pathways and clarify the role played by defects. In fact, the reduced form of TiO_2 is intrinsically characterized by oxygen vacancies, which are the most common types of defects in this

material. These impurities play a fundamental role as trapping centers for the free charges. This is particularly relevant when materials high surface-to-volume ratio are used in applications, since surface defects represent an active adsorption site and are expected to affect the photocatalytic activity [90, 91].

The details of charge trapping at impurities and defects in TiO_2 has been addressed by several studies, which suggested that in this material electrons and holes are trapped at the sample surface [92–100]. Nevertheless, the identification of defect and impurity bands is still debated [101, 102]; in this regard, the main limitation of visible spectroscopies is their poor sensitivity to charge carrier trapping, which lacks of a clear spectral fingerprint in these region.

Another important aspect of the physics of this material is that, different to conventional band insulators, in anatase TiO_2 the electron-phonon interaction becomes relatively strong, and has often been invoked to interpret experimental results naturally pointing to the polaronic (self-trapped) picture [103–109]. In this regard, insightful information is provided by time-resolved photoluminescence, which revealed a strongly Stokes-shifted emission in the visible range assigned to self-trapped excitons and/or charges trapped at defects [110–115]. However, these processes were found to emerge only at low temperatures and to disappear at RT.

Overall, the material's optical response is dominated by a free-carrier Drude response and by absorption features attributed to localized charges trapped at impurity and/or defect centres, with large variability depending on the sample considered. However, the photophysical picture provided by THz and visible studies is somehow inaccurate or incomplete. In fact, TiO_2 is an indirect-gap insulator with the fundamental absorption edge lying in the UV spectral region (E_g = 3.2 eV), limiting the sensitivity of lower-energy probes to intraband transitions and defect states.

Importantly, in the interpretation of the experimental data, the role of e-h correlation at RT has been often neglected. Although the free-carrier picture was supported by the large static dielectric constant ($\epsilon_S \approx 22/45$ [116, 117]), which suggests significant e-h Coulomb screening, these hypotheses did not account for the frequency-dependence of the dielectric function, nor for the details of the band structure [87]. In light of the existence of bound excitons, the assumption of uncorrelated photoexcited species only holds in the case of non-resonant band-to-band excitation [18]. Given the importance of interactions and correlations in this material, the excitonic states in anatase TiO_2 are expected to have a pronounced influence on the photophysics. On the other hand, as presented in Section 1.2, the e-h Coulomb interaction is very sensitive to the presence of other quasiparticles in the systems, which influence the strength of the Coulomb attraction and modify the optical properties of the material via strong optical nonlinearities.

Thanks to the availability of the ultrafast UV spectroscopies (Section 2.1.2), monitoring the photoinduced dynamics directly at the band edge is now possible, and opens the door to the study of interaction between elementary excitations and many-body effects in wide-gap insulators. The potentiality of this approach is demonstrated by our recent ultrafast studies

on TiO_2 NPs, where the spectral region of the interband transition is probed for the first time by the use of broadband UV pulses and energy-tunable excitation. In particular, because of the peculiar band structure of anatase TiO_2, the PSF due to electrons in the CB (rather than holes in the VB) has been identified as the main mechanism behind exciton bleaching upon avobe-gap photoexcitation [18]. The effectiveness of exciton bleaching as a probe of an electron density in the CB allowed to measure the timescale for electron cooling in the CB; this process was found to occur in <50 fs, due to the strong electron-phonon coupling which leads to an efficient and fast transfer of electron excess energies to the phonon bath within a few tens of fs [18]. Moreover, monitoring the exciton bleaching has been proven to be an elegant substrate-specific method to study the dynamics of interfacial electron injection from a dye to TiO_2, and can be applied to any combination of TMO/sensitizer, also in case of solid-state sensitizers [88].

Thanks to time-resolved UV spectroscopies in the UV, some light was also shed on the hierarchy of exciton nonlinearities at play upon above-gap photoexcitation, which is a topic of relevance for the work of this thesis. In fact, as the bleaching of the exciton state depends on the presence of all the particles in the material [118, 119], insightful information on single-particle and many-body effects can be decoded in the transient excitonic features. In Ref. [18], a slight broadening of the exciton linewidth with increasing carrier density was observed in TiO_2 NPs, and assigned to the presence of long-range CS. Although this effect is also expected to lead to a reduction in exciton binding energy, no blue shifts in the peak energy position, nor derivative-like shapes were detected in the experiment, suggesting that at all the explored densities an exact cancellation of the effects of CS and BGR on the excitonic resonances takes place. In Chapter 4, we will see how in highly-excited anatase TiO_2 single crystals this compensation is no more valid, and a sizeable shift of the exciton peak is instead detected.

Finally, the role of exciton-phonon coupling in TiO_2 deserves special attention. Thanks to the robustness of excitonic species and their strong coupling to the lattice degrees of freedom, this material is an ideal candidate to study how the photoinduced ionic motion modifies the exciton properties at RT. In Ref. [89], it was shown that UV laser pulses can generate coherent acoustic phonons (CAPs) inside spherical anatase TiO_2 NPs. By monitoring the changes in the exciton properties via time-resolved UV spectroscopy, it was observed that the CAPs induce selective modulation of the oscillator strength, without affecting the peak energy position. In Chapter 5, we will show that CAPs can be also generated in TiO_2 single crystals, this time resulting in important modulations of the exciton properties.

2 Materials and Methods

This Chapter provides an overview on the experimental techniques and synthesis of materials relevant for the work presented in this thesis. In Section 2.1, we present the ultrafast spectroscopy set-ups used for our measurements, *i. e.* broadband VIS transient reflectivity (TR) and 2D-UV/VIS TR. The synthesis of the $CH_3NH_3PbBr_3$ and anatase TiO_2 materials is the focus of Section 2.2.

2.1 Ultrafast spectroscopy

2.1.1 Ultrafast broadband reflectivity

The experiments presented in Chapter 3 are performed using an ultrafast broadband reflectivity set-up, which is shown schematically in Figure 2.1 and described in details in Refs. [120–124]. A Ti:Sapphire oscillator, pumped by a continuous-wave Nd:YVO_4 laser, delivers sub-50 fs pulses at 1.55 eV with a repetition rate of 80 MHz. The output of the oscillator seeds a cryo-cooled Ti:Sapphire amplifier, which is pumped by a Q-switched Nd:YAG laser. The amplified laser system provides 45 fs pulses at 1.55 eV and a repetition rate of 6 kHz. One third of the output, representing the probe beam, is sent to a motorized delay line to set a controlled delay between pump and probe. The 1.55 eV beam is focused onto a 3 mm thick CaF_2 cell using a combination of a lens with short focal distance and an iris to limit the numerical aperture of the incoming beam. The generated continuum covers the 2.00-2.80 eV spectral range. The probe is subsequently collimated and focused onto the sample through a pair of parabolic mirrors under an angle of 15°. The remaining two thirds of the amplifier output, representing the pump beam, is frequency-doubled with a β-barium borate (BBO) crystal via second harmonic generation (SHG), and directed towards the sample under normal incidence. Along the pump path, a chopper with a 60-slot plate is inserted, operating at 1.5 kHz and phase-locked to the laser system. Both pump and probe beams are focused onto the sample on spots of dimensions 155μm×125μm and 60μm×30μm respectively. The excitation density

impinging on the sample is estimated as:

$$n_{ex} = \frac{F}{h\nu \cdot \lambda_p}(1 - R) \tag{2.1}$$

where F is the pump fluence, $h\nu$ is the pump photon energy, $\lambda_p = 1/\alpha$ the penetration depth, and R is the reflectivity of the sample. All the parameters are evaluated at the pump photon energy.

The sample is mounted inside a closed cycle cryostat. The reflected probe is dispersed by a fiber-coupled 0.3 m spectrograph and detected on a shot-to-shot basis with a linear CMOS array. In a typical experiment, the acquisition of each data set is repeated multiple times to improve the statistics of the measurement. Hence, the experiment strongly relies on the repeatability of the scans, which requires stability of the sample under laser light illumination for several hours. Before the data analysis, the $\Delta R/R$ matrix has to be corrected for the group velocity dispersion (GVD) of the probe. Since the probe beam is not dispersion-compensated after generation of the white light continuum, the probe pulses arrive at the sample stretched to a duration of few ps. This is beneficial for the experiment, because it significantly reduces the instantaneous probe light intensity on the sample. Importantly, the probe beam dispersion is not a limiting factor for the time resolution of the set-up, which is given on the detection side by the much smaller effective pulse duration per detector pixel. As such, the time resolution of the set-up for all probe photon energies is 50 fs. Finally, we devoted particular attention in maintaining the sample under controlled environmental conditions to avoid its degradation or contamination. To this aim, all measurements were performed at RT, while keeping the crystal in the cryostat under a pressure $< 10^{-8}$ mbar. The temperature was also periodically cycled to avoid artefacts from residual molecules adsorbed on the surface. Finally, the differential change in reflectivity $\Delta R/R(\omega, t)$ is extracted from the data using the expression:

$$\frac{\Delta R}{R}(\omega, t) = \frac{R_{\text{pumped}}(\omega, t) - R_{\text{unpumped}}(\omega)}{R_{\text{unpumped}}(\omega)} \tag{2.2}$$

2.1.2 Ultrafast broadband 2D-UV/VIS spectroscopy

The extension of broadband pump-probe techniques towards the multidimensional scheme allows to study the response of a system under different conditions of photoexcitation [125]. Moreover, the capabilities of exciting and probing the system in both the VIS and UV spectral region opens to the study of wide-gap insulators as transparent conducting TMOs [18, 87–89]. Such ultrafast UV set-up with tunable UV pump and broadband UV probe (presented schematically in Figure 2.2(a)) has been developed as detailed in Refs. [126, 127], and is used to perform the time-resolved reflectivity measurements presented in Chapters 4 and 5.

The laser system is based on a 20 kHz Ti:Sapphire regenerative amplifier which provides 50 fs pulses at 1.5 eV and energy of 0.5 mJ. The output pumps a noncollinear optical parametric

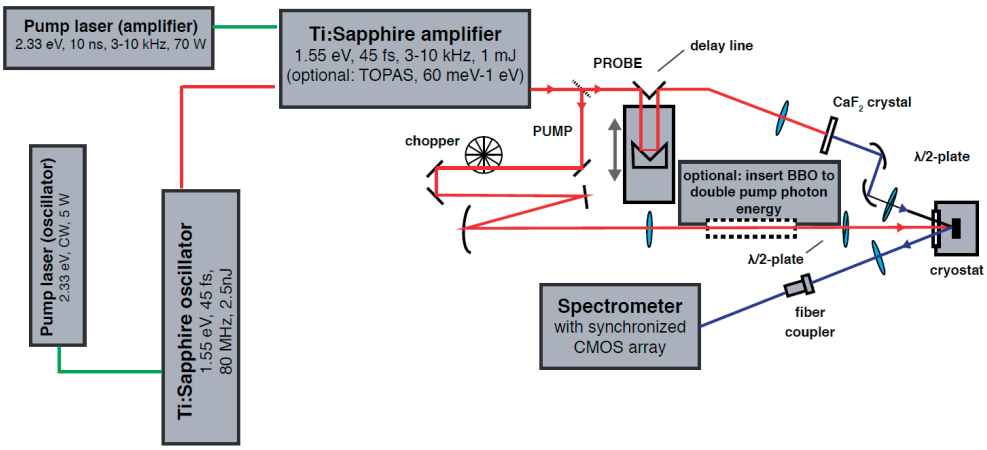

Figure 2.1 – Diagram of the laser system and pump-probe scheme in the ultrafast broadband reflectivity set-up. Reproduced from Ref. [120].

amplifier (NOPA) which generates visible pulses (1.77-2.30 eV) with a duration below 90 fs and typical energy of 13 μJ. Around half of the NOPA output is used to generate the narrowband pump pulses. The beam passes through a chopper operating at 10 kHz and focussed on a 2 mm thick BBO crystal to generate the UV pump pulses via SHG, with typical bandwidth of 20 meV and 120 nJ energy. A photodiode performs shot-to-shot tracking of the pump power, which is used to renormalize the data.

The remaining visible output of the NOPA is used for generating the broadband probe with an achromatic frequency doubling scheme, depicted schematically in Figure 2.2(b). Here, a couple of silica prisms spatially disperse and then recollimate the visible beam, which is then focused on a 200 μm thick BBO crystals with a parabolic mirror. In this stage, each frequency is impinging on the BBO with the phase-matching angle for SHG. The frequency-doubled beam is then recollimated and recombined by a parabolic mirror and other two CaF_2 prisms. The outcoming broadband UV beam is then focused on the sample and spatially overlapped with the excitation beam, as depicted schematically in Figure 2.2(c). The pump and probe spot diameters are approximately 100 μm and 40 μm. The experiments can be performed in both transmission (thin films, colloidal solutions) and reflection geometry (single crystals and reflecting samples). For our studies, the set-up was used in the reflection geometry. The specimens were mounted on a rotating sample holder, in order to explore the transient reflectivity along the desired crystalline axis.

A motorized delay stage introduces a temporal delay between pump and probe pulses; after interaction with the sample, the transmitted or reflected probe beam is focuses in a 100 μm multimode optical fiber coupled to the entrance of a 150 gr/mm grating. The beam is then imaged on a CMOS linear sensor (512 pixels) with 50 MHz pixel readout that allows easy shot-to-shot detection. The typical temporal resolution is 150 fs, which can be reduced to 80 fs at the expenses of a reduction in probe bandwidth. Also in this case, it is necessary to correct the $\Delta R/R$ matrix for the GVD of the probe before the data analysis.

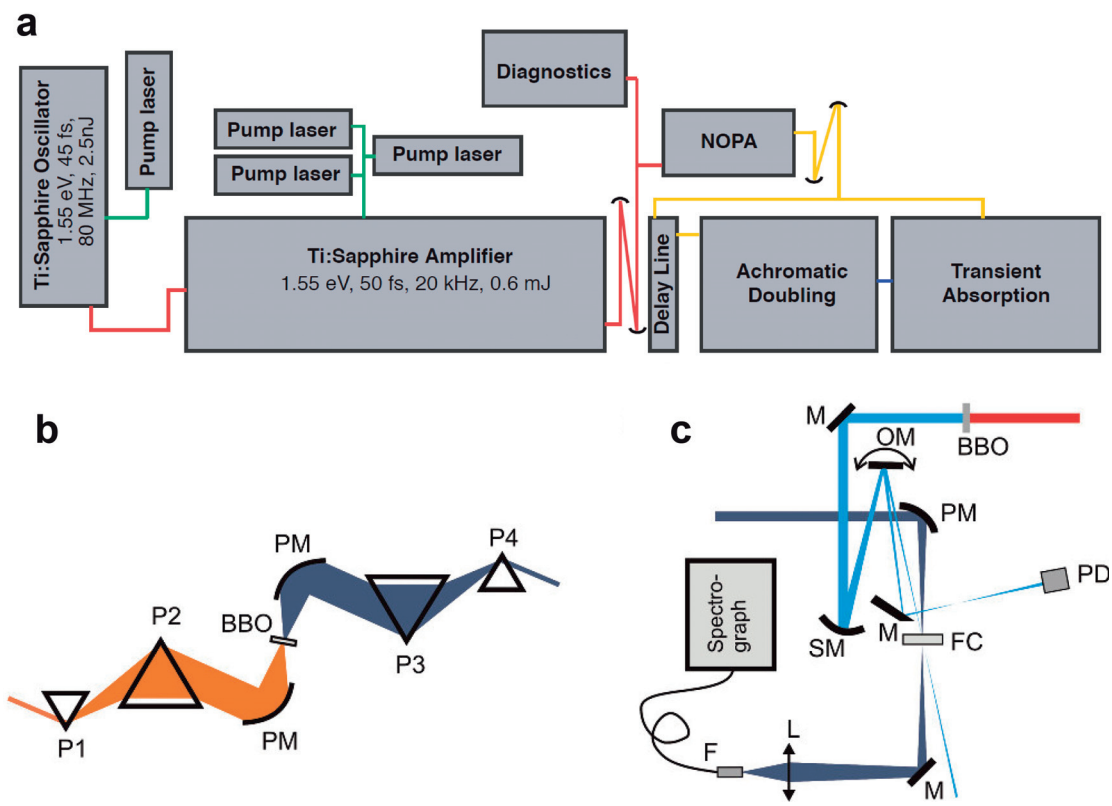

Figure 2.2 – (a) Diagram of the ultrafast UV-VIS spectroscopy set-up and details of the laser system. (b) Schematic of the achromatic doubling. (c) Sample environment. (P=prism, M=mirror, PM=off-axis parabolic mirror, SM=spherical mirror, PD=photodiode, L=lens, F=multimode fiber). Readapted from Refs. [127, 128].

2.2 Materials

2.2.1 $CH_3NH_3PbBr_3$

High-quality single crystals of $CH_3NH_3PbBr_3$ (typical size: 2-3 mm) were provided to us by Dr. Márton Kollár and Dr. Endre Horváth (Forró's group, EPFL). The crystals were synthesized by solution growth and are shown in Figure 2.3. The 3.3 mmol lead (II) acetate trihidrate ($Pb(ac)_2 \times 3H_2O$, >99.9%) was reacted with 6 ml saturated HBr solution (48 wt% HBr in H_2O). The formed $PbBr_2$ precipitate is stable in the acidic solution. The respective amount (3.30 mmol) methylamine (CH_3NH_2) solution (40 wt% in H_2O) was pipetted into the 5 °C ice cooled solution of $PbBr_2$. Orange coloured microcrystallites of $CH_3NH_3PbBr_3$ were formed immediately and settled down at the bottom of the vessel. In a temperature gradient of 15 °C in the acidic media, large (3–10 mm) intergrown orange, transparent crystals were formed in 7–10 days.

After removing the crystals from the solution, they were dried on laboratory paper wipes at RT followed by 30 minutes air drying at 150 °C on a hot plate. During this heat treatment the

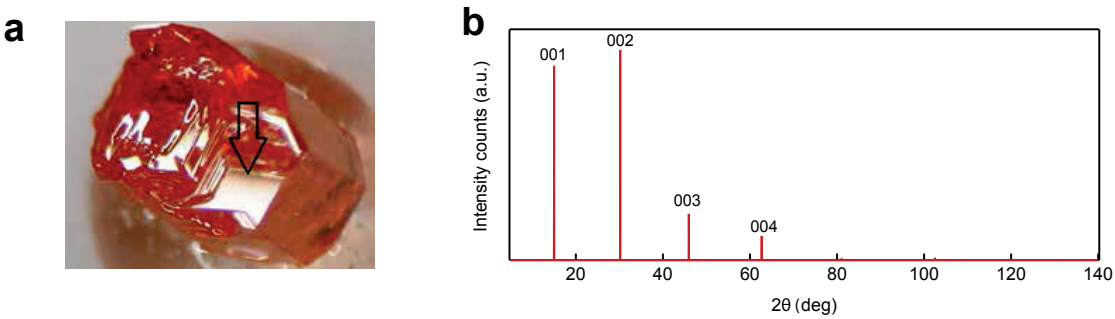

Figure 2.3 – Single crystals of $CH_3NH_3PbBr_3$ single crystals (typical size: 2-3 mm) showing a highly reflective surface. The X-ray diffraction pattern demonstrate the high crystallinity of the sample and the absence of any degradation.

colour of the crystals changed from light orange to dark orange-red. Shiny surfaces could be obtained by applying a mechanical stress (using tweezers or a blade) on a previously baked clusters of twinned crystals. Such a surface is highly advantageous in measurements requiring flat, non-contaminated surfaces, as in the case of reflectivity measurements.

At RT, $CH_3NH_3PbBr_3$ has a cubic crystal structure; the X-ray diffraction pattern demonstrate the absence of any degradation and the sharp diffraction peaks that prove the high crystallinity of the sample. Further details on the synthesis can be found in Ref. [129].

2.2.2 Anatase TiO_2

High-quality single crystals of anatase TiO_2 were grown by Dr. Helmuth Berger (Crystal Growth Facility, EPFL) via a chemical transport method from anatase powder and NH_4Cl as transport agent. In detail, 0.5 g of high-purity anatase powder were sealed in a 3 mm thick, 2 cm large and 20 cm long quartz ampoule together with 150 mg of NH_4Cl, previously dried at 60 °C under dynamic vacuum for one night, and 400 mbar of electronic grade HCl. The ampoules were placed in a horizontal tubular two-zone furnace and heated very slowly to 740 °C at the source, and 610 °C at the deposition zone. After two weeks, mm-sized crystals with a bi-pyramidal shape (Figure 2.4(a)) were collected and cut into rectangular bars (typically $0.8\times0.6\times0.15\text{mm}^3$). Because of oxygen vacancies, the crystals are naturally n-doped and appear black. The doping level was determined via ARPES and transport measurements to be $n = 2\times10^{19}\text{cm}^{-3}$.

The pristine form of anatase TiO_2 was instead obtained by annealing the raw anatase TiO_2 crystals at 700 °C for 10 days under 950 mbar of CO; in this case, the doping is absent ($n \sim 0$) and the crystals are transparent (Figure 2.4(b)). Further details on the synthesis can be found in Ref. [130].

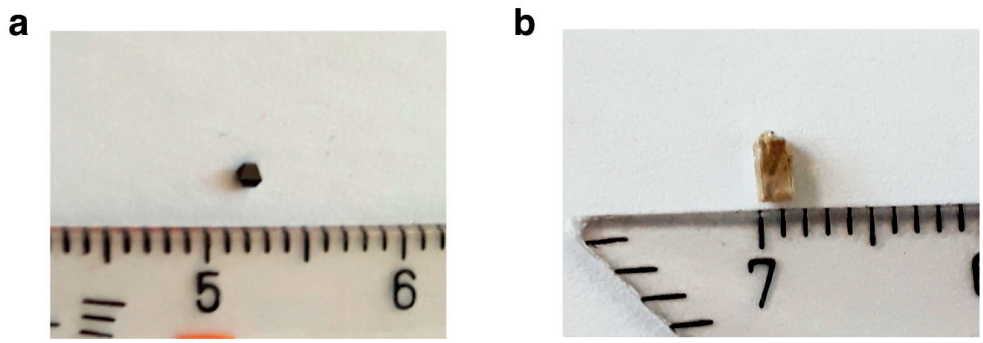

Figure 2.4 – Single crystals of anatase TiO_2: (a) raw samples (n-doping level is $n = 2 \times 10^{19} cm^{-3}$) and (b) pristine sample (after annealing: $n \sim 0$).

3 Excitonic correlations above the Mott density in $CH_3NH_3PbBr_3$

This Chapter presents our result on excitonic correlation in highly excited $CH_3NH_3PbBr_3$ ($MAPbBr_3$) single crystals. Here, we combine different experimental techniques and theory calculations to show that signatures of e-h correlations still persist in the response of $MAPbBr_3$ single-crystals photoexcited above the nominal Mott density. In particular, state-of-the-art many-body theory is used to calculate the exciton ionization ratio and provide a precise estimate of the Mott density. Then, in our pump-probe experiments, we induce a carrier density above this critical density and monitor the photoinduced changes in reflection, which are related to the renormalization of the excitonic states upon the interaction with the photogenerated e-h plasma. Via lineshape analysis, we calculate the evolution of the absorption coefficient in time, finding the persistence of the exciton feature with finite oscillator strength. Finally, we calculate the absorption coefficient for different excitation densities by solving the semiconductor Bloch equations for $MAPbBr_3$ crystals. These results reveal the presence of e-h correlations in these materials in a regime where the complete dissociation is expected, revealing the robustness of these collective excitations against high e-h densities.[1].

3.1 Introduction

Revealing the strength of e-h correlations in hybrid organic-inorganic perovskites is a topic of pivotal importance for a wide class of applications based on these materials, having a dramatic impact on the device design and operation. In photovoltaic technologies, the presence of excitons affects the charge transport and prevents efficient e-h dissociation at the heterojunction. On the other hand, a substantial exciton binding energy (E_b) is desirable in light-emitting devices, as a higher E_b) results in larger e-h capture rates for radiative recombination [28, 55]. Excitons also play a role in perovskite-based spintronics, as the manipulation of the spin degrees of freedom of the bound species in Rashba-split semiconductors is key to the development of spin-polarized circuits [56–58]. Because of the relevance of the subject,

[1] Tania Palmieri*, Edoardo Baldini*, Alexander Steinhoff, Ana Akrap, Márton Kollár, Endre Horváth, László Forró, Frank Jahnke & Majed Chergui, *"Mahan excitons in room-temperature methylammonium lead bromide perovskites"*. Submitted.

numerous studies have focused on understanding the extent to which the exciton scenario describes the physics of these materials [47, 60, 62, 66]. In $MAPbI_3$, exciton binding energies of the order of $k_B T$ were reported at RT, suggesting the presence of free-carriers as photoexcited species in the operating photovoltaic device [17, 62, 73]. Well-resolved excitonic resonances dominate instead the RT electrodynamics of $MAPbBr_3$ (E_b = 60-70 meV) because of its smaller dielectric constant; here, the thermal energy alone is not sufficient to dissociate the bound states [64, 77, 78].

While the influence of thermal effects on the exciton stability has been extensively investigated, less explored is the fate of the e-h correlations in the presence of other perturbations that are actively at play in devices, the most important being the photoexcited carrier density. In particular, the most dramatic effect accompanying the presence of high carrier densities is the transition from an insulating exciton gas into a fully ionized e-h plasma, which is typically referred to as the Mott transition [13] and has been previously introduced in Section 1.2.4. A different scenario predicts that, in the high-density limit, e-h Coulomb correlations can still be present and prevent the complete formation of a metallic phase. In this alternative hypothesis put forth by Mahan, excitonic states do not disappear above n_M but rather merge into a persisting exciton continuum [131–133]. The new bound state, dubbed as Mahan exciton, enhances the oscillator strength close to the Fermi edge, causing the excitonic absorption peak to persist against increasing excitation densities [134].

The insulator-to-metal transition in hybrid perovskites has been addressed by various studies, which estimated critical Mott densities (n_M) for $MAPbI_3$ in the order of 10^{16}-10^{18}cm^{-3} based on the comparison between the exciton Bohr radius and the screening length induced by the free carriers [68, 135, 136]. Similar values can be estimated for $MAPbBr_3$, resulting in a superior limit to n_M of $\sim 2 \times 10^{18}$cm^{-3} (see Section 3.3). Nevertheless, the exact value of n_M remains an argument of discussion, due to the large variations of critical densities depending on the model assumptions, which usually yield to over- or underestimation of n_M by one or two orders of magnitude [6]. In fact, a severe limitation of these models is that many-body effects are not fully included. As a result, a sophisticated many-body theory is required to describe the interaction between a dense e-h plasma and the excitonic states, and finally provide a precise estimate of the excitation densities at which the insulator-to-metal transition occurs.

In the following, we address the complex interplay between excitons and unbound e-h pairs in highly photoexcited single crystals of $MAPbBr_3$ through a combination of ultrafast broadband optical spectroscopy and state-of-the-art many-body calculations. After providing a precise estimate of n_M by means of the ionization equilibrium theory, we illuminate a $MAPbBr_3$ crystal with an intense ultrashort laser pulse in order to induce carrier densities well above n_M. The use of a spectrally-broad optical probe covering the exciton resonance allows us to reveal the persistence of the exciton peak and the enhancement of the above-gap absorption for densities well above n_M. These observations are rationalized by solving the Semiconductor Bloch Equations, indicating that no sharp transition between the insulating and conductive

phase occurs in $MAPbBr_3$. Conversely, a crossover between the two phases is established, which is characterized by the emergence of Mahan exciton states. Our results remark the critical role of e-h correlations in a regime where complete exciton dissociation would be otherwise expected, proving the robustness of these fundamental excitations against high e-h densities.

3.2 Equilibrium optical spectra

We first characterize the steady-state optical properties of the crystals at RT using spectroscopic ellipsometry in the 1.00-5.00 eV spectral range. Figure 3.1 shows the real ($\epsilon_1(\omega)$, blue dots) and imaginary ($\epsilon_2(\omega)$, red dots) parts of the dielectric function. From these quantities, we calculate the absorption coefficient $\alpha(\omega)$ of our sample, shown in dots in Figure 3.2. It features a sharp peak at 2.35 eV, corresponding to the lowest direct charge excitation of the material, and a continuum extending to higher energies [64, 77, 137, 138].

We apply Elliott theory to describe the absorption onset of the material, assuming the presence of Wannier-Mott exciton states (see Section 1.1.2). We convolute Equation (1.11) with an hyperbolic secant to account for phenomenological broadening Γ, and introduce a term to correct for non-parabolic band dispersion [63]:

$$\begin{aligned}\alpha(h\nu) = \frac{|d_{\mathrm{cv}}|^2(2\mu)^{3/2}}{\epsilon_0\hbar n_b c}E_b^{1/2}h\nu\Bigg\{\sum_{n=1}^{\infty}\frac{2E_b}{n^3}\operatorname{sech}\left(\frac{h\nu - E_g + E_b/n^2}{\Gamma}\right) + \\ + \int_E^{E_g}\operatorname{sech}\left(\frac{E-x}{\Gamma}\right)\frac{1}{1-e^{-2\pi\sqrt{\frac{E_b}{x-E_g}}}}\frac{1}{1-\frac{8\mu b}{\hbar^3}(x-E_g)}dx\Bigg\}\end{aligned} \tag{3.1}$$

The fit to the absorption spectrum, shown as solid line in Figure 3.2, yields E_b = 71 meV, linewidth Γ = 34 meV, single-particle gap energy E_g = 2.42 eV, and non-parabolicity factor $8\mu b/\hbar^3$=0.50 eV^{-1}, in excellent agreement with previous reports [64, 77].

3.3 Estimation of the critical Mott density

3.3.1 Mott criterion

We now use the extracted E_b to estimate n_M in $MAPbBr_3$ single crystals and compare with the results of the literature. As presented in details in Section 1.2.4, depending on the assumptions of the model, different expressions for n_M can be used to describe the insulator-to-metal transition, which give values in the range 10^{16}-10^{18}cm^{-3} for RT $MAPbI_3$ [68, 135, 136]. In all these equations, the knowledge of the dielectric constant is required; however, because in HOPs the dielectric function changes by orders of magnitude with the frequency, it is not straightforward to know which $\epsilon(\omega)$ should be used [17]. The choice should take into account the dynamic screening, and compare the relative magnitudes of E_b and the longitudinal optical

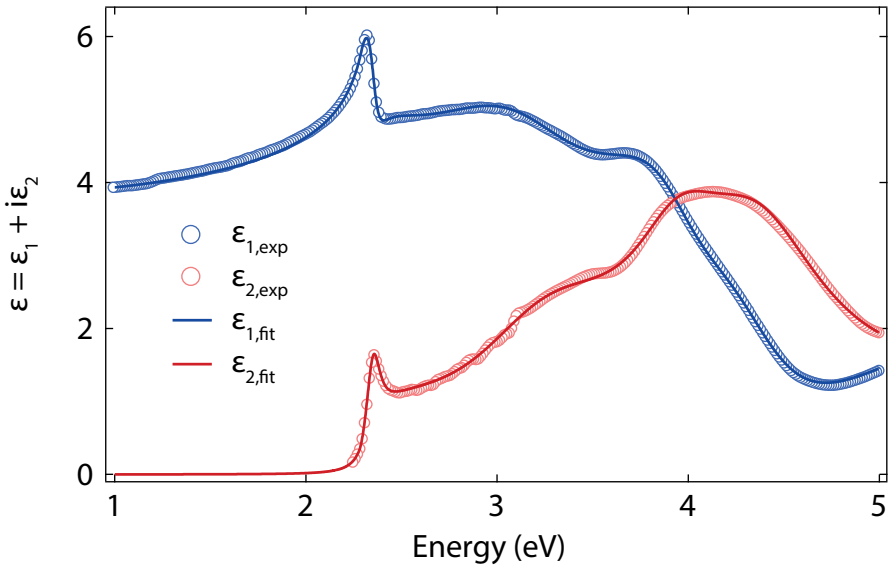

Figure 3.1 – Complex dielectric function of $MAPbBr_3$ single crystals measured by spectroscopic ellipsometry. The experimental data of the real (blue) and imaginary (red) parts of the dielectric function are represented by dots. The solid lines are the results of the Tauc-Lorentz model fit.

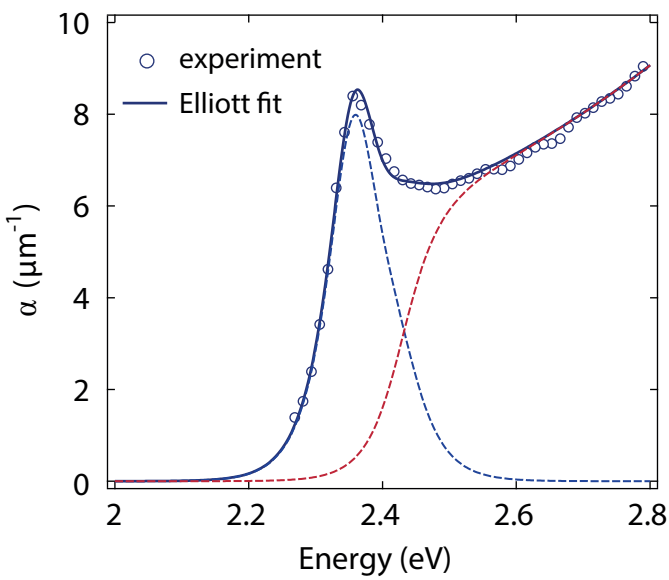

Figure 3.2 – Absorption spectrum of $MAPbBr_3$ single crystals as calculated from the ellipsometry data (dots), fitted with Elliott theory (solid line) and resulting in $E_b = 71$ meV, linewidth $\Gamma = 34$ meV, single-particle gap energy $E_g = 2.42$ eV, and non-parabolicity factor $8\mu b/\hbar^3 = 0.50$ eV^{-1}. The blue and red dotted lines represent the distinct contributions of the exciton and the continuum respectively.

(LO) phonon mode energy $\hbar\omega_{LO}$. In particular, if $E_b < \hbar\omega_{LO}$, the value of ϵ to be considered is the static one ϵ_s; if $E_b \gtrsim \hbar\omega_{LO}$, lattice polarization will only partially follow the e-h motion, and value between ϵ_s and ϵ_b should be used [6]. In the case of hybrid perovskites, the uncertainty on the low-frequency values of $\epsilon(\omega)$, as well as LO phonon energies comparable to exciton binding energy hinders the identification of the main screening mechanism [139]. For ϵ_s, values as high as 60 have been reported [140], and binding energies ranging from 2 meV to 75 meV has been extracted with different methods [17]. Here, we extract an effective dielectric constant ϵ_{eff} from the expression of the exciton binding energy

$$E_b = \frac{\mu e^4}{2\hbar(\epsilon_{\text{eff}}\epsilon_0)^2} \tag{3.2}$$

From the experimental value of E_b=71 meV, and assuming $m_e^* = 0.22m_e$, $m_h^* = 0.25m_e$, $\mu = 0.117m_e$ as determined from previous GW calculations [51], we estimate $\epsilon_{\text{eff}} = 4.73$ and an exciton Bohr radius a_B=2.14 nm.

By using the Mott criterion of Equations (1.27) and (1.29), we find for our $MAPbBr_3$ single crystal Mott densities of

$$n_{M,\,1.27} = 1.19^2 \frac{k_B T}{2a_B^3 E_b} = 2.01 \times 10^{18}\text{cm}^{-3} \tag{3.3}$$

$$n_{M,\,1.29} = a_B^{-3} \frac{\pi 1.19^6}{4^3 \times 3} \left(\frac{m_e m_h}{(m_e + m_h)^2} \right)^3 = 7.31 \times 10^{16}\text{cm}^{-3} \tag{3.4}$$

Moreover, to take into account the uncertainty on the material parameters, we also explore the dependence of the Mott density with various combinations of μ and ϵ_{eff} for the experimental binding energy E_b =71 meV. The results are shown in Figure 3.3 for $n_{M,\,1.27}$ (solid lines) and $n_{M,\,1.29}$ (dashed lines). The exciton reduced mass μ varies from $0.06m_e$ (red line) to $0.18m_e$ (purple line), while the black vertical line corresponds to the ϵ_{eff} extracted in this work, which intersect the curves corresponding to $\mu = 0.12m_e$. Taking into account the variability of parameters and even considering extremely high reduced masses and extremely low effective dielectric constant, the upper limit for the critical density is $n_M \approx 2 \times 10^{19}\text{cm}^{-3}$.

3.3.2 Degree of ionization

We now make use of a more sophisticated approach to calculate the degree of ionization in the framework of the ionization equilibrium theory, as outlined in Ref. [141] (see Appendix A.1). All the theoretical calculations presented in this Chapter are performed by Dr. Alexander Steinhoff and Prof. Frank Jahnke (University of Bremen). In general, e-h pairs that are optically excited in a semiconductor can form either a plasma of unbound carriers or a gas of bound excitons, with all possible states of coexistence of the two phases depending on the experimental parameters. To determine the density at which excitons are fully ionized into an unbound yet correlated e-h plasma, the theory builds on a many-body description of the optically excited exciton-plasma

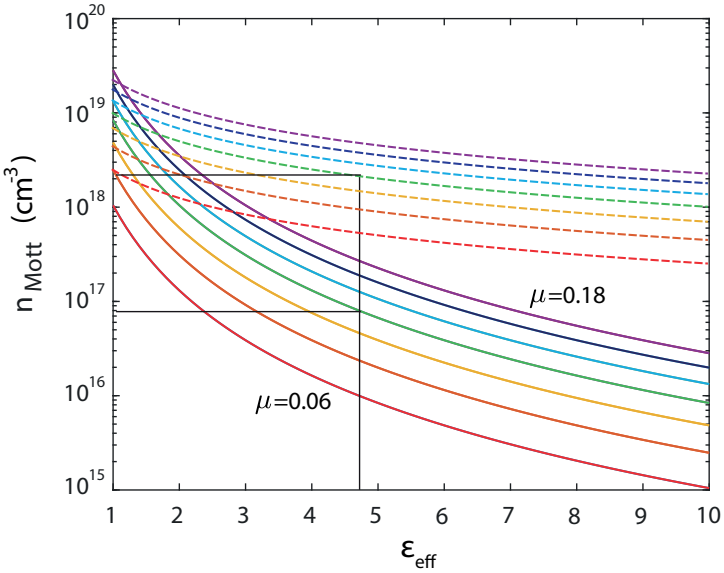

Figure 3.3 – Dependence of the nominal Mott density with respect to various combinations of exciton reduced masses, using the criterion in Equation (1.27) (solid lines) and Equation (1.29) (dashed lines). The exciton reduced mass μ varies from $0.06m_e$ (red line) to $0.18m_e$ (purple line). The black vertical line corresponds to the ϵ_{eff} extracted in this work, which intersect the curves corresponding to $\mu = 0.12m_e$.

conglomerate at a given temperature and excitation density, allowing to calculate the fraction of carriers that exists as plasma or excitons, respectively. The fraction of ionized e-h pairs $\alpha_{eh} = n_{\text{free}}/n$, where $n = n_{\text{free}} + n_X$ is the total density of e-h, is shown in Figure 3.4 as red dots.

At low carrier densities, α_{eh} closely follows the ionization ratio predicted by the mass-action law (Saha-Langmuir equation, blue curve in Figure 3.4). According to this law, a balance exists between e-h dissociation and recombination events. Saha equation predicts the formation of excitonic species for increasing n following the expression:

$$\frac{\alpha^2}{1-\alpha} = \frac{1}{n\lambda_T^3}\exp\left(\frac{-E_b}{k_B T}\right) \tag{3.5}$$

where $\lambda_T = h/\sqrt{2\pi\mu k_B T}$ is the thermal de Broglie wavelength.

However, we see from Figure 3.4 that at $n \sim 5\times10^{17}\text{cm}^{-3}$ the two curves start deviating, and at a certain threshold α_{eh} from the TIE abruptly increases to 1. Here, many-particle renormalization and Coulomb screening lead to full exciton ionization at $n_M \sim 8\times10^{17}\text{cm}^{-3}$, which we identify as the critical Mott density for $MAPbBr_3$ single crystals. In the following, we aim to study the behaviour of the exciton transition in the Mott crossover regime by photoinducing high charge carrier densities in this material.

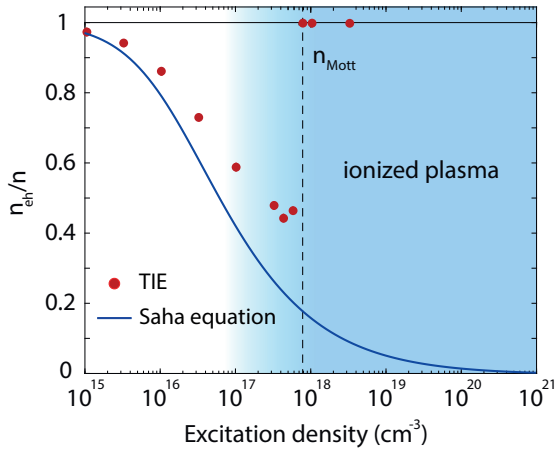

Figure 3.4 – Exciton ionization ratio as a function of the photoexcitation density, where $\alpha = 0$ corresponds to an exciton gas and $\alpha = 1$ to a fully ionized plasma, as calculated from the theory of ionization equilibrium (TIE, red dots). The vertical line indicates the Mott critical density, found for $n_M \sim 8 \times 10^{17}\text{cm}^{-3}$. The solid line represents the ionization ratio calculated with Saha equation and has been added for comparison.

3.4 Ultrafast broadband spectroscopy

We now focus on the results of our pump-probe experiment, where we use an intense 3.10 eV pump pulse to create an e-h density above n_M. The details of the experimental setup can be found in Section 2.1. The first column in Figure 3.5 shows the color maps of $\Delta R/R$ as a function of the probe photon energy and the time delay between pump and probe for different excitation energies above n_M (5, 7.5 and $10\times10^{18}\text{cm}^{-3}$). We observe a derivative-like signal, which is positive above and negative below 2.40 eV. For time delays >1 ps, this signal agrees with previous reports at lower excitation densities ($5 \times 10^{17}\text{cm}^{-3}$), where it was assigned to the bleaching of the excitonic feature caused by phase-space filling (PSF) [137]. A closer inspection of our data reveals a complex spectral evolution taking place within the first picosecond. This is better resolved in the second and third columns in Figure 3.5, which show the transient spectra at representative time delays. Specifically, in the first 500 fs (Figure 3.5(b)) the signal amplitude rises with an isosbestic point developing around 2.40 eV, and no shifts of the relative maxima are observed. At longer time delays (Figure 3.5(c)), the response undergoes an asymmetric evolution around the inversion point, accompanied by a sizeable red shift of both the zero-crossing energy and the positive shoulder maximum. This biphasic trend is observed at all the explored e-h densities.

3.5 Global fit analysis

To gain information on the timescales governing the evolution of the spectral features, we perform a global fit of the kinetic traces $\Delta R/R$ (dots in Figure 3.6(a)) obtained from the map in Figure 3.5(a) for 30 different probe photon energies. The traces are fitted with multi-

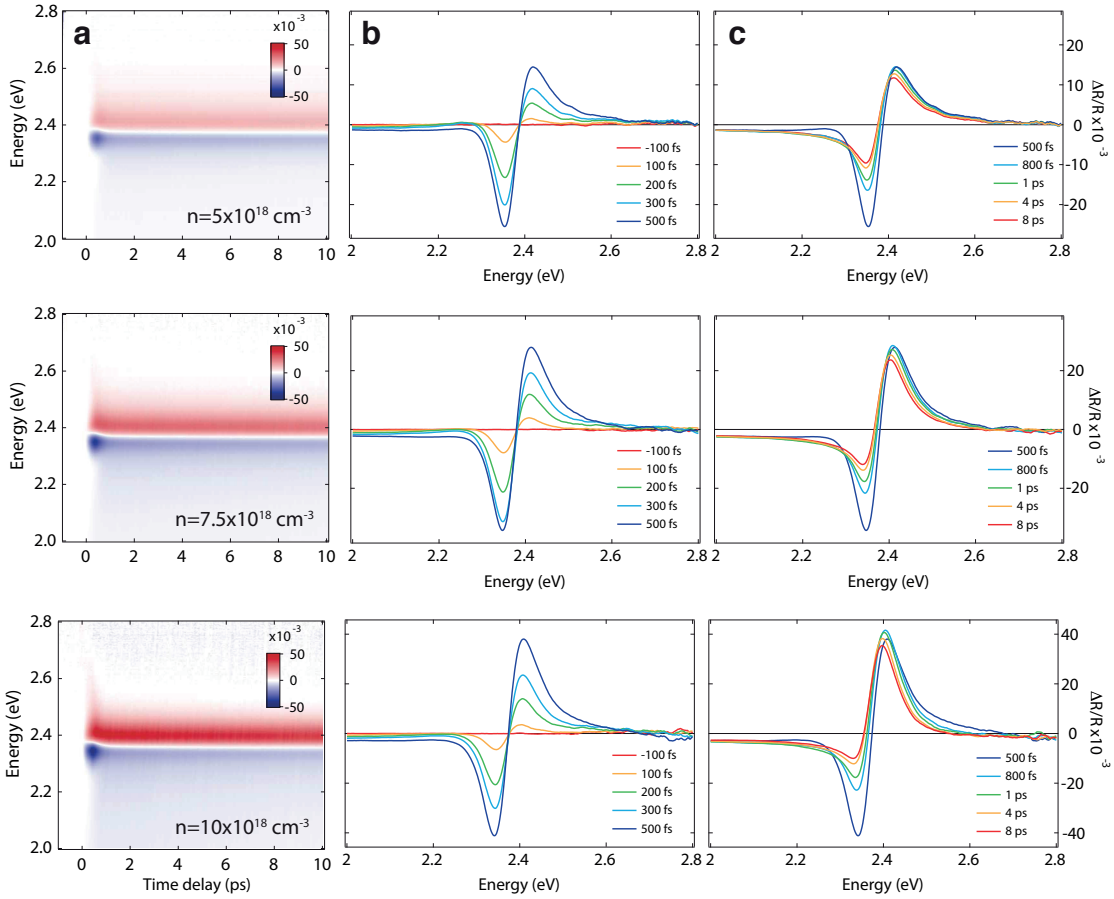

Figure 3.5 – (a) Colour-coded $\Delta R/R$ map as a function of probe photon energy and time delay between pump and probe. The pump photon energy is 3.10 eV and the estimated carrier densities are $n = 5$, 7.5 and $10\times10^{18}\text{cm}^{-3}$. The time resolution is 50 fs. (b, c) $\Delta R/R$ spectra of the temporal windows 0-500 fs and 500 fs-8 ps.

exponential functions of the type

$$\Delta R/R = OS + \sum_{i=1}^{2} A_i \text{erfexp}(\sigma_i, D_i, \tau_i, t) \tag{3.6}$$

In the function, OS is the offset; the erfexp function denotes the convolution between an exponential function with decay constant τ (multiplied by a Heaviside function to account for signal causality) and a Gaussian with full-width at half maximum (FWHM) of 2.35σ, which accounts for the rising part of the signal; A is the amplitude of the exponential; D the delay with respect to zero time delay. We assume that all the kinetic traces are described by the same rising and decay time, whereas we leave the A_i and D_i unlinked during the fit. The fit is shown as solid lines in Figure 3.6(a), while the resulting decay associated spectra (DAS) are shown in Figure 3.6(b) and reveal the presence of two distinct spectral features. We find that the signal rises over the entire spectral range within ~ 500 fs, which is much longer than the 50 fs response function of our set-up. The decay time of the two exponentials are $\tau_1 \sim 300$ fs

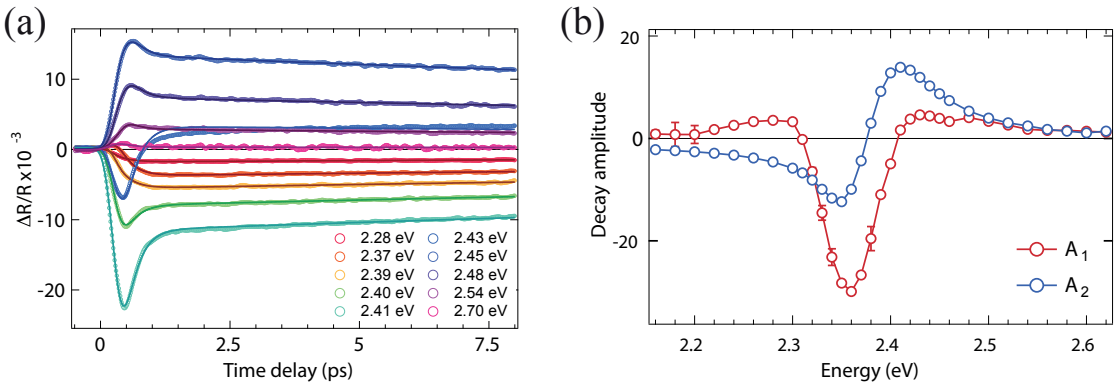

Figure 3.6 – Global fit analysis of transient reflectivity. (a) Kinetic traces extracted from the transient reflectivity data (circles) and their corresponding fit (solid lines). (b) Decay associated spectra for the fast and slow components and corresponding decay constants ($A_1 : \tau_{R1} \sim 325$ fs, τ_{D1} ~307 fs; $A_2 : \tau_{R2} \sim 313$ fs, $\tau_{D2} \sim 45$ ps).

and $\tau_2 \sim 40$ ps. The distinct spectral contributions over the probed energy range is shown in Figure 3.6(b). Here, the associated spectrum of τ_1 shows a main negative peak at 2.36 eV and two symmetric positive features. The DAS of the second exponential is instead characterized by a highly-symmetric derivative-like shape. In conclusion, the global fit analysis highlights the presence of two distinct processes: a fast one, that characterizes the dynamics in the first 500 ps, and a slow one, which evolves beyond the time window of our experiment.

3.6 Lineshape analysis

Although being a powerful tool to disentangle diverse processes occurring with different timescales, the global fit analysis lacks in precision when it deals with spectral renormalization, *i. e.* when the assumption of DAS constant in time does not hold. In particular, by looking at the transient spectra in Figure 3.5, we notice a nonlinear dependence of the signal on the photoexcited e-h density and the presence of energy shifts of isosbestic points which become more relevant with varying excitation densities. However, often this evolution cannot be captured by a simple global fit of the kinetic traces. The knowledge of such spectral renormalization is of pivotal importance to elucidate the nonlinear effects taking place in the material upon photoexcitation, and an alternative route has to be considered with respect of the common approaches to the data analysis to disentangle the renormalization dynamics. For this reason, we develop here an *ad hoc* lineshape analysis to reconstruct the spectro-temporal evolution of the relevant optical quantities and directly visualize the temporal evolution of the relevant parameters, as peak energy and linewidth. The procedure is described in the following.

Table 3.1 – Amplitude, linewidth and peak energy for the Lorentz oscillator and the five TL oscillators modelling the dielectric function of $MAPbBr_3$ single crystals. Other parameters are $\epsilon_\infty = 2.025$ and $E_g = 2.278$ eV.

Oscillator	A	Γ	E_0
Lorentz	0.2483 ± 0.0190	0.0914± 0.0028	2.3514 ± 0.0008
TL1	211.9 ± 0.0889	0.1728 ± 0.0608	2.2464 ± 0.0203
TL2	17.83 ± 0.0011	1.1128 ± 0.0416	3.2122 ± 0.0068
TL3	5.20 ± 0.0004	0.6270 ± 0.0246	3.9441 ± 0.0045
TL4	6.81 ± 0.0003	0.8305 ± 0.0147	4.3677 ± 0.0070
TL5	6.44 ± 0.0005	1.4348 ± 0.1049	6.2195± 0.0532

3.6.1 Tauc-Lorentz fit of the dielectric function

First of all, we fit $\epsilon_1(\omega)$ and $\epsilon_2(\omega)$ simultaneously with a model comprising one Lorentz (L) and 5 Tauc-Lorentz (TL) oscillators describing the excitonic resonance and the continuum, respectively. The fit of $\epsilon_2(\omega)$ is limited to the region 2.22 eV - 5.50 eV due to artefacts of the measurements at lower energies. The analytical expression of $\epsilon_1(\omega)$ and $\epsilon_2(\omega)$ of TL functions can be found in reference [142]. We remark that the simultaneous fit of the real and imaginary parts provides an accurate description of the optical quantities in the energy range of interest and overcomes the issues related to a Kramers-Kronig transformation of one set of data to the other quantity. The results of the fit are shown in Figure 3.1 as solid lines. The oscillator parameters are listed instead in Table 3.1.

3.6.2 Derivation of the time-resolved reflectivity spectra

The transient reflectivity signal $\frac{\Delta R}{R}(\omega, t)$ is defined as

$$\frac{\Delta R}{R}(\omega, t) = \frac{R(\omega, t) - R_s(\omega)}{R_s(\omega)} \tag{3.7}$$

where $R(\omega, t)$ is the reflectivity at the pump-probe delay t and $R_s(\omega)$ is the equilibrium reflectivity spectrum. We assume the latter to be equal to the reflectivity R_s extracted from the ellipsometry data. R_s is shown in Figure 3.7, and is calculated as

$$R_s = \frac{(1-n)^2 + \kappa^2}{(1+n)^2 + \kappa^2} \tag{3.8}$$

where n and k are respectively the real and imaginary parts of the complex refractive index $\tilde{n}(\omega) = n(\omega) + i\kappa(\omega)$:

$$n = \left(\frac{\epsilon_1 + \sqrt{\epsilon_1^2 + \epsilon_2^2}}{2} \right)^{\frac{1}{2}}, \qquad \kappa = \left(\frac{-\epsilon_1 + \sqrt{\epsilon_1^2 + \epsilon_2^2}}{2} \right)^{\frac{1}{2}} \tag{3.9}$$

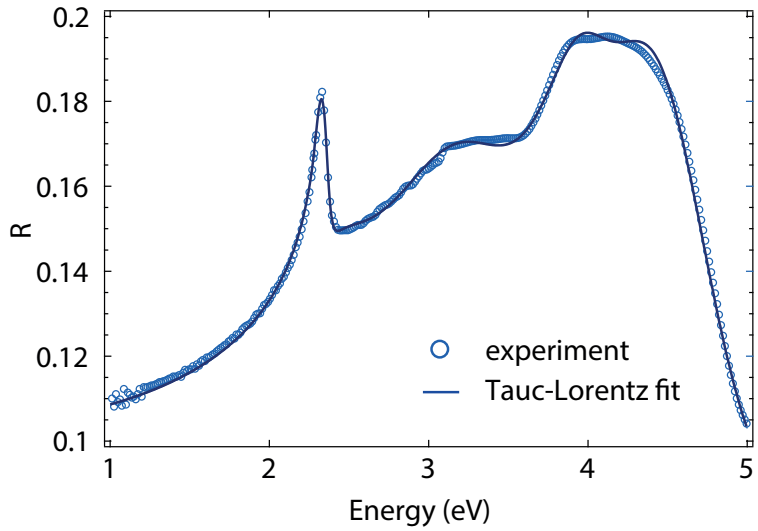

Figure 3.7 – Reflectivity of $MAPbBr_3$ single crystals calculated from the ellipsometry data (dots) overlapped with the fit obtained via Tauc-Lorentz model (solid line).

Finally, we combine our steady-state and time-resolved data and retrieve the time evolution of the reflectivity $R(\omega, t)$

$$R(\omega, t) = R_s(\omega) \times \frac{\Delta R}{R}(\omega, t) + R_s(\omega) \tag{3.10}$$

resulting in the spectra shown in Figure 3.8.

3.6.3 Tauc-Lorentz fit of the reflectivity spectra

Via the TL model of the reflectivity, we can directly relate the changes in reflectivity to the variation of the oscillator parameters. We consider the absolute reflectivity spectra of Figure 3.8 and fit them iteratively within the TL model. We use as starting parameters the steady-state ones; leaving the Lorentz and the first TL oscillator free to vary is sufficient to reproduce well the spectra at all times delays. In this way, we access the evolution of the oscillators parameters, which is presented in Figure 3.9 for the three excitation densities.

3.6.4 Calculation of the time-resolved absorption spectra

Having extrapolated the evolution of the model parameters, the dynamics of any optical quantity of interest can be accessed. In particular, we can retrieve the time-dependent absorption coefficient $\alpha(\omega, t)$, whose evolution during the rise and decay of the response is shown in Figure 3.10. In the first 500 fs, we observe only a $\sim 10-20\%$ decrease of the exciton oscillator strength for the lowest and highest e-h densities respectively, accompanied by a slight red shift of its peak energy E_x. A net broadening of the linewidth Γ is also detected. Remarkably,

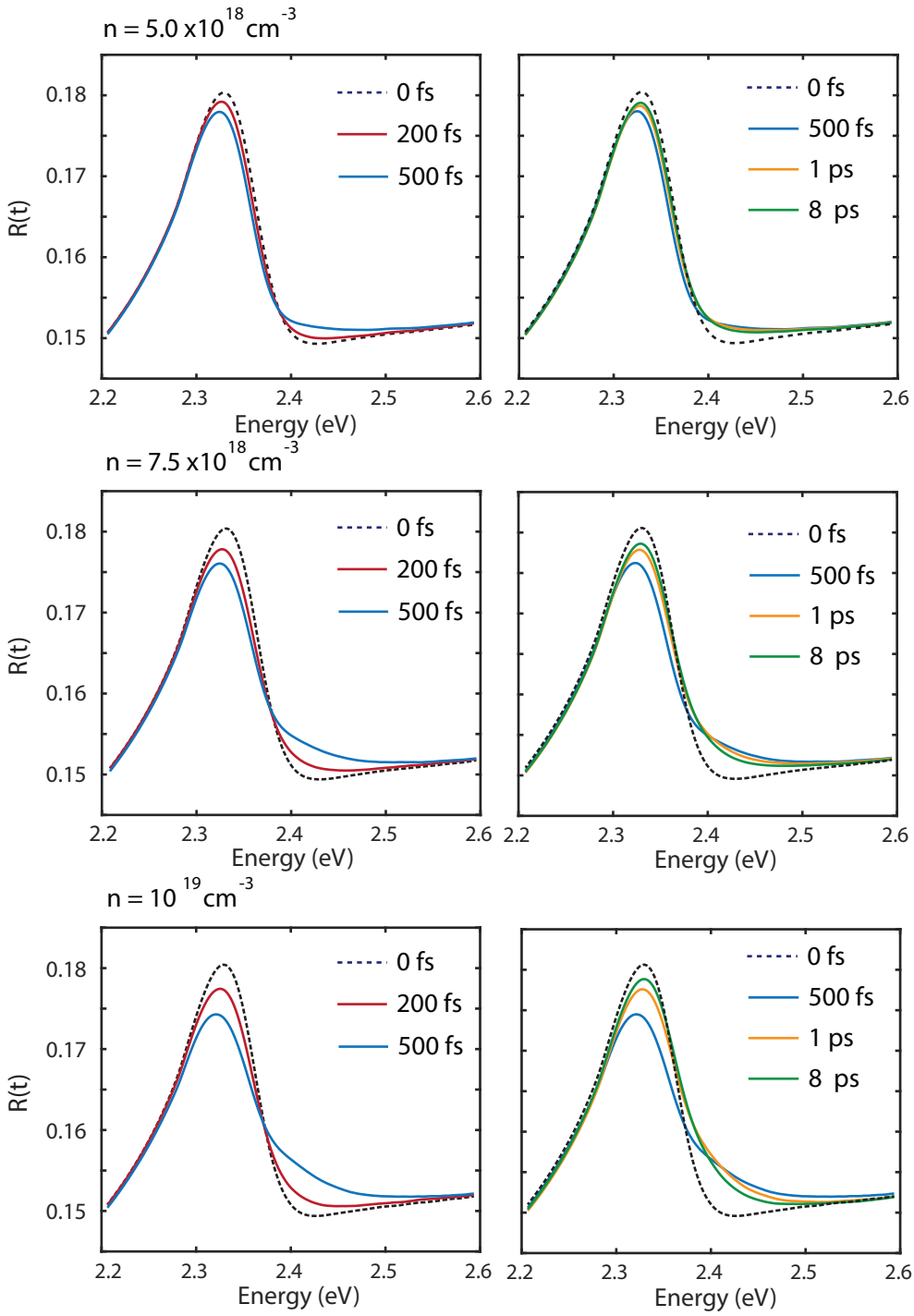

Figure 3.8 – Spectral evolution of $R(\omega, t)$, obtained by combining the steady-state $R_s(\omega)$ calculated from ellipsometry and the $\Delta R/R(\omega, t)$ data in the time windows 0-500 fs and 500 fs-8 ps.

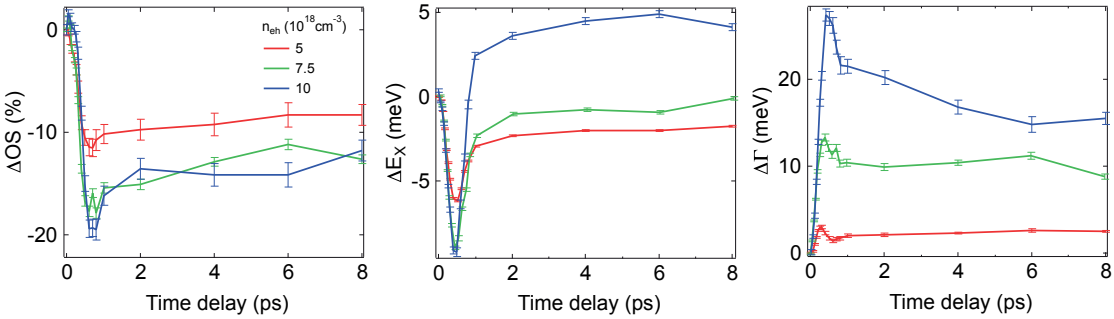

Figure 3.9 – Evolution of (a) oscillator strength, (b) peak energy and (c) linewidth of the first Lorentz oscillator with respect to the equilibrium parameters as obtained by iterating the Tauc-Lorentz fit over the reflectivity for different time delays.

besides this renormalization, the exciton lineshape remains well resolvable. The persistence of the excitons against the photoexcited carrier density is also confirmed by Figure 3.11(a), where we show the absorption spectrum for three different photoexcited densities, at the time corresponding to the maximum photoinduced bleaching (500 fs) and thus to the largest e-h density at the band edge before the recombination sets in. A well-resolved exciton feature is always observed, being very robust to the photoexcited e-h density up to 10^{19}cm^{-3} at RT. This is at odds with the scenario predicted by Mott, in which the photoexcitation above n_M causes an abrupt transition from an insulating phase to a metallic one.

3.7 Semiconductor Bloch Equations

To accurately explore the fate of exciton correlations above the nominal Mott density, we use the Semiconductor Bloch Equations (SBE) [143–145] and calculate the absorption spectrum of $MAPbBr_3$ in the presence of a photoexcited carrier density. The SBE describe the two-particle optical response based on single-particle properties such as the band structure, e-h occupancies and dipole matrix elements, as well as Coulomb-interaction-induced bound states. In addition, many-body effects that shape the optical response in the high-excitation regime can be systematically included consistent with the theory of ionization equilibrium of Section 3.3.2. Since excitons can be viewed as neutral composite particles, they do not induce significant renormalization or screening effects. Thus, we only consider the influence of unbound carriers on the absorption spectrum. A detailed explanation of the SBE calculations can be found in Appendix A.2.

The solution of the SBE under these assumptions results in the theoretical absorption spectra plotted in Figure 3.11(b) for different photoexcited carrier densities ($1\times10^{17} - 3.2\times10^{18}$ cm^{-3}). Here, the curves corresponding to the lowest densities are taken as a reference for the absorption coefficient at $n = 0$, since many-body effects do not produce sizeable changes in the optical spectra up to $n \sim 3.2\times10^{17}$ (see also the imaginary part of the dielectric susceptibility, $\mathrm{Im}\{\chi\}$, in Figure 3.12). We observe that the computed spectra show the persistence of the

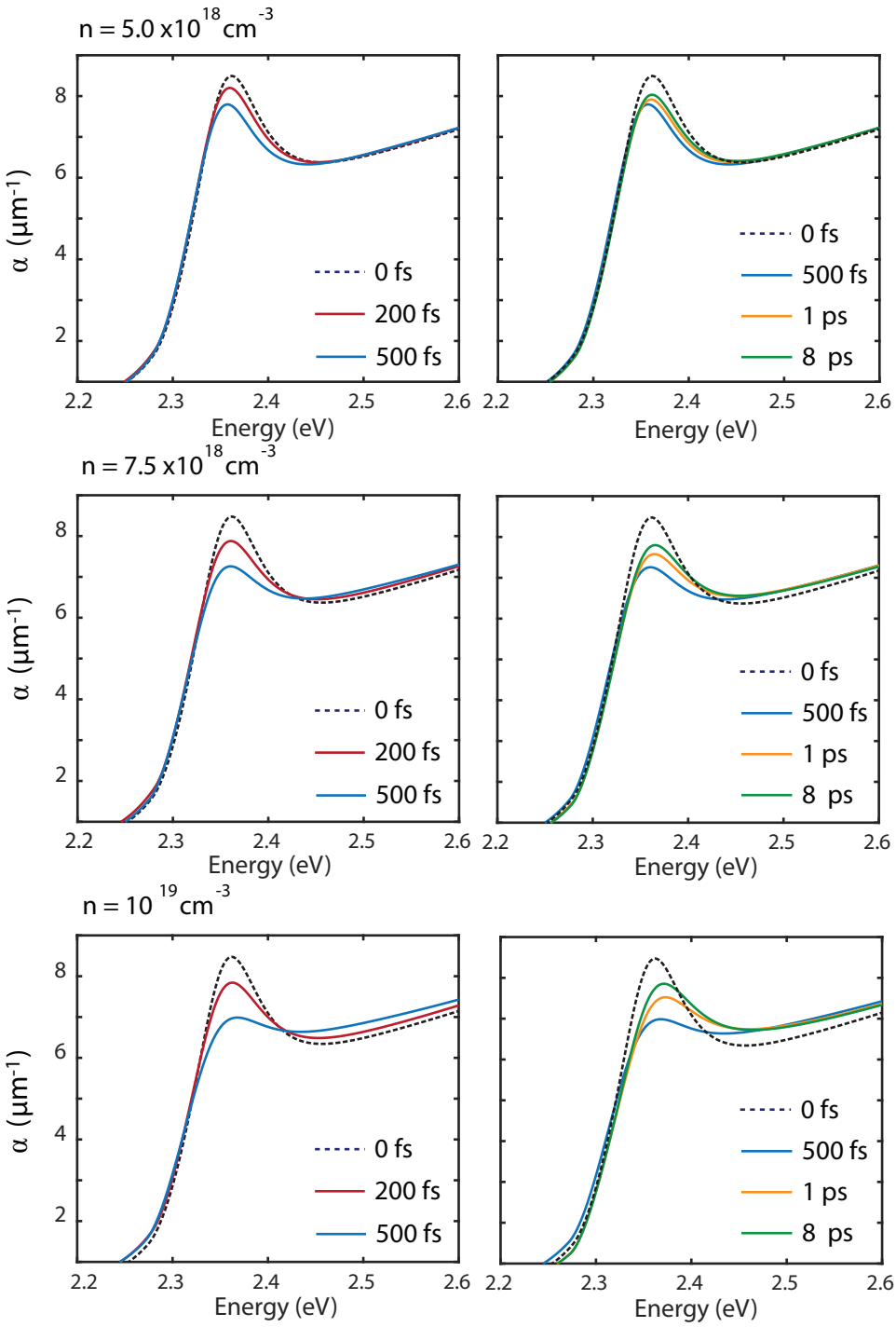

Figure 3.10 – Spectral evolution of $\alpha(\omega, t)$ calculated from the time-resolved TL model in the time windows 0-500 fs and 500 fs-8 ps.

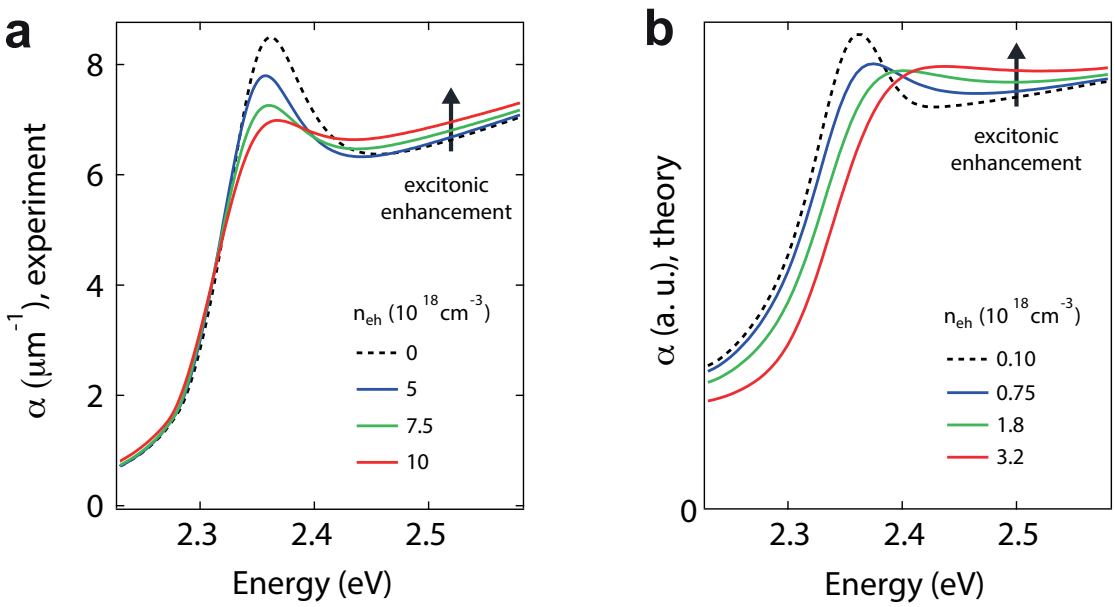

Figure 3.11 – (a) Absolute absorption spectrum of $MAPbBr_3$ single crystals for the excitation densities of 5, 7.5 and $10 \times 10^{18} cm^{-3}$ at 500 fs, corresponding to the time delay of maximum photoinduced bleaching. (b) Absorption spectra of of $MAPbBr_3$ in presence of increasing carrier densities as calculated with the SBE. The black arrow indicates the excitonic enhancement of the above-gap absorption associated to the presence of e-h correlations in the highly photoexcited material.

excitonic feature above n_M ($\sim 8 \times 10^{17}$ cm^{-3}) and the enhancement of above-gap absorption for increasing densities (black arrow), in excellent qualitative agreement with our experimental data.

On the other hand, the theory predicts a sizeable shift of the absorption edge, and the quantitative agreement in the explored excitation densities between the two sets of data is limited. The mismatch can be explained by considering the assumptions at the basis of our calculations. First, we describe the phonon-induced broadening as Lorentzian, which generates very long tails and over-broadens the excitonic feature at the band edge; the same effect can be invoked to explain the different vertical offset of the two sets of absorption spectra, also visible in $\mathrm{Im}\{\chi\}$ (Figure 3.12). Second, since the GW self-energy tends to overestimate renormalization effects, our prediction of the critical density might be slightly smaller. The description of CS can be improved by introducing a vertex correction to the self energy; however, such correction is computationally challenging. For our scope, correcting for the mismatch would only result in a small variation of n_M, which is not expected to overcome the experimental e-h densities nor influence significantly the discussion.

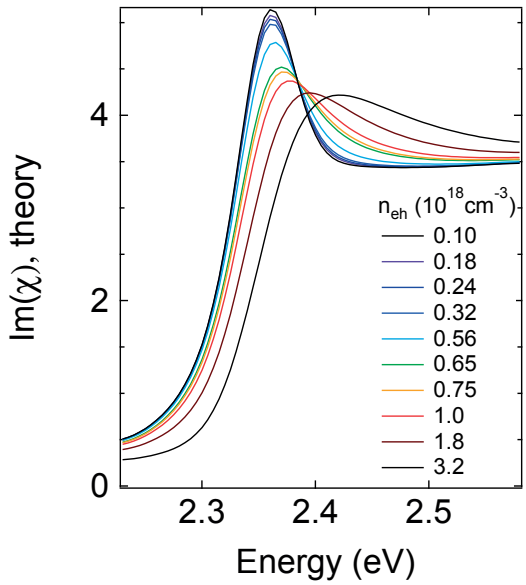

Figure 3.12 – Theoretical Im $\{\chi\}$ spectra calculated via the semiconductor Bloch equations for a range of e-h densities ($1 \times 10^{17} - 3.2 \times 10^{18}\text{cm}^{-3}$, see Appendix A.2).

3.8 Discussion

The qualitative behaviour observed in Figure 3.11 is in contrast with the disappearance of the bound state expected at the Mott transition, which would result in optical properties resembling the ones of non-interacting e-h pairs. A possible interpretation for the persistence of the exciton peak is that in highly excited $MAPbBr_3$ a crossover between the insulating and conductive phase occurs rather than a phase transition. Under these conditions, e-h pairs still form exciton-like states, the so-called Mahan excitons [6, 133, 134, 146]. The formation of Mahan exciton is accompained by the increase in above-gap absorption, which is referred to as Fermi-edge singularity, or excitonic enhancement. The origin of the enhanced absorption is explained by considering the distribution of e-h populations upon photoexcitation. In the presence of a degenerate e-h plasma, the bands are occupied up to the quasi-Fermi level. At the Fermi edge, the electrons and holes can still be attracted by Coulomb interaction, resulting in the appearance of above-gap absorption [6, 133]. Therefore, we assign the trend observed in Figure 3.11 to the excitonic enhancement arising from the strong correlations between e-h in the Fermi sea, persisting above n_M, which also prevents the exciton peak from disappearing.

The evolution of Wannier-Mott excitons into Mahan excitons has been recently investigated for degenerate wide-gap oxides [134], and the excitonic enhancement above the Mott transition has been reported experimentally for various semiconductors [132, 133, 146, 147]. In the low temperature limit, because of the sharpness of the Fermi surface, Mahan states are expected to appear as a singularity in the absorption spectrum in correspondence of the Fermi edge. Nevertheless, in real semiconductors at RT, the edge anomalies are broadened by temperature

effects and by the finite lifetime of photogenerated e-h pairs. Such a broadening typically prevents these states from being resolved as distinct peaks in experiments, and thus hinders a clear distinction between the formation of Mahan excitons and the Mott transition [134]. Conversely, in $MAPbBr_3$, we report the simultaneous presence of the excitonic enhancement and the exciton peak, which persists against increasing excitation densities. This indicates the unique character of the fundamental photo-excitations in this material, which retain a strongly-bound nature even at densities where free e-h pairs are expected to form.

In hybrid perovskites of the $MAPbI_3$ class, the presence of strong e-h correlations was suggested by early studies: here, the existence of bound states with small E_b has the advantage of enhancing the absorption onset without excitons being actually formed in the material [63]. The disappearance of the bound exciton peak in the same compound was also reported by optical pump-THz probe studies, and assigned to the dynamic screening of the exciton population, occurring on a sub-picosecond time scale [136]. In the case of $MAPbBr_3$, the exciton states are characterized by $E_b = 71$ meV; such a large E_b is key to preventing the full ionization of the exciton gas and causes the appearance of the spectral signatures due to Mahan excitons at higher energies. These results further remark the diversity in the fundamental excitations of the bromide and iodide compounds, the latter being characterized by an unstable exciton population which is easily screened in favour of the formation of free charge carriers.

3.9 Conclusion

In this Chapter, we presented a combined experimental-theoretical study to investigate the excited-state properties of $MAPbBr_3$ single crystals above the Mott density. In the experiment, we resolved the bound e-h resonance and excitonic enhancement up to e-h densities of $\sim 10^{19}\text{cm}^{-3}$, which is also reproduced by the theoretical absorption spectra at different excitation densities. Being the photoexcited e-h densities well above the estimated Mott density, we attribute the enhancement to the formation of exciton-like states, referred to as Mahan excitons. Our results support the scenario of strong e-h correlations in the hybrid perovskite at RT, and prove the exceptional stability of bound species in $MAPbBr_3$ single crystals against strong photoexcitation. These findings highlight the potential of hybrid perovskites in RT devices which demand high injected carrier densities, and open the door to the use of these materials in the field of excitonics.

4 Exciton dynamics in anatase TiO_2 single crystals

In this Chapter, we study the effect of above-gap photoexcitation on the excitonic states in anatase TiO_2 single crystals. We use ultrafast broadband deep-UV spectroscopy to investigate the interplay between bound excitons and a high density of e-h pairs in pristine and *n*-doped anatase TiO_2 single crystals. By tuning the excitation density above the previously explored range, we observe a pronounced bleaching and broadening of the excitonic transition, along with a sizeable blue shift of its peak energy. Our analysis suggest that the peculiar electronic structure of anatase TiO_2 cause the photoexcited electron-hole plasma to reduce the exciton binding energy via long-range Coulomb screening, while preventing the complete disappearance of the exciton lineshape. These results reveal unprecedented details on the excitonic dynamics in presence of high photoexcitation densities in this prototypical oxide.

4.1 Introduction

The photocatalytic reaction in TiO_2 is based on the absorption of deep-UV photons exceeding the fundamental optical band gap of 3.20 eV, which leads to the creation of neutral charge excitations in the material. Thereafter, the photogenerated charges are assumed to migrate to the surface of the TiO_2 substrate, and are transferred to the adsorbed species to initiate chemical reactions [86]. Understanding the hierarchy of phenomena that lie at the heart of the photocatalytic activity in anatase TiO_2 is a topic of great interest, as it paves the way to the design of more efficient photocatalytic systems. However, up to date, a number of important questions remains open in the field: How do the these processes depend on the nature of the charge excitations in the material? Do the charges directly react with adsorbates, or are they first trapped by surface species and then transferred to the reactants? Does charge trapping slow down or does it facilitate recombination?

To address these questions, in the last decade first significant steps have been made by the application of time-resolved spectroscopies to the case of anatase TiO_2, as addressed earlier in Chapter 1. Although these studies shed light on the e-h recombination pathways in anatase TiO_2, they did not relate the observed dynamics to the details of the electronic structure. As a

result, due to the simultaneous contribution of free electrons and holes in the system, transient absorption spectra from the THz to the visible show a high degree of ambiguity, hindering a clear distinction between the carriers and complicating the study of many-body phenomena. More remarkably, most studies focused on the interplay between free and trapped charges, due to the absence of clear spectroscopic signatures that could suggest the emergence of other quasiparticles at RT. Nevertheless, in view of the recent discovery of strongly bound exciton in the material [87], the question whether these excitons enhance or reduce the efficiency of photocatalytical reactions at the surfaces of anatase TiO_2 substrates is yet to be addressed.

To this aim, a first step would be to refine the established description of the charge dynamics by taking into account the presence excitonic correlations in this material. In the following, we investigate the interplay between excitons and uncorrelated e-h pairs in pristine and n-doped anatase TiO_2 single crystals by means of ultrafast broadband deep-UV spectroscopy. We observe that photoexciting the crystals with a high density of e-h pairs results in a pronounced bleaching and broadening of the excitonic transition, along with a sizeable blue shift of its peak energy. Our lineshape analysis suggests that the exciton binding energy (E_b) is reduced in the presence of a dense electron-hole plasma (EHP) via long-range Coulomb screening (CS). Moreover, the recovery of the exciton oscillator strength is found to proceed faster in the presence of oxygen vacancies, which suggests the active role of these defects in the recombination dynamics of the material.

4.2 Equilibrium optical spectra

For our study, we employ high-quality anatase TiO_2 single crystal grown by a chemical vapor-transport method (see Section 2.2.2). In particular, we focus on a pristine (transparent) and n-doped (black) single crystals exposing large (001) facets. The doping levels were determined to be $n \sim 0$ cm^{-3} and $n = 2 \times 10^{19}$cm^{-3}, respectively. We first characterize the static optical response of the samples. Figure 4.1 shows the real (ϵ_1) and imaginary (ϵ_2) parts of the dielectric function of the single crystals at RT with light polarized parallel to the a-axis. The material static reflectivity and absorption, as derived from ϵ_1 and ϵ_2, are instead shown in Figures 4.2 and 4.3.

In the pristine crystal, we observe that ϵ_2 is characterized by the presence of a sharp peak (I) at 3.79 eV, preceded by a long Urbach tail at lower energies [103]. A second, broader charge excitation (II) lies at 4.57 eV and extends up to 5.00 eV. We identify the two peaks as the spectral signature of strongly bound 2D excitons and a delocalized resonant excitation, respectively (see Section 1.5). All excitations are still clear-cut in the n-doped sample, where we observe: i) no apparent shift in the peak energy of features (I) and an slight red shift in the peak energy of feature (II); ii) a reduction of the oscillator strength of all peaks, due to a transfer of spectral weight from the above-gap to the below-gap region; iii) a pronounced broadening of the spectral features.

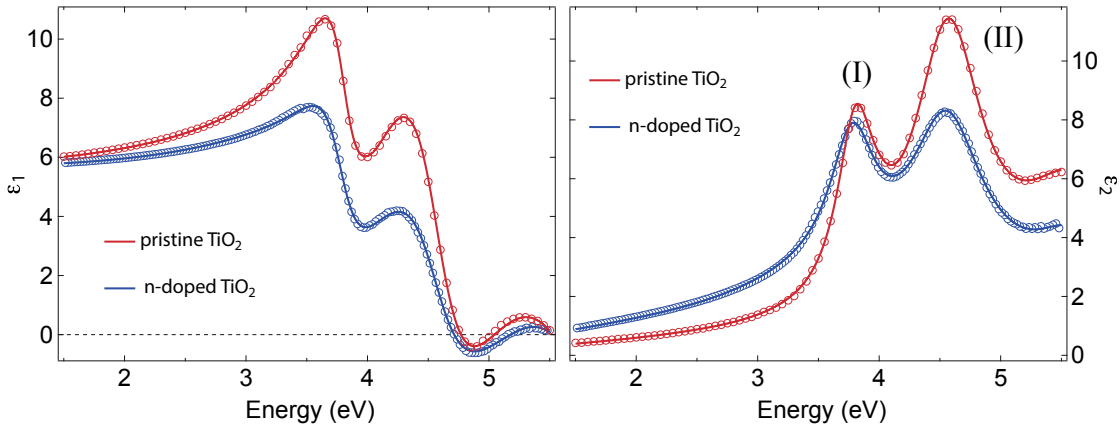

Figure 4.1 – Real (ϵ_1) and imaginary (ϵ_2) parts of the dielectric function of pristine (red curve) and n-doped (blue curve) anatase TiO_2 single crystals measured by spectroscopic ellipsometry. The solid lines are the results of the fit with Lorentz oscillators. Peaks (I) and (II) in (b) represent the signature of strongly bound 2D excitons and a delocalized resonant excitation, respectively.

4.3 Ultrafast broadband spectroscopy

To investigate the response of the excitonic transition to photoexcitation, we perform time-resolved reflectivity measurements using the set-up described in Section 2.1.2. We illuminate the TiO_2 crystal with an ultrashort pump pulse centered around 4.08 eV (violet arrow in Figure 4.3). This photon energy lies above the first exciton peak, and thus promotes a non-resonant excitation of uncorrelated e-h pairs [18]. Subsequently, we monitor the relative changes in the material reflectivity ($\Delta R/R$) over a broad spectral range covering the bound exciton feature (shaded area in Figure 4.3). The time-resolution of the experiments is ~700 fs and the dynamics is measured up to 1 ns. Figure 4.4(a) displays the colour-coded map of $\Delta R/R$ as a function of the probe photon energy and time delay between pump and probe. Similar trends are observed for the undoped sample, shown in Figure 4.4(b), although the signal amplitude is approximately four times smaller.

In both experiments, the photoexcited carrier density is set to $\sim 5 \times 10^{21}\,\mathrm{cm}^{-3}$ to exceed the fluence range ($8.0 \times 10^{19}\,\mathrm{cm}^{-3}$ to $8.4 \times 10^{20}\,\mathrm{cm}^{-3}$) that we explored in previous experiments on highly-excited anatase TiO_2 nanoparticles (NPs) [18]. In the map of Figure 4.4, we observe a derivative-like $\Delta R/R$ signal, which is positive above (red in the map) and negative (blue in the map) below 3.95 eV. First significant insights into the ultrafast dynamics are provided by the $\Delta R/R$ temporal traces, which are displayed in Figure 4.5(a) for the n-doped sample at representative probe photon energies. We observe that the signal undergoes a sign change over time close to 3.93 eV, which reflects a change in the zero-crossing energy over time. In the following, we present the results for the n-doped material. Similar analysis is implemented for the pristine crystal, whose results are summarized in Section 4.5.

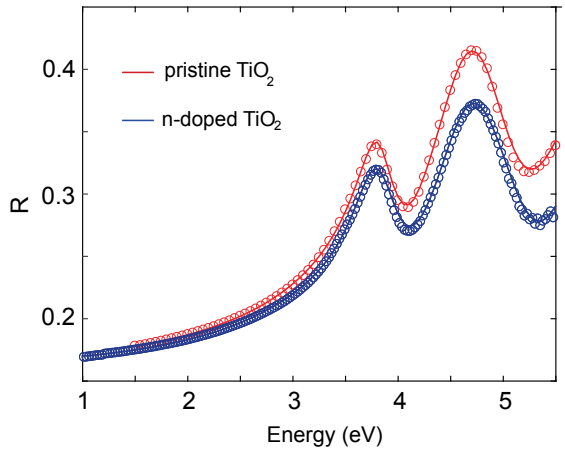

Figure 4.2 – Reflectivity of pristine (red curve) and n-doped (blue curve) anatase TiO_2 single crystals, calculated from the ellipsometry data (dots) overlapped with the fit obtained via Lorentz model (solid line).

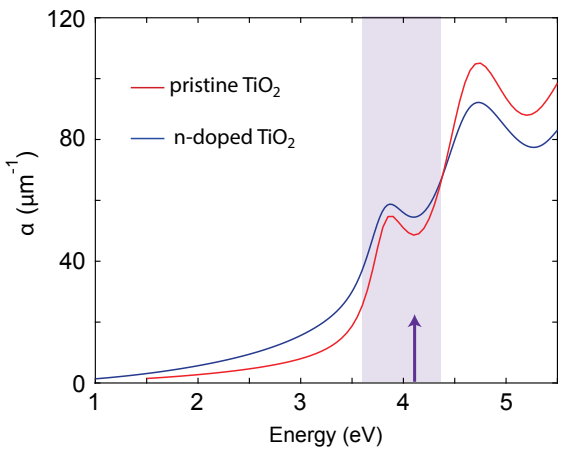

Figure 4.3 – Absorption spectrum of pristine (red curve) and n-doped (blue curve) anatase TiO_2 single crystals as calculated from the ellipsometry data.

4.4 Global fit analysis

To gain information on the timescales governing the evolution of the spectral features, as a first step we perform a global fit of the kinetic traces corresponding to 10 different probe photon energies. The traces are fitted with multi-exponential functions of the type:

$$\Delta R/R = OS + \sum_{i=1}^{4} A_i \mathrm{erfexp}(\sigma, D_i, \tau_i, t) \tag{4.1}$$

where the erfexp function denotes the convolution between an exponential function with decay constant (multiplied by a Heaviside function to account for signal causality) and a Gaussian with full-width at half maximum (FWHM) σ which accounts for the rising of the

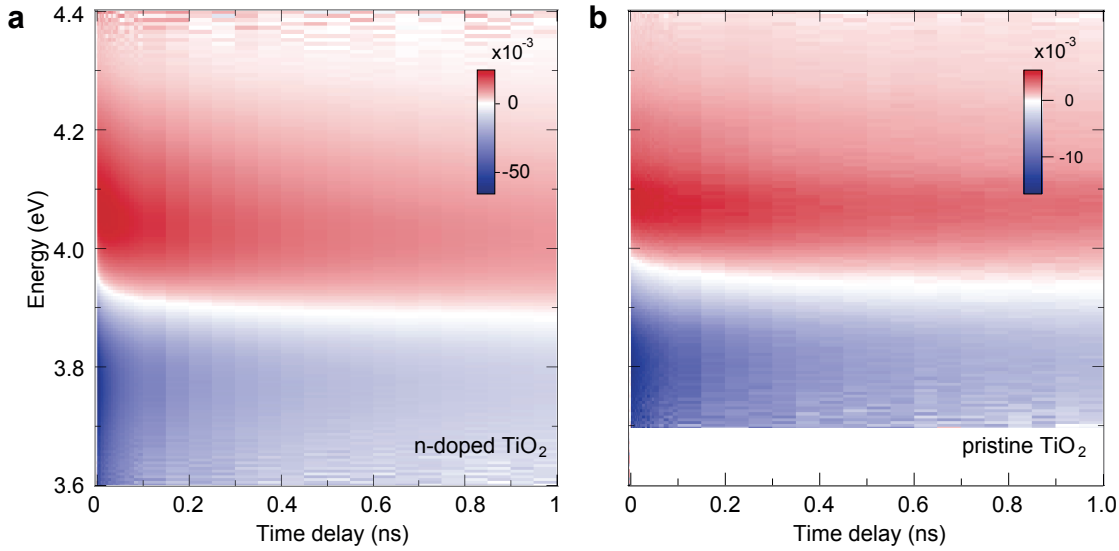

Figure 4.4 – Colour-coded $\Delta R/R$ map as a function of probe photon energy and time delay between pump and probe for (a) pristine and (b) n-doped TiO_2 crystals. The pump photon energy is 4.07 eV and the estimated carrier density is $n \sim 5 \times 10^{21}\,\mathrm{cm}^{-3}$. The time resolution is ~700 fs.

exponential. OS is the offset; A is the amplitude of the exponential; D the delay with respect to zero time delay. We assume that all the kinetic traces are described by the same rising and decay times, whereas we leave the A_i and D_i unlinked during the fit. The FWHM is set to 700 fs to account for the instrument response function.

The fit yields $\tau_1 \sim 415$ fs, $\tau_2 = 16$ ps, $\tau_3 = 120$ ps and $\tau_4 = 1.5$ ns for the n-doped crystal. The fitted curves are shown on top of the experimental traces as solid lines in Figure 4.5(a), whereas the decay associated spectra are shown in Figure 4.5(b). The contribution to the signal is negative for the fastest decay constants, while it retains a derivative-like shape (negative at lower energies, positive at higher energies) for the longest time constants, revealing the presence of at least two distinct processes which build up the material's transient response.

4.5 Lineshape analysis

A closer inspection of the $\Delta R/R$ data of Figure 4.4 reveals a complex spectral evolution taking place in the time window of our experiment. In this respect, more insightful information is provided by the analysis of the transient spectra at representative time delays. Figure 4.6(a) shows the spectra during the decay of the response ($t > 700$ fs), where we observe an asymmetric evolution around the inversion point, accompanied by a sizeable red shift of both the zero-crossing energy and the positive shoulder maximum. The presence of such renormalization calls for a different approach to the data analysis, since the assumptions of the global fit analysis of the kinetic traces might not hold for the reasons detailed in Section 3.6. Moreover,

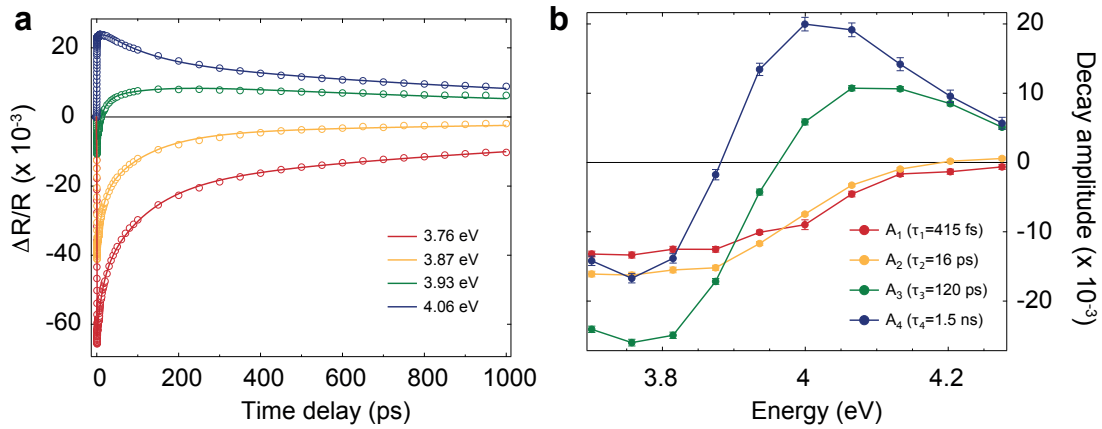

Figure 4.5 – (a) $\Delta R/R$ temporal traces extracted from the transient reflectivity data of Figure 4.4(a) (n-doped sample) at different photon energies (circles), and their corresponding fit (solid lines). (b) Decay spectra associated to the exponential time constants ($\tau_1 \sim 415$ fs, $\tau_2 = 16$ ps, $\tau_3 = 120$ ps and $\tau_4 = 1.5$ ns) resulting from the global fit of the traces in panel (a).

Table 4.1 – Amplitude, linewidth and peak energy of the five Lorentz oscillators modelling the dielectric function of n-doped anatase TiO_2 single crystals ($\epsilon_\infty = 0.189$)

Oscillator	**A**	**Γ**	**E_0**
L1	7.483 ± 0.324	0.45495 ± 0.009	3.785 ± 0.001
L2	6.191 ± 1.358	1.759 ± 0.120	3.669 ± 0.120
L3	18.9045 ± 0.670	0.734952 ± 0.670	4.568 ± 0.870
L4	6.495 ± 1.653	0.714 ± 1.653	5.578 ± 0.018
L5 (background)	~683	~ 31	~14.229

in our previous investigations on anatase TiO_2 nanoparticles, the transient absorption (ΔA) signal was monitored in transmission [18, 88, 89]. However, while ΔA is directly proportional to ϵ_2, $\Delta R/R$ has a complex relationship with both ϵ_1 and ϵ_2. For this reasons, being equally sensitive to both components of the dielectric function, the optical reflectivity signal can be used to decode additional information on any optical quantity of interest.

To rationalize the spectral dynamics, we derive the pump-induced evolution of the absorption from the measured $\Delta R/R$. The detailed procedure has been described in Section 3.6 in the case of $MAPbBr_3$ crystals. Briefly, we first model the steady-state optical data of Figure 4.1 using a Lorentz model comprising 5 oscillators. The resulting oscillator parameters are summarized in Table 4.1, where as the fitting curves are shown in Figure 4.1 as solid lines superimposed on the experimental data, demonstrating the accuracy of our fit. In addition, we calculate the steady-state reflectivity (solid lines in Figure 4.2), finding an excellent match with the experimental data (dots).

Thereafter, we calculate the time-dependent evolution of $R(\omega)$, displayed in Figure 4.6(b) for

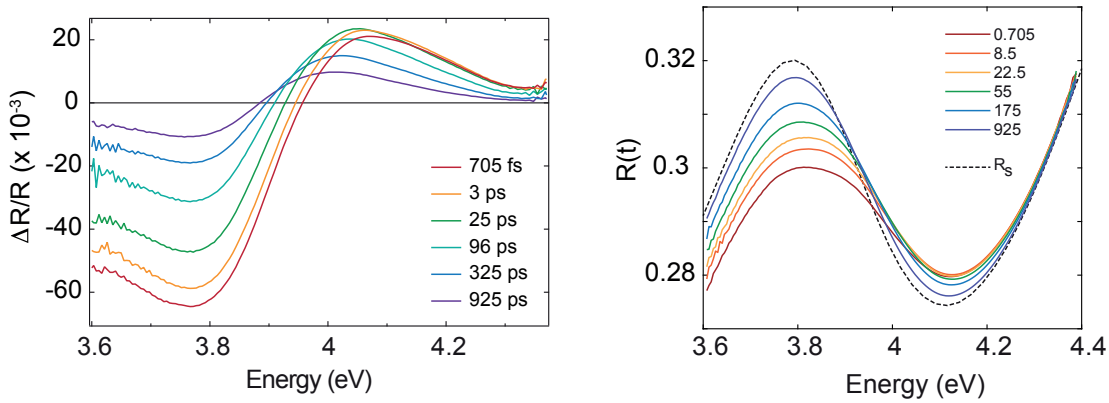

Figure 4.6 – (a) $\Delta R/R$ transient spectra extracted from the map in Figure 4.4(a) (n-doped sample) in the temporal windows 700 fs-1 ns. (b) Spectral evolution of $R(\omega, t)$, obtained by combining the steady-state $R_s(\omega)$ calculated from ellipsometry and the $\Delta R/R(\omega, t)$ data in the time windows 700 fs-1 ns.

the n-doped crystal, in which we observe a dramatic decrease of the first exciton oscillator strength, accompanied by a sizeable broadening of its linewidth and a small blue shift of its peak. We remark that this renormalization occurs within our instrument respose time (~700 fs); at longer time delays, the exciton red-shifts back to the steady-state position in approximately 1 ns (Figure 4.6(b)).

To track the exciton renormalization dynamics, we use the same Lorentz model function to fit the spectra of Figure 4.6(b) and relate the spectral changes to the variation of a subset of parameters characterizing the optical response. This way, we avoid the systematic errors produced by a Kramers-Kronig analysis. The fitted spectra and the evolution of the model parameters for the n-doped crystal are displayed in Figures 4.7 and 4.8 respectively.

We find that, at the present photoexcited carrier density, the exciton oscillator strength promptly decreases by 4% (Figure 4.8(a)), recovers with a bi-exponential trend, and stabilizes around its initial value for longer timescales. In contrast, a different temporal behaviour is followed by the peak energy and the exciton linewidth, which respectively shifts to the blue by 40 meV (Figure 4.8(b)) and broadens by 15% (Figure 4.8(c)) prior to decaying with a timescale of ~200 ps. A direct inspection of the absolute absorption as a function of time (Figure 4.9) shows that the exciton feature is strongly suppressed, and is about to merge into the continuum of direct charge excitations.

The same analysis is performed for the pristine crystal. Figure 4.10(a) reports the $\Delta R/R$ transient spectra, whereas the temporal evolution of $R(\omega, t)$ is shown in Figure 4.10(b). The evolution of the exciton oscillator strength, peak energy, and linewidth with respect to the equilibrium parameters is reported in Figure 4.11. In the case of the pristine material, we detect only a ~1% change in oscillator strength (Figure 4.11(a)), a ~2 meV shift of E_x (Figure 4.11(b)), and a linewidth broadening of ~15% (Figure 4.11(c)).

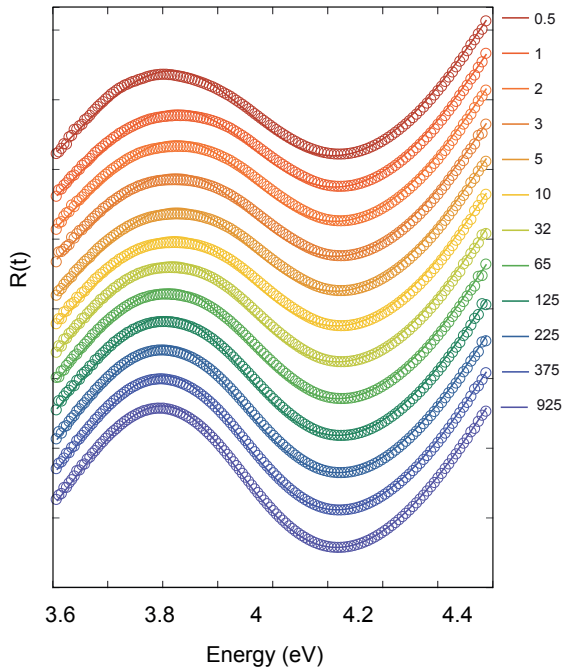

Figure 4.7 – Results of the Lorentz fit of $R(\omega, t)$ for the n-doped sample. Dots represent the experimental $R_s(\omega)$ curves, while the fits are shown in solid lines. The labels indicate the time delay in ps.

4.6 Discussion

We now rationalize the observed exciton dynamics and relate it to the many-body effects that modify the exciton lineshape in presence of a dense photoexcited density. In particular, the decrease in the oscillator strength can be associated with a phase-space filling (PSF) of the single-particle states contributing to the exciton. Moreover, the increased broadening of the exciton linewidth is an unambiguous manifestation that long-range CS is also at play, as the total (delocalized and trapped) photoexcited carrier density is expected to reduce the exciton lifetime. The origin of the exciton blue shift over time deserves instead separate attention. As presented in details in Chapter 1, three are the main optical nonlinearities that cause a shift in the excitonic features for above-gap photoexcitation in semiconductors, namely bandgap renormalization (BGR), long-range CS and PSF. While BGR leads to a density-dependent shrinkage of the single-particle states (and consequently a red shift of the exciton feature), long-range CS screens the electron-hole interaction and reduces the exciton binding energy, thus shifting the exciton to the blue. PSF can also contribute a blue shift of the exciton peak through the Burnstein-Moss effect, as the absorption is pushed to higher energies when the bands get populated. These processes act simultaneously on the exciton lineshape, their relative weights being governed by the material parameters and dimensionality [118, 119]. In the case of anatase TiO_2, our previous transient absorption study on highly-excited NPs in aqueous solution detected no sizeable shift of the exciton peak up to a photoexcited carrier density of $8.4 \times 10^{20}\,\mathrm{cm}^{-3}$, thus revealing a remarkable stability of the excitonic states against

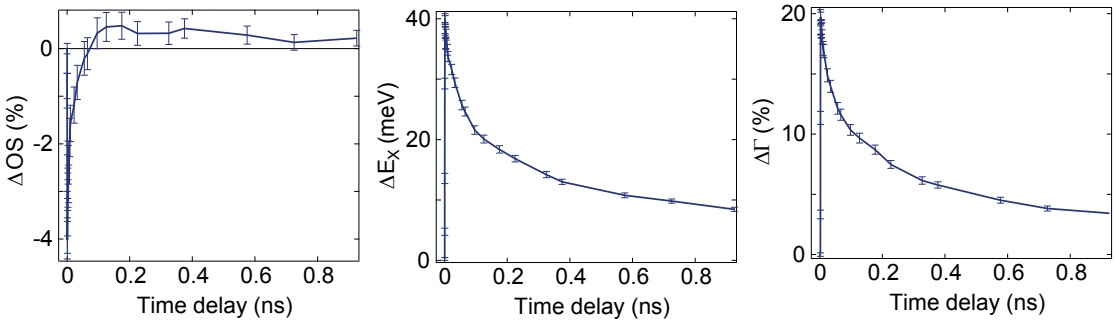

Figure 4.8 – Evolution of the oscillator strength (a), peak energy (b) and linewidth (c) of the first Lorentz oscillator with respect to the equilibrium parameters of n-doped TiO_2 single crystals as obtained by iterating Lorentz fit over the reflectivity for different time delays.

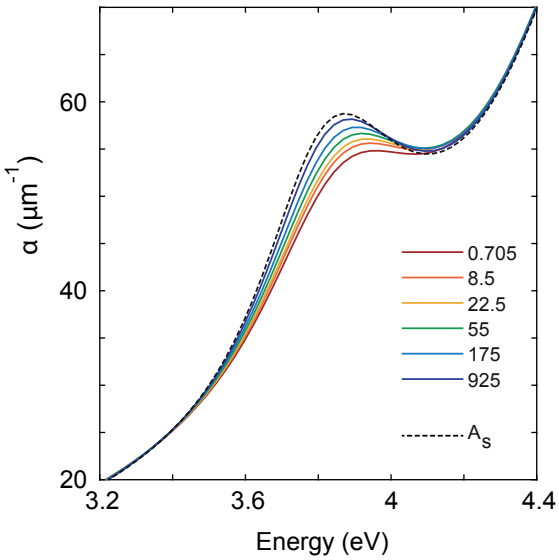

Figure 4.9 – Spectral evolution of $\alpha(\omega, t)$ for n-doped TiO_2 single crystals as calculated from the time-resolved Lorentz model.

the photoexcited electron-hole plasma [18, 88]. In contrast, under the present excitation conditions, in the n-doped sample the exciton is observed to blue shift following a temporal response that closely resembles the one of the linewidth (Figure 4.8(b,c)). This indicates that long-range CS is the dominant source of optical nonlinearity behind the exciton blue shift in anatase TiO_2 single crystals, ruling out an active role of PSF. Consistent with this scenario, previous angle-resolved photoemission spectroscopy measurements demonstrated the absence of BGR for carrier densities as high as $10^{21}\,cm^{-3}$; therefore, this effect is negligible at our excitation density. As a result, the detected blue shift can be directly correlated with the absolute change in the exciton E_b produced by the photoexcited e-h pairs. Our current time resolution limits the estimate of the E_b change to ~40 meV (lower limit) for the n-doped crystal; this value is expected to be even larger in experiments at higher time-resolution.

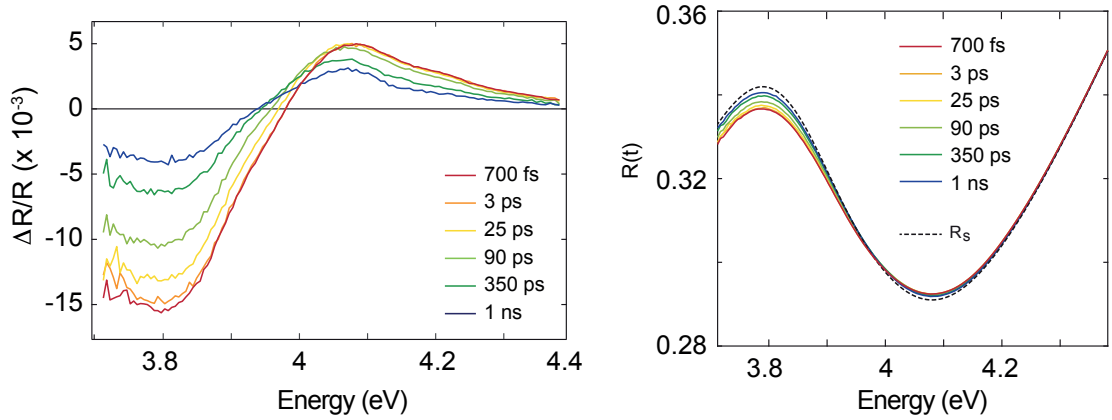

Figure 4.10 – (a) $\Delta R/R$ transient spectra extracted from the map in Figure 4.4(b) (pristine sample) in the temporal windows 700 fs-1 ns. (b) Spectral evolution of $R(\omega, t)$, obtained by combining the steady-state $R_s(\omega)$ calculated from ellipsometry and the $\Delta R/R(\omega, t)$ data in the time windows 700 fs-1 ns.

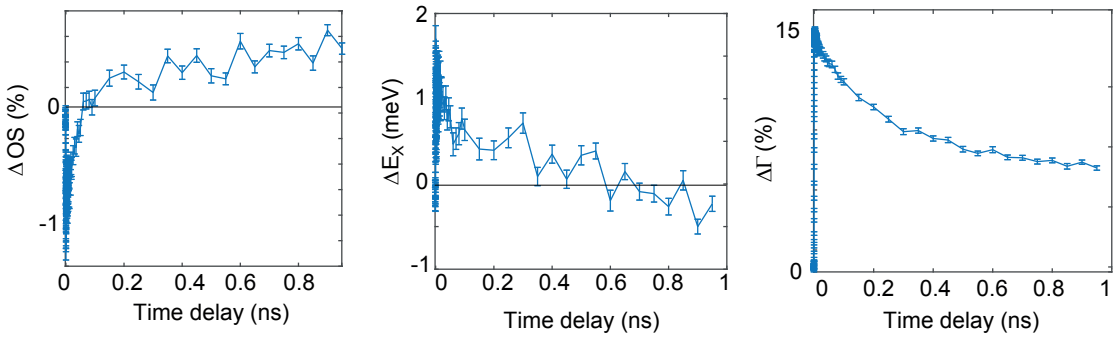

Figure 4.11 – Evolution of the oscillator strength (a), peak energy (b) and linewidth (c) of the first Lorentz oscillator with respect to the equilibrium parameters of pristine TiO_2 single crystals as obtained by iterating Lorentz fit over the reflectivity for different time delays.

Finally, we compare the results for the pristine and n-doped crystals. As observed previously, for identical excitation densities the $\Delta R/R$ signal in the n-doped sample is found to be approximately four times larger than the pristine sample; furthermore, the lineshape analysis reveals a much smaller variation in parameters in the pristine sample. However, the present fits are affected by a larger error, which limits us to a qualitative discussion. In this regard, we notice that the recovery of the exciton oscillator strength is found to proceed slightly faster in the presence of oxygen vacancies, which suggests the active role of these defects in the recombination dynamics of the material, [148]

4.7 Conclusion

In conclusion, this Chapter presented a study the effect of above-gap photoexcitation on the excitonic states in anatase TiO_2 single crystals. We observed a pronounced bleaching and

broadening of the excitonic transition, along with a sizeable blue shift of its peak energy in both pristine and n-doped samples. Our analysis suggest that the peculiar electronic structure of anatase TiO_2 cause the photoexcited electron-hole plasma to reduce E_b via long-range Coulomb screening while preventing the complete disappearance of the exciton lineshape. Therefore, above a carrier density of $n \sim 5 \times 10^{21}\text{cm}^{-3}$, the excitons can become unstable with respect to the formation of an electron-hole plasma. We found this effect to be more pronounced in the presence of oxygen vacancies; moreover, the decay of the nonequilibrium signal in this sample proceeds slightly faster than the other responses, and suggests that the increased density of in-gap states facilitates charge carrier recombination across the bandgap.

5 Exciton control with coherent strain pulses in anatase TiO_2

The coherent manipulation of excitons in bulk semiconductors via the lattice degrees of freedom is key to the development of acousto-optic and acousto-excitonic devices. In this Chapter, we perform state-of-the-art ultrafast broadband UV spectroscopy on anatase TiO_2 single crystals at RT, and reveal the modulation of the exciton peak amplitude due to coherent acoustic phonons launched by the UV pump pulse. This modulation is accompanied by a giant exciton shift of ~30 meV. We rationalize our results by advanced many-body perturbation theory calculations, which analyze the influence of the coherent acoustic field onto the excitonic correlations. This combined theoretical-experimental approach paves the way to the design of exciton control schemes with propagating strain pulses[1].

5.1 Introduction

New perspectives in the field of excitonics have recently developed from the discovery of strongly bound excitons that persist at RT in several semiconductors, including organics [149], transition metal dichalcogenides [150], and transition metal oxides [87, 151, 152]. Despite their different origin, excitons in these classes of materials are strongly coupled to the lattice degrees of freedom. Indeed, since excitons can be viewed as quanta of electronic excitation energy travelling in the periodic crystal lattice, their motion is influenced by the fluctuating potential field due to lattice vibrations. On the fundamental aspect, exciton-phonon coupling is an intriguing type of interaction that results in phenomena such as exciton self-trapping, spectral-weight transfers to phonon sidebands and Stokes-shifted emissions [153]. On the practical side, identifying the specific modes (optical or acoustic) that couple strongly to the excitons paves the way to the control of the exciton properties through the tailored application of strain, pressure or photoexcitation.

Experimentally, the microscopic details of the exciton in the phonon field can be addressed via absorption and photoluminescence spectroscopy, since the shape and width of the optical

[1] Edoardo Baldini, Adriel Dominguez, Tania Palmieri, Oliviero Cannelli, Angel Rubio, Pascal Ruello, Majed Chergui, *"Exciton Control in a Room-Temperature Bulk Semiconductor with Coherent Strain Pulses"*. Submitted.

spectra directly reflect the coupling of the exciton to the lattice vibrations [154]. However, the information offered by these methods is mediated over all the coupled phonon modes. This calls for more advanced techniques that can yield information on the exciton-phonon coupling for specific lattice modes of interest in order to allow, in return, for the phonon-selective control of the exciton properties. A powerful tool relies on setting a particular phonon mode out of equilibrium and monitoring the impact of the ionic motion on the exciton spectral features, which is possible by time- and energy-resolved optical spectroscopy [155–163]. Moreover, this approach also opens the door to the high-speed control of the exciton properties via ultrafast light excitation. So far, the coherent manipulation of excitons through the photoinduced ionic motion has led to exciton shifts as large as 10 meV in semiconductor nanostructures, and only at very low temperatures [164, 165]. At RT, shifts of <1 meV have only been reached in quantum dots [166], where the exciton-phonon coupling is enhanced by the low-dimensionality, posing serious limitations to the use of this approach for the design of efficient acousto-excitonic devices.

An alternative strategy involves the use of bulk semiconductors that are known to host strongly bound excitonic resonances at RT and simultaneously show strong electron-phonon coupling phenomena. An ideal material system is represented by anatase TiO_2, whose optical absorption spectrum is dominated by strongly bound excitons, as presented in Section 1.5. In TiO_2, there exists a moderately strong coupling between the electronic degrees of freedom that build up the exciton states and the polar optical modes of the lattice via the Fröhlich interaction [107, 167]. Yet, the study of the direct coupling between the excitonic states and the acoustic modes is still in its infancy. In a recent study, we demonstrated that UV femtosecond laser pulses can coherently excite acoustic phonons that are confined in anatase TiO_2 nanoparticles at RT, leading to a dramatic modulation in the amplitude of the material's a-axis exciton [89]. Although such an effect points towards a giant coupling between excitons and acoustic phonons in anatase TiO_2, its theoretical understanding was partially hindered by the averaging effect due to the random distribution of the nanoparticles, and the fact that the confined mechanical vibrations of these nanosized objects depend on the boundary conditions. Making use of a single crystal of anatase TiO_2 clearly provides a more direct and precise way of probing the acoustic phonon/exciton coupling matrix elements. Moreover, future acousto-optic and acousto-excitonic applications would benefit from the coherent control of excitons through the use of propagating strain pulses in bulk substrates, rather than confined modes in nanosized particles. As such, demonstrating extraordinary RT acoustic effects in the case of anatase TiO_2 single crystals is highly desirable.

In the following, using ultrafast broadband spectroscopy in the UV, we reveal the signature of coherent acoustic phonons that couple directly to the c-axis exciton of anatase TiO_2 single crystals. Thanks to the high photogenerated carrier densities that can be supported by this material, a giant modulation of the reflectivity amplitude is produced by the coherent phonons, and it indicates efficient generation/detection of the acoustic modes. Furthermore, the strong exciton-phonon coupling leads to a ~30-50 meV shift of the exciton peak, which is the largest ever reported in condensed matter systems under a time-dependent perturbation. We

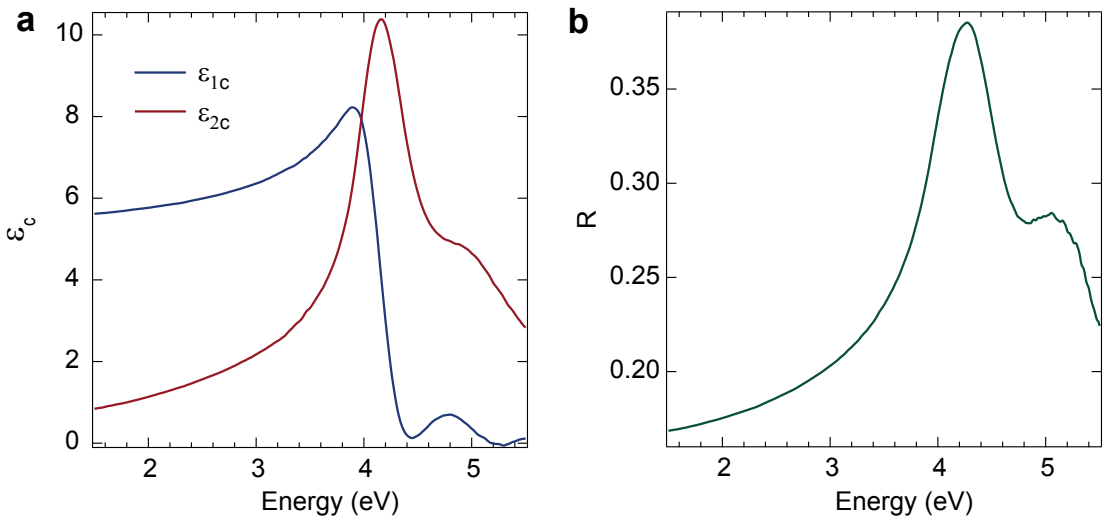

Figure 5.1 – (a) Real part (blue) and imaginary part (red) of the dielectric function and (b) reflectivity of ac-oriented anatase TiO_2 single crystals measured at RT with the electric field polarized along the c-axis.

rationalize our findings within the framework of many-body perturbation theory, providing a complete quantitative treatment of such a strong exciton-phonon interaction.

5.2 Equilibrium optical spectra

High-quality anatase TiO_2 single crystals were grown by a chemical vapor-transport method (see Section 2.2.2) and oriented via Laue diffraction to expose a (010) surface to the incoming radiation. Figure 5.1(a) shows the real part (ϵ_{1c}, blue) and imaginary part (ϵ_{2c}, red) of the dielectric function at RT with light polarized parallel to the c-axis. The material reflectivity as derived from the dielectric function is shown in Figure 5.1(b). The ϵ_{2c} trace features a sharp peak at 4.15 eV, which is due to the c-axis excitonic transition (see Section 1.5). A weaker charge excitation lies around 5.00 eV and is ascribed to a resonant interband transition within the continuum. Consistently, R presents similar features at 4.26 eV and 5.15 eV, respectively.

5.3 Ultrafast spectroscopy

In our time-resolved experiments, performed with the pump-probe set-up described in Section 2.1.2, we excite the crystal with an ultrashort laser pulse polarized along the c-axis. Its photon energy of 4.50 eV lies above the c-exciton peak, thus promoting a non-resonant excitation of uncorrelated electron-hole pairs. The photoexcited carrier density is set to $n \sim 3.5 \times 10^{20}\text{cm}^{-3}$. Subsequently, we monitor the relative changes in the material c-axis reflectivity ($\Delta R/R$) over a broad spectral range spanning the exciton feature (4-4.8 eV).

Figure 5.2(a) displays the colour-coded map of $\Delta R/R$ as a function of the probe photon energy

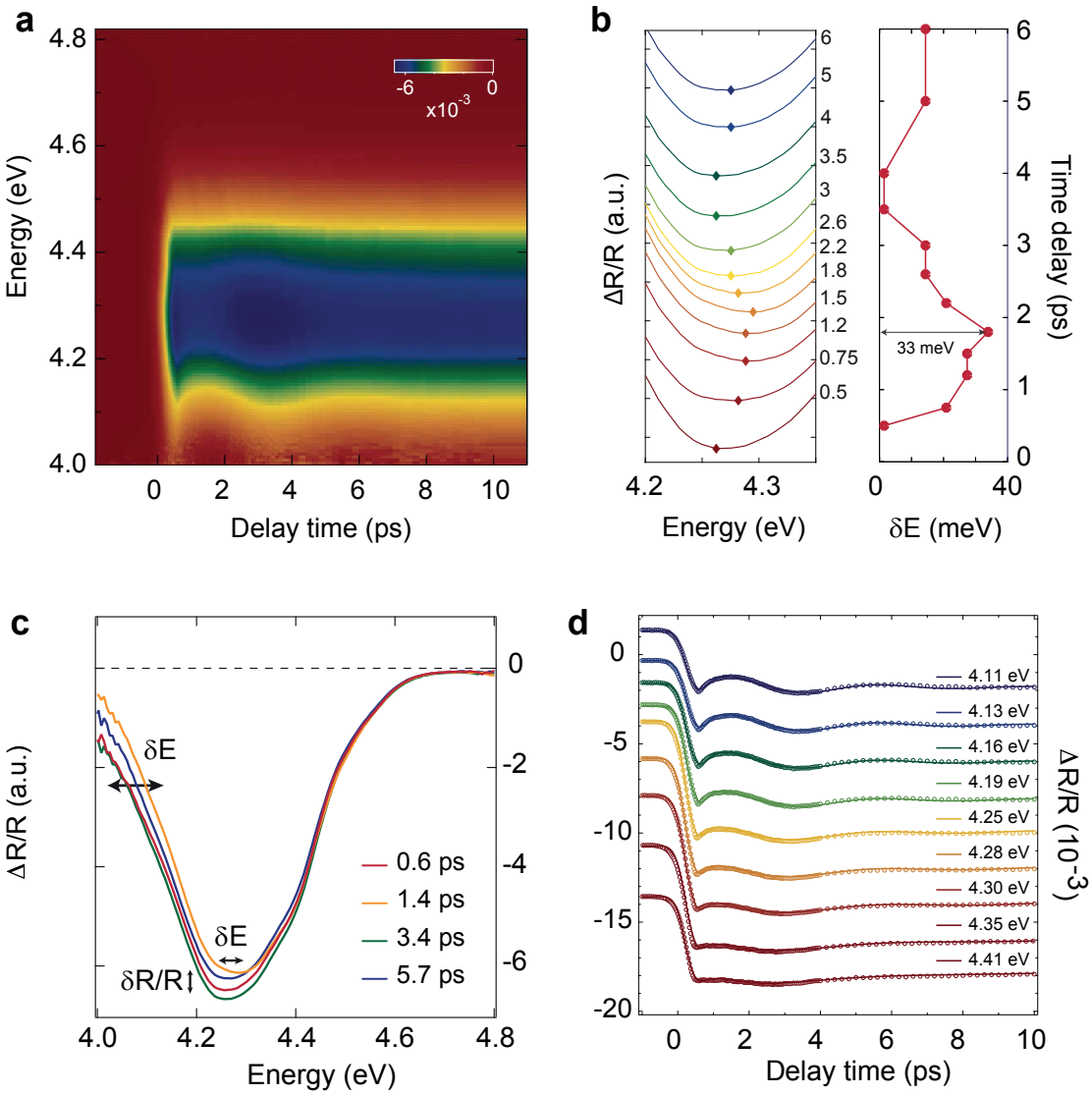

Figure 5.2 – Transient reflectivity measurements of anatase TiO_2 single crystals with the electric field polarized along the c-axis. (a) Colour-coded map of $\Delta R/R$ at RT as a function of probe photon energy and time delay between pump and probe. Both pump and probe beams are polarized along the material c-axis. The pump photon energy is 4.50 eV. (b) Transient spectra of $\Delta R/R$ for different time delays during the first 10 ps of the response, which track the shift of the exciton peak. (c) Transient spectra of $\Delta R/R$ for different time delays during the coherent acoustic phonon evolution. The exciton peak undergoes a δE = 30 meV variation in energy and a $\Delta R/R$ ~5% change in intensity. The low-energy tail of the exciton also reacts to the modulation, shifting by 50 meV. (d) Temporal traces of $\Delta R/R$ for different probe photon energies (dotted lines), indicated in the label. The solid lines are fits to the experimental data.

and time delay between pump and probe. We observe a long-lived negative $\Delta R/R$ response, which is primarily due to the contribution of phase-space filling (*i. e.* exciton bleaching in the corresponding transient absorption signal) induced by the photoexcited carrier density [87]. Importantly, this feature experiences a pronounced sinusoidal modulation during the first 6 ps, which is particularly evident around 4.10 eV. Selecting $\Delta R/R$ spectra at representative time delays during this sinusoidal modulation (Figure 5.2(b)) leads us to observe a giant variation of the exciton energy (δE as large as 30 meV at the exciton peak), and intensity ($\Delta R/R \sim 5\%$ of the total signal at the exciton peak). Also the low-energy tail of the exciton strongly reacts to the modulation, undergoing a 50 meV shift (Figure 5.2(c)). Complementary insights are offered by the temporal traces, which are shown in Figure 5.2(d) at representative photon energies. They feature a resolution-limited rise followed by a large-amplitude coherent response on top of the flat background caused by the phase-space filling. The modulation is strongly damped, vanishing after two periods. Its frequency is much lower than that of optical phonons in anatase TiO_2 [168, 169] and it varies with the probe photon energy.

5.4 Global fit analysis

To retrieve the photon energy dependence of the modulation frequency, we perform a standard global fit of the temporal traces up to 1 ns, by simultaneously fitting nine traces in the 4.10-4.42 eV range, while fixing the same time constants. The temporal traces comprise two main signals: i) the incoherent response caused by electron-hole generation and recombination; and ii) the strongly damped sinusoidal modulation caused by the propagation of coherent acoustic phonons. A satisfactory fit could be obtained by using two exponential functions (with relaxation time $\tau_1 = 42$ ps and $\tau_2 = 270$ ps, decay associated spectra in Figure 5.3(a)) and a damped sinusoidal term convolved with a Gaussian response accounting for the temporal shape of the pump pulse. The fitted curves are shown in Figure 5.2(c) as solid lines on top of the experimental traces. The dependence of the modulation amplitude (red trace) and frequency (blue trace) on the probe photon energy is plotted instead in Figure 5.3(b). We observe that the amplitude peaks around 4.15 eV, *i. e.* at the low-energy tail of the exciton resonance in the reflectance spectrum. Furthermore, the modulation frequency varies with the probe photon energy, which is not expected in the case of coherent optical phonons. This observable supports that the modulations are due to longitudinal acoustic phonons propagating along the [010] axis of the anatase TiO_2 single crystal.

Light-induced coherent acoustic phonons in solids have been a subject of numerous studies, especially with all-optical pump-probe methods in the transparency region of materials or in the proximity of interband transitions [156]. However, the study of the interplay between these propagating acoustic modes and excitonic collective states in bulk solids is still unexplored. This framework holds promise especially in the case of materials possessing a strong exciton-phonon coupling, as the coherent strain field can lead to dramatic effects on the exciton bound states. Consistent with this idea, we observe that the modulation depth of the exciton oscillator strength provided by the coherent acoustic phonons in bulk anatase TiO_2 is among

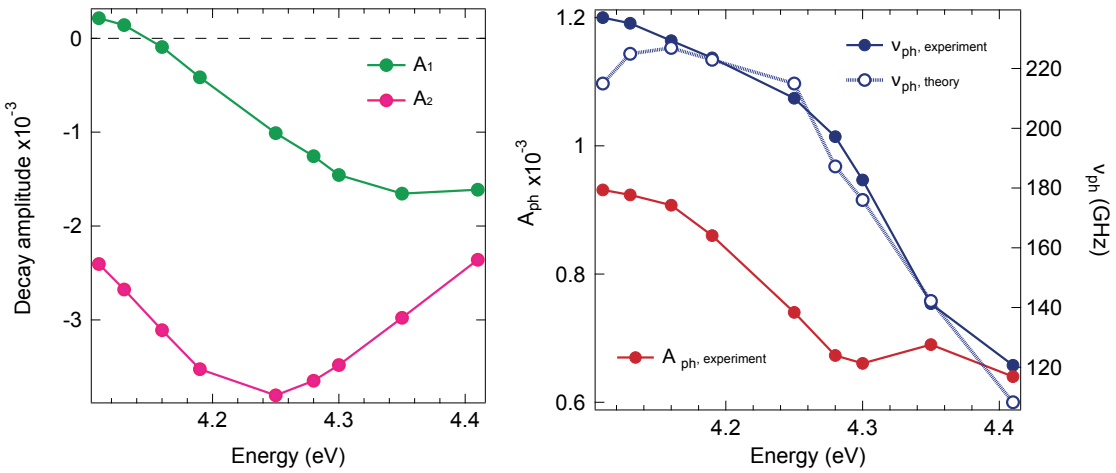

Figure 5.3 – Probe photon energy dependence of the amplitude of the exponential terms (A_1, A_2), and the amplitude (A_{ph}, red) and frequency of the coherent oscillations (ν_{ph}, blue) obtained from the global fit of the kinetic traces, with a comparison between experiment and theory.

Table 5.1 – Exciton shifts in different materials under distinct external perturbations (PSF=pulsed strain field, PLF=pulsed light field).

Material	Dimensionality	Perturbation	T	δE_X	Ref.
Anatase TiO_2	Bulk	PSF	295 K	30-50 meV	This work
$Zn_{1-x}Cd_xSe$	Quantum wells	PLF	10 K	4 meV	[172]
WS_2, WSe_2	Monolayer	PLF	295 K	10-18 meV	[173, 174]
$CH_3NH_3PbI_3$	Bulk	PLF	295 K	10 meV	[175]
GaAs/AlGaAs	Heterostructure	PSF	1.8 K	1 meV	[164]
ZnSe/ZnMgSSe	Quantum wells	PSF	1.8 K	10 meV	[165]
CdSe	Quantum dots	PSF	295 K	< 1 meV	[166]

the largest ever experimentally observed. Comparable signals have only been reported in semiconductor nanostructures [170, 171], where the electron-phonon coupling is strongly enhanced by quantum confinement. We also notice that the detected exciton shift is one of the highest ever reached in condensed matter systems at RT under the influence of a time-dependent perturbation, as summarized in Table 5.1. Therefore, our observations point towards a giant exciton-acoustic phonon coupling in RT bulk anatase TiO_2.

In the following, we provide a general description of the generation and detection mechanism of coherent acoustic photons (CAP) in TiO_2 and we reveal the details of exciton-phonon coupling in this material by means of many-body perturbation theory, thanks to the collaboration with Dr. Adriel Dominguez and Prof. Angel Rubio (Hamburg). Such an advanced *ab initio* treatment of the exciton-phonon coupling in bulk solids has never been explored before and

it shows that the deformation potential (DP) coupling lies at the origin of the observed effects in anatase TiO_2.

5.5 Generation and detection of coherent acoustic phonons

5.5.1 Generation mechanism

The generation of CAP is based on the conversion of the optical energy of the pump pulse into mechanical energy *via* the photoinduced stress, denoted as $\sigma(z,t)$ [156]. The equation of motion is based on a semiclassical theory: the equation of the elastic motion is based on the classical approach of wave physics, whereas $\sigma(z,t)$ is described within the quantum approach. For an isotropic medium, the wave equation reads

$$\frac{\partial^2 u}{\partial t^2} - C_a^2 \frac{\partial^2 u}{\partial z^2} = \frac{1}{\rho}\frac{\partial \sigma(z,t)}{\partial z} \tag{5.1}$$

where u, ρ are the displacement and mass density in the material and C_a the speed of sound velocity. The source term $\sigma(z,t)$ is composed by different contributions, which reflect different microscopic mechanisms involved in the generation of CAP, the most important being the deformation potential (DP), thermoelasticity (TE), and inverse piezoelectricity (PE). Because anatase TiO_2 is a non-magnetic and non-piezoelectric material, CAP generation can occur only via the influence of DP or TE mechanisms, which are described in the following.

Deformation potential

The DP mechanism is related to the modification in energy of the electronic distribution upon photon absorption, which perturbs the interatomic forces inside the material and induces a displacement of the ions from their equilibrium position. This change results in the deformation of the crystal and emission of acoustic phonons [156]. The electronic contribution to the photoinduced stress (σ_{DP}) can be expressed as:

$$\sigma_{DP} = \sum_k \delta N(k) \frac{\partial E_k}{\partial \eta}, \tag{5.2}$$

where $\delta N(k)$ is the change of the electronic concentration at level k and $\partial E_k/\partial\eta$ is the deformation potential parameter. This expression can be simplified by considering that in TiO_2 the photoexcited carriers have thermalized to the bottom of the respective bands at Γ and X in 50 fs [18], *i. e.* a much faster timescale than the detected coherent acoustic phonon period. Therefore, we can write

$$\sigma_{DP} = -NB\left[\left.\frac{\mathrm{d}E_e}{\mathrm{d}P}\right|_\Gamma + \left.\frac{\mathrm{d}E_h}{\mathrm{d}P}\right|_X\right] = -NB(d_e + d_h), \tag{5.3}$$

where N is the photoinduced carrier concentration, B is the bulk modulus, P the electronic pressure, and d_e and d_h the deformation potential coupling of electrons and holes respectively.

Thermoelasticity

The TE mechanism indicates the change in volume following a temperature variation, which can also be induced by an intense laser pulse [156]. From the microscopic point of view, the lattice heating originates from the energy transfer from the photoexcited carriers to the phonon modes. The TE contribution to the photoinduced stress (σ_{TE}) can be written as

$$\sigma_{TE} = -\alpha_V B \Delta T_L = -\alpha_V B N E_{exc} / C_L, \tag{5.4}$$

where α_V is the volumetric thermal expansion coefficient. For a tetragonal crystal, $\alpha_V = 2\alpha_\perp + \alpha_\parallel$, where $\alpha_\perp$ and $\alpha_\parallel$ are the in-plane and the out-of-plane thermal expansion coefficients, respectively. ΔT_L is the lattice temperature, C_L is the lattice heat capacity per unit volume and E_{exc} is the excess energy with respect to the optical bandgap energy.

Relative contribution

To assess whether the generation mechanism is governed by the electronic or phononic pressure, one can consider the ratio between the DP- and TE coupling contributions to the photoinduced stress, σ_{DP}/σ_{TE}, expressed by

$$\frac{\sigma_{DP}}{\sigma_{TE}} = \frac{C_L(d_e + d_h)}{\alpha_V E_{exc}} \tag{5.5}$$

If the ratio is $\ll 1$, the main contribution is the phononic pressure. In the opposite case, the deformation potential mechanism is the dominant one, as it is the case in many band insulators and semiconductors [156].

5.5.2 Detection mechanism

As a second step, we evaluate the efficiency of the DP coupling by providing a quantitative description of the coherent acoustic phonon transient reflectivity signal ($\Delta R/R$). In general, if the probe photon energy lies within the bandgap of an insulator, the detection mechanism can be interpreted in terms of the conventional Brillouin scattering process [176], in which only the real part of the material's refractive index is modulated and the phonon frequency linearly depends on the probe light wave vector k inside the material ($\nu_{ph} = kv/\pi$, where v is the sound velocity). In contrast, when the material is opaque to the probe photon energy, a more general expression has to be taken into account for the detection process, by including the contribution of imaginary parts of both the refractive index and the photoelastic coefficient. This is accounted for by the general perturbative approach developed by Thomsen et al. [177],

in which the strain-induced change in reflectivity reads

$$\frac{\delta R}{R} = 2\,\mathrm{Re}\left\{\frac{4ik_0\tilde{n}}{1-\tilde{n}^2}\frac{\mathrm{d}\tilde{n}}{\mathrm{d}\eta}\int_0^\infty \eta(z,t)e^{2ik_0\tilde{n}z}dz\right\}, \tag{5.6}$$

where Re denotes the real part, $z = 0$ defines the TiO_2 surface, k_0 is the probe light wave vector in vacuum and $\tilde{n} = n_1 + in_2$ is the complex refractive index. In this expression, the exciton-phonon coupling parameter is represented by the photoelastic coefficient $\mathrm{d}\tilde{n}/\mathrm{d}\eta$, which can be written as

$$\frac{\mathrm{d}\tilde{n}}{\mathrm{d}\eta} = \frac{\mathrm{d}n_1}{\mathrm{d}\eta} + i\frac{\mathrm{d}n_2}{\mathrm{d}\eta} = \frac{\mathrm{d}E}{\mathrm{d}\eta}\left(\frac{\mathrm{d}n_1}{\mathrm{d}E} + i\frac{\mathrm{d}n_2}{\mathrm{d}E}\right). \tag{5.7}$$

and is linked to the DP matrix element. The expression in Equation (5.7) is governed by the time-dependent spatial overlap integral between the longitudinal coherent strain field, $\eta(z,t)$, and the electric field of the backscattered probe light. In the linear regime of photoelasticity (*i. e.* for a small strain of the order of $10^{-5}/10^{-4}$), $\mathrm{d}\tilde{n}/\mathrm{d}\eta$ is assumed to be independent of the strain, thus leading to an opposite but equivalent shift in magnitude of the material optical spectrum under the application of compressive or tensile stress.

5.6 Many-body perturbation theory

To evaluate Equation (5.6), the photoelastic coefficients are needed. Since the photoelastic coefficients in the UV are not known, we rely on state-of-art band structure calculations. Even though the description of the optical response becomes challenging in the presence of strong excitonic correlations, in Refs. [87, 178] it was shown that many-body perturbation theory provides a very accurate model of the electronic and optical properties of TiO_2 single crystals. Here, we extend this approach to the case of strained anatase TiO_2, and extract the fundamental electron-phonon matrix elements that are relevant for both the generation (photoinduced strain $\eta(z,t)$) and the detection (photoelastic coefficient $\mathrm{d}\tilde{n}/\mathrm{d}\eta$) mechanisms. The details of the calculations are provided in Appendix A.3.

Briefly, the single-particle excitation spectrum of the material is calculated at the GW level while applying a 0.2% deformation of the unit cell along the [010] axis. This deformation is artificially introduced to mimic the photoinduced strain propagating in the crystal under our experimental conditions, and to study its effects on the single-particle electronic structure. In a second step, we compute the optical spectrum in the presence of many-body electron-hole correlations by solving the Bethe-Salpeter Equation (BSE) [179, 180], and study how the excitons are renormalized by the macroscopic strain field. Our theoretical analysis is performed in the case of a pristine TiO_2 crystal, taking into account only direct optical transitions and neglecting the additional screening induced by free carriers and the presence of indirect (phonon- or impurity-assisted) transitions. Although the latter effects are not expected to modify our conclusions (as discussed in Ref. [87]), they could be responsible for some of the remaining discrepancies between theory and experiment.

5.6.1 Efficiency of deformation potential mechanism

Our estimate of the DPs experienced by the lowest states in the valence (d_h) and conduction band (d_e) yields d_h = -0.066 eV/GPa and d_e = -0.096 eV/GPa. The negative sign of the DPs suggests that the photoinduced stress is compressive in nature. This allows us to evaluate the efficiency of the DP mechanism in comparison to the TE mechanism. Substituting the computed values of d_h and d_e in Equation (5.5) yields σ_{DP}/σ_{TE} = -27.47. Thus, we conclude that the deformation potential mechanism provides the dominant contribution to the generation of the observed coherent acoustic phonons. Importantly, this result can be obtained only with a reliable estimate of the DPs, as the one provided at the GW level. In contrast, when relying on the generalized-gradient approximation level of density-functional theory [181], the value σ_{DP}/σ_{TE} = -4.2 is found.

5.6.2 Computed optical spectra and photoelastic coefficients

Thereafter, we compute the dielectric function and the reflectivity in the case of the unstrained unit cell and in the presence of a tensile/compressive strain along the [010] axis, resulting in the spectra shown in Figure 5.4. We find that the exciton peak strongly reacts to the strain field, undergoing a dramatic renormalization of its energy and a pronounced modulation of its intensity. Remarkably, the peak energy shift (δE = 30 meV) and intensity change ($\Delta R/R$ = 3.5%) in the reflectivity show an excellent match with the experimental data. Moreover, the observed strain dependence of the exciton peak suggests that the photoelastic coefficients $\mathrm{d}n_1/\mathrm{d}\eta$ and $\mathrm{d}n_2/\mathrm{d}\eta$ are not symmetric upon application of compressive or tensile strain. Specifically, from the optical spectra in Figure 5.4 we see that in the presence of a tensile strain, the exciton peak undergoes a larger shift towards the red. In contrast, upon the application of a compressive strain, the exciton displays higher resistance to blueshift. The asymmetry is confirmed by comparing the photoelastic coefficients in presence of tensile and compressive strain, shown in Figure 5.5.

This intriguing aspect of anomalous renormalization of the excitonic states has never been reported or discussed so far. Most of the nonlinearities in ultrafast acoustics come from nonlinear acoustic properties illustrated by the observations of solitons [165] or shock-waves [182]. In contrast, the question of nonlinear photoelastic coefficients has never been quantitatively assessed. Our data suggest that, in the present experimental conditions, the system is driven into a non-perturbative (nonlinear) regime because the photoinduced strain is large and the damped sinusoidal acoustic signal predicted by the Thomsen model may be distorted. To simplify the modelling of our data within the perturbative regime, we calculate the photoelastic coefficients using the central finite differences method (Figure 5.6(a)). Large values are found in the vicinity of the exciton resonance, indicating that the electron-phonon coupling is effective only in this photon energy range.

Finally, we evaluate Equation (5.6) using the parameters computed above. We consider that the photoinduced DP stress is produced within the skin depth of the pump field (ξ =

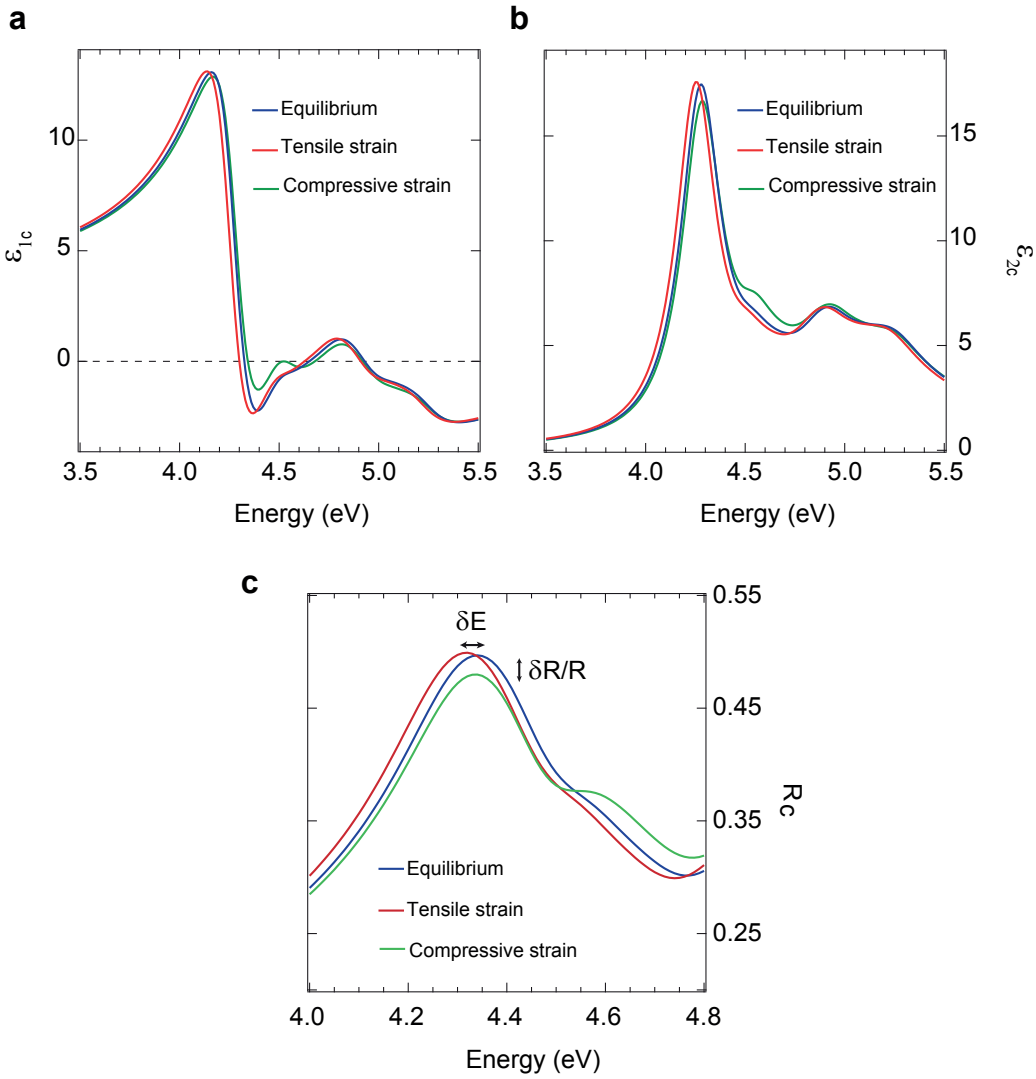

Figure 5.4 – Calculated (a) real and (b) imaginary part of the dielectric function and (c) reflectivity in the BSE-GW scheme for the equilibrium unit cell (blue curve) and in the presence of a 0.2% tensile (red curve) and compressive (green curve) strain.

$\lambda/4\pi n_2 \sim 12$ nm). Since the crystal is semi-infinite, the resulting photoinduced strain pulse is assumed to be bipolar, with $\eta(z,t) = -\eta_0 \,\mathrm{sign}(z - vt)e^{-|z-vt|/\xi}$. This assumption is reasonable as during the time range over which the phenomena are observed (0-10 ps), the acoustic pulse cannot develop an N-wave or form acoustic solitons. Based on the computed DPs and elastic properties (a bulk modulus $B = 181$ GPa), the photoinduced strain along the [010] direction is $\eta_0 = (d_e + d_h)BN/\rho v^2 \sim 10^{-3}$.

The final calculation is performed with the computed photoelastic coefficients of Figure 5.6(a), whereas the conventional approach of ultrafast acoustics (which makes use of the steady-state linear optical data) provides a poor agreement in the presence of such a high value of photoinduced strain (data not shown). Our refined model yields damped sinusoidal functions

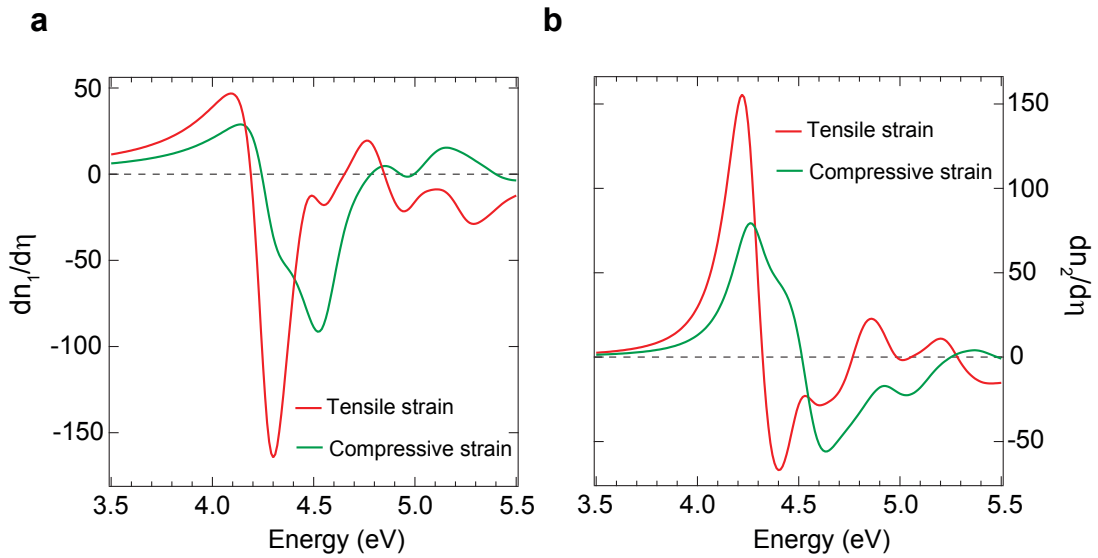

Figure 5.5 – Calculated (a) real and (b) imaginary part of the photoelastic coefficient in the presence of a 0.2% tensile (red curves) and compressive (green curves) strain. The red (green) curves have been obtained using the method of the backward (forward) differences.

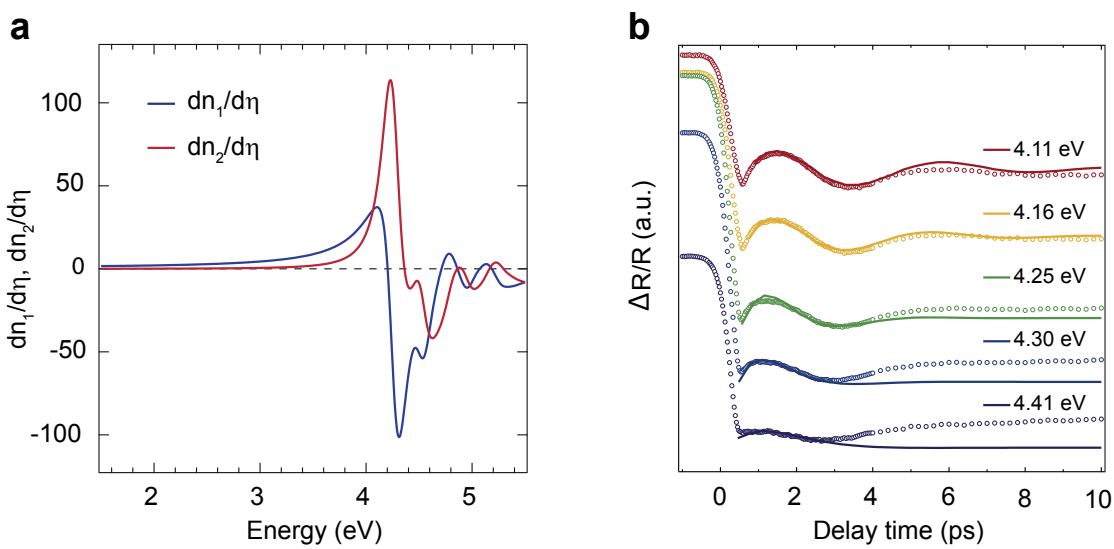

Figure 5.6 – (a) Calculated real (blue curve) and imaginary (red curve) parts of the photoelastic coefficient calculated using the central finite differences method. (b) Simulated transient acoustic response at different probe photon energies (solid lines), as indicated in the labels. The dotted lines are the experimental data.

that are shown in Figure 5.6(b) and compared with the experimental traces. We observe that the coherent response is well reproduced and the calculated frequencies ($\nu_{\mathrm{ph,th}}$, Figure 5.3) are in excellent agreement with the experimental ones. Small deviations in the modulation amplitude (by a factor of 0.6–1.2) and damping are caused by the distortion that the signal undergoes beyond the perturbative regime. More importantly, some of the traces were multiplied by –1 to match the experimental curves, implying that our model does not reproduce the phase of the modulation over the whole probed range. Indeed, the phase depends on the ratio between the real and imaginary part of the photoelastic coefficient, which are here calculated with the method of the central differences to mimic the perturbative regime of the Thomsen model. Thus, the disagreement between the phase observed in our experimental data and the one predicted by the Thomsen model shows the limit of our approach at this stage. Despite this limitation, the overall agreement between our data and the model is very good, and the *ab initio* calculations provide relevant values of physical parameters to successfully reproduce the amplitude of the transient reflectivity signal. We underline that the optical spectra calculated with the random phase approximation on top of the GW results do not provide realistic signals [87], leading to much smaller photoelastic coefficients than the experimental ones (data not shown). This highlights the importance of solving the BSE to address the impact of the lattice motion on the excitonic states, thus opening new perspectives for the accurate prediction and design of tailored exciton-phonon coupling schemes.

5.7 Conclusion

In conclusion, by combining state-of-art ultrafast broadband UV spectroscopy and many-body perturbation theory calculations, we elucidate the details of the coupling between excitons and coherent acoustic phonons in anatase TiO_2 single crystals. Efficient generation and detection of coherent acoustic phonons in the 100-200 GHz range is observed at RT in the vicinity of an exciton resonance, which is characterized by photoelastic coefficients as large as those found in the visible range for quantum confined nanostructures and an exceptional exciton band tuning of 30-50 meV with a moderate strain value. This result assumes a particular importance when compared to the coherent manipulation of excitons via the light field itself within the framework of the optical Stark effect, which so far has produced RT exciton shifts over the visible range of 10-20 meV in transition metal dichalcogenides [173, 174] and 2 meV in hybrid perovskites [175]. Thus, our findings open intriguing perpectives for UV acousto-optics and acousto-excitonics, in which the additional electronic contribution to the exciton renormalization can be suppressed by engineering a source of coherent acoustic phonons (*e. g.* a metallic film) on top of an anatase TiO_2 crystal. Finally, in analogy to the growing field of active plasmonics [183], we envision the rise of active excitonics schemes in which the excitonic transport can be selectively modulated at high-speeds by tailored opto-acoustic stimuli.

Conclusion and future directions

The research presented in my thesis demonstrates how the unique combination of ultrafast optical spectroscopy and quantitative lineshape analysis can give novel insights into the the interplay between free charge carriers, excitons, and phonons. Peculiar to our experiments is the use of photon energies above the fundamental energy gap, as well as laser fluences high enough to induce strong perturbations in the system. In this regard, the possibility to visualize the time evolution of the absorption coefficient in bulk single crystals is intriguing, as many-body effects manifest themselves as strong optical nonlinearities in the optical spectrum. Therefore, the combination of spectroscopic ellipsometry, ultrafast spectroscopy, and quantitative lineshape analysis represents a reliable approach to access the time evolution of any optical quantity of interest from the transient reflectivity signal. As we always make use of complex optical quantities, this procedure is not affected by the errors introduced by Kramers-Kronig transformations. Within this approach, a rich body of information on the spectral dynamics can be accessed, revealing new details on the effects behind exciton renormalization in hybrid perovskites and anatase titanium dioxide.

In the former case, we resolved the excitonic resonance and observed Coulomb enhancement up to e-h densities of $\sim 10^{19}\mathrm{cm}^{-3}$, also reproduced by the theoretical absorption spectra, pointing toward the existence of Mahan exciton species in $CH_3NH_3PbBr_3$. The exceptional stability of bound species in these materials against strong photoexcitation highlights the potential of hybrid perovskites in room-temperature devices which demand high injected carrier densities, and open the door to the use of these materials in the field of excitonics.

The same approach allows to study the nonequilibrium properties of in pristine and n-doped anatase TiO_2 single crystals. We observe that the photoexcited e-h plasma reduces the strength of e-h interaction via long-range Coulomb screening, while preventing the complete disappearance of the exciton lineshape. This represents a first important step towards the understanding of the role of the excitonic species in the photophysics of TiO_2, contributing to the refinement of the established description of the photophysics in this material.

Furthermore, the strong coupling between electrons and acoustic phonons in TiO_2 represents an intriguing opportunity to study the influence of the coherent acoustic field onto the excitonic correlations. We showed that in TiO_2 single crystals, coherent acoustic phonons can be launched in the material by an intense UV pump pulse, which results in the coherent

modulation of the exciton energy. This possibility is intriguing in light of future acousto-optic and acousto-excitonic applications, and the demonstration of room-temperature acoustic effects in the case of anatase TiO_2 single crystals is a step forward in this direction.

The main objective of my thesis work was to understand how excitons react to external perturbations, as photoinduced coherent strain pulses or dense e-h plasma. A natural continuation of this strand of research is represented by the use of complementary techniques to transient absorption or reflectivity. An ideal candidate is represented by luminescence spectroscopy, which is widely used for the study of microscopic physical processes in semiconductors. Similar to the absorption, the emission spectrum undergoes substantial modifications when high intensity laser pulses are shed on the material. In particular, time-resolved photoluminescence measurements can be used to elucidate the nature of photoexcitations in the material. On the one hand, the probability of radiative recombination of correlated e-h pairs (bound excitons or correlated e-h plasma) is increased several times with respect to free carriers, and each photoexcited species retains a specific luminescence spectrum. On the other hand, these effects can be often observed only at low temperature, and these technique might not be suitable for the study of room-temperature phenomena.

Here, we presented a powerful method to disentangle the many-body effects that lye at the origin of the observed optical nonlinearities, making another crucial step towards the understanding of nonequilibrium exciton physics and to the development of novel semiconductor technologies.

A Theory calculations

A.1 Theory of ionization equilibrium

The details presented in this Section are kindly provided by Dr. Alexander Steinhoff (Bremen).

Following [141] and [184], we start from the general expression for the carrier density n_a of the species (electron or hole) a

$$n_a(\mu_a, T) = \frac{i\hbar}{\mathcal{V}} \int_{-\infty}^{\infty} \frac{d\omega}{2\pi} \sum_{\mathbf{k}\sigma} f^a(\omega) A^a_{\mathbf{k}\sigma}(\omega) \,, \tag{A.1}$$

where $f^a(\omega)$ denotes the Fermi distribution function depending on μ_a and T and $\mathcal{V}$ is the crystal area. The spectral function $A^a_{\mathbf{k}\sigma}(\omega)$ of the single-particle state $|\mathbf{k}\sigma a\rangle$ with spin σ is given by

$$A^a_{\mathbf{k}\sigma}(\omega) = 2i\,\mathrm{Im}\,\frac{1}{\hbar\omega - \varepsilon^{0,a}_{\mathbf{k}\sigma} - \Sigma^{\mathrm{ret},a}_{\mathbf{k}\sigma}(\omega)} \,. \tag{A.2}$$

The self-energy $\Sigma^{\mathrm{ret},a}_{\mathbf{k}\sigma}(\omega)$ accounts for many-particle effects giving rise to renormalizations of the single-particle band structure $\varepsilon^{0,a}_{\mathbf{k}\sigma}$ as well as contributions of bound states. For a given self-energy, the inversion of Eq. (A.1) yields the chemical potential $\mu_a(n_a, T)$ for each species and therefore any thermodynamic property of the system in the grand canonical formulation. In the limit of small quasi-particle damping $\mathrm{Im}\,\Sigma^{\mathrm{ret},a} \ll \mathrm{Re}\,\Sigma^{\mathrm{ret},a}$, the spectral function can be expanded in linear order of $\mathrm{Im}\,\Sigma^{\mathrm{ret},a}$ yielding the carrier density in so-called extended quasi-particle approximation

$$\begin{aligned} & n_a(\mu_a, T) \\ & = \frac{1}{\mathcal{V}} \sum_{\mathbf{k}\sigma} f^a(\varepsilon^a_{\mathbf{k}\sigma}) \\ & - \frac{1}{\mathcal{V}} \sum_{\mathbf{k}\sigma} \int_{-\infty}^{\infty} \frac{d\omega}{2\pi} \frac{2}{\hbar} \mathrm{Im}\,\Sigma^{\mathrm{ret},a}_{\mathbf{k}\sigma}(\omega) \left[f^a(\varepsilon^a_{\mathbf{k}\sigma}) - f^a(\omega) \right] \frac{d}{d\omega} \frac{\mathscr{P}}{\omega - \varepsilon^a_{\mathbf{k}\sigma}/\hbar} \\ & = n^{\mathrm{QP}}_a + n^{\mathrm{corr}}_a \,, \end{aligned} \tag{A.3}$$

where the quasi-particle energy $\varepsilon^a_{\mathbf{k}\sigma}$ is given by $\varepsilon^a_{\mathbf{k}\sigma} = \varepsilon^{0,a}_{\mathbf{k}\sigma} + \mathrm{Re}\,\Sigma^{\mathrm{ret},a}_{\mathbf{k}\sigma}(\varepsilon^a_{\mathbf{k}\sigma})$ and $\mathscr{P}$ denotes the Cauchy principal value. The total density is divided into contributions from quasi-free particles and correlated particles, the latter being either in bound or scattering many-particle states. To evaluate the expressions (A.2) and (A.3), we have to choose an approximation for the self-energy $\Sigma^{\mathrm{ret},a}(\omega)$. The real and imaginary parts of Σ determine the quasi-particle energies and the correlated part of the carrier density, respectively. An appropriate choice is the screened ladder approximation [185–187] $\Sigma(\omega) = \Sigma^{\mathrm{H}} + \Sigma^{\mathrm{GW}}(\omega) + \Sigma^{\mathrm{T}}(\omega)$ that takes into account screening of Coulomb interaction due to excited carriers as well as the formation of bound two-particle states and consists of Hartree, GW and T-matrix contributions. We assume that renormalizations due to the Hartree self-energy are small compared to exchange and correlation effects. In the T-matrix contribution, we neglect exchange terms and assume static screening so that the T-matrix depends only on one instead of three frequency arguments. Expressing the T-matrix by its so-called bilinear expansion into two-particle eigenstates, we arrive at the final expression for the carrier density [141, 186, 186]:

$$\begin{aligned} n_a(\mu_a, T) &= \frac{1}{\mathcal{V}} \sum_{\mathbf{k}\sigma} f^a(\varepsilon^a_{\mathbf{k}\sigma}) + \frac{1}{\mathcal{V}} \sum_{b\neq a} \sum_{\sigma\sigma'} \sum_{\nu\mathbf{Q}} n^{\mathrm{B}}_{ab}(E^{\sigma\sigma'}_{\nu\mathbf{Q}}) \\ &= n^{\mathrm{GW},a}_{\mathrm{free}} + n_{\mathrm{X}}\,. \end{aligned} \tag{A.4}$$

The total carrier density separates into contributions from quasi-free carriers and from carriers bound as excitons. We identify excitons as those two-particle states $\left|\nu\sigma\sigma'\mathbf{Q}\right\rangle$ which have eigenenergies $E^{\sigma\sigma'}_{\nu\mathbf{Q}}$ below the renormalized quasi-particle gap, while contributions from scattering states above the gap are neglected for simplicity. ν describes the relative motion of electron and hole, whereas $\mathbf{Q}$ denotes the total momentum of the exciton. While unbound carriers enter the carrier density via Fermi distribution functions, exciton states are populated according to the Bose distribution function $n^{\mathrm{B}}_{ab}(\omega) = \left[\exp(\beta(\hbar\omega - \mu_a - \mu_b)) - 1\right]^{-1}$ depending on the chemical potentials of both carrier species.

For a specific material, the ionization equilibrium has to be computed numerically. The electron and hole chemical potentials are determined by adapting the Fermi functions $f^a(\varepsilon^a_{\mathbf{k}\sigma})$ of electrons and holes to a given density of quasi-free carriers at the quasi-particle energies $\varepsilon^a_{\mathbf{k}\sigma}$. As the chemical potentials also enter the bound-carrier density via the Bose function n^{B}_{ab}, Eq. (A.4) represents an implicit equation for the fraction of quasi-free carriers $\alpha_a = n^a_{\mathrm{free}}/n_a$, that has to be solved self-consistently with the quasi-particle energies in GW approximation, see Eq. (A.10), and the bound-state energies $E^{\sigma\sigma'}_{\nu\mathbf{Q}}$. The quasi-particle renormalizations are evaluated using only the quasi-free carrier density. Also, dynamical screening of the Coulomb interaction only due to free carriers is taken into account, while dipolar screening due to excitons is assumed to be weak. The free-carrier screening is treated in RPA with a macroscopic Lindhard dielectric function [188]. To further simplify the procedure, we exploit the fact that shifts of excitonic resonances are naturally much smaller than band-gap shifts, which is due to compensation effects between gap shrinkage and binding-energy reduction. Hence we assume that the exciton spectrum depends only weakly on the excitation density so that we can limit ourselves to the exciton spectrum in the limit of zero excitation density.

A.2 Semiconductor Bloch Equations

The details presented in this Section are kindly provided by Dr. Alexander Steinhoff (Bremen).

The absorption of a semiconductor medium is obtained from its linear response to a classical electric field $\mathbf{E}(t)$ [1]. The electric field drives a macroscopic polarization of the medium that is composed of the microscopic inter-band polarizations $\psi^{\mathrm{he}}_{\mathbf{k}}(t) = \langle a^{\mathrm{h}}_{\mathbf{k}} a^{\mathrm{e}}_{\mathbf{k}} \rangle(t)$, with the annihilation operator $a^{\mathrm{e/h}}_{\mathbf{k}}$ of electrons and holes, according to $\mathbf{P}(t) = \frac{1}{\mathcal{V}} \sum_{\mathbf{k},\mathrm{eh}} \psi^{\mathrm{he}}_{\mathbf{k}}(t)(\mathbf{d}^{\mathrm{eh}}_{\mathbf{k}})^* +$ c.c.. Here, $\mathcal{V}$ is the crystal volume and $\mathbf{d}^{\mathrm{eh}}_{\mathbf{k}}$ are dipole matrix elements describing the efficiency of light-matter coupling depending on the momentum $\mathbf{k}$. In the regime of weak excitation, the macroscopic polarization is linear in the electric field. This allows to extract the response of the medium as a pure material property in the form of a susceptibility that is independent of the electric field:

$$\chi(\omega) = \frac{P(\omega)}{\varepsilon_0 E(\omega)}\,, \tag{A.5}$$

where we consider an isotropic susceptibility χ. To obtain the frequency-dependent response of the medium, we use the Fourier transform of the macroscopic polarization $\mathbf{P}(t)$, assuming the medium to be in a quasi-equilibrium state. In this picture, any excited carriers that are generated by pumping the active medium relax to quasi-equilibrium distributions at a certain temperature and carrier density. The absorption at these parameters is then probed by the weak electric test field.

Applying the technique of nonequilibrium Green functions, the equation of motion for microscopic inter-band polarizations known as *semiconductor Bloch equations* (SBE) can be derived [143, 144]. As shown in [145], the SBE are transformed into frequency space taking into account many-body effects due to excited carriers on a GW-level:

$$\begin{aligned}
&\Big(\hbar\omega - \varepsilon^{\mathrm{HF,h}}_{\mathbf{k}} - \varepsilon^{\mathrm{HF,e}}_{\mathbf{k}} - \Delta^{\mathrm{eh}}_{\mathbf{k}}(\omega) + i\gamma^{\mathrm{El\text{-}Ph}}\Big)\psi^{\mathrm{he}}_{\mathbf{k}}(\omega) \\
&\quad + \Big(1 - f^{\mathrm{e}}_{\mathbf{k}} - f^{\mathrm{h}}_{\mathbf{k}}\Big)\Big(\mathbf{d}^{eh}_{\mathbf{k}} \cdot \mathbf{E}(\omega) + \frac{1}{\mathcal{V}} \sum_{\mathbf{k}'} V_{|\mathbf{k}-\mathbf{k}'|} \psi^{\mathrm{he}}_{\mathbf{k}'}(\omega)\Big) \\
&\qquad + \frac{1}{\mathcal{V}} \sum_{\mathbf{k}'} V^{\mathrm{eff,eh}}_{\mathbf{k}\mathbf{k}'}(\omega) \psi^{\mathrm{he}}_{\mathbf{k}'}(\omega) = 0\,.
\end{aligned} \tag{A.6}$$

Just as the well-known Bethe-Salpeter equation in screened ladder approximation [189, 190], the SBE on GW-level describe two-particle states in the presence of a dynamically screened carrier-carrier interaction. The single-particle energies $\varepsilon^{\mathrm{HF,e/h}}_{\mathbf{k}}$ contain renormalization effects on a Hartree-Fock level. The second line contains the light-matter coupling term $\mathbf{d} \cdot \mathbf{E}$ of the materials' dipoles to the external field as well as a two-body interaction term facilitating excitonic resonances in the optical response. These terms are modified by a Pauli-blocking factor given by the electron and hole occupancies for which we assume Fermi distribution functions. Consistent with the theory of ionization equilibrium, the Fermi functions describe only quasi-free carriers, while we assume that renormalization effects due to excitons can be

neglected. As we focus on the microscopic description of effects induced by excited carriers, we include dephasing contributions due to carrier-phonon interaction on a phenomenological level by adding a constant imaginary part $\gamma^{\text{El-Ph}}$ to the quasi-particle energies. The constant is chosen as $\gamma^{\text{El-Ph}} = 30$ meV according to [139]. Following this reference, we additionally include inhomogeneous broadening caused by impurities by convoluting the susceptibility $\chi(\omega)$ with a Gaussian with 16 meV HWHM.

All many-body effects induced by carrier-carrier interaction beyond the Hartree-Fock level are contained in the correlation terms

$$\begin{aligned} V^{\text{eff,eh}}_{\mathbf{k}\mathbf{k}'}(\omega) = i\hbar \int_{-\infty}^{\infty} \frac{d\omega'}{2\pi} \Bigg\{ & \\ & \frac{(1 - f^{\text{h}}_{\mathbf{k}} + n_{\text{B}}(\omega'))2i\,\text{Im}\, W^{\text{ret}}_{|\mathbf{k}-\mathbf{k}'|}(\omega')}{\hbar\omega - \varepsilon^{\text{h}}_{\mathbf{k}} - \varepsilon^{\text{e}}_{\mathbf{k}'} + i\Gamma^{\text{h}}_{\mathbf{k}} + i\Gamma^{\text{e}}_{\mathbf{k}'} - \hbar\omega'} \\ & + \frac{(1 - f^{\text{e}}_{\mathbf{k}} + n_{\text{B}}(\omega'))2i\,\text{Im}\, W^{\text{ret}}_{|\mathbf{k}-\mathbf{k}'|}(\omega')}{\hbar\omega - \varepsilon^{\text{e}}_{\mathbf{k}} - \varepsilon^{\text{h}}_{\mathbf{k}'} + i\Gamma^{\text{e}}_{\mathbf{k}} + i\Gamma^{\text{h}}_{\mathbf{k}'} - \hbar\omega'} \Bigg\}, \end{aligned} \tag{A.7}$$

with the Bose distribution function $n_{\text{B}}(\omega)$ and Fermi distribution function $f^{\text{e/h}}_{\mathbf{k}}$, and

$$\begin{aligned} \Delta^{\text{eh}}_{\mathbf{k}}(\omega) = & \Sigma^{\text{MW,ret,e}}_{\mathbf{k}}(\hbar\omega - \varepsilon^{\text{h}}_{\mathbf{k}} + i\Gamma^{\text{h}}_{\mathbf{k}}) \\ & + \Sigma^{\text{MW,ret,h}}_{\mathbf{k}}(\hbar\omega - \varepsilon^{\text{e}}_{\mathbf{k}} + i\Gamma^{\text{e}}_{\mathbf{k}}), \end{aligned} \tag{A.8}$$

where the Montroll-Ward (MW) self-energy

$$\begin{aligned} \Sigma^{\text{MW,ret},\lambda}_{\mathbf{k}}(\omega) = i\hbar \int_{-\infty}^{\infty} \frac{d\omega'}{2\pi} \\ \frac{1}{\mathcal{V}} \sum_{\mathbf{k}'} \frac{(1 - f^{\lambda}(\omega - \omega') + n_{\text{B}}(\omega'))2i\,\text{Im}\, W^{\text{ret}}_{|\mathbf{k}-\mathbf{k}'|}(\omega')}{\hbar\omega - \varepsilon^{\lambda}_{\mathbf{k}'} + i\Gamma^{\lambda}_{\mathbf{k}'} - \hbar\omega'} \end{aligned} \tag{A.9}$$

is responsible for quasi-particle renormalizations beyond Hartree-Fock according to

$$\varepsilon^{\lambda}_{\mathbf{k}} = \varepsilon^{0,\lambda}_{\mathbf{k}} + \Sigma^{\text{HF},\lambda}_{\mathbf{k}} + \text{Re}\,\Sigma^{\text{MW,ret},\lambda}_{\mathbf{k}}(\omega)\Big|_{\omega=\varepsilon^{\lambda}_{\mathbf{k}}/\hbar}. \tag{A.10}$$

The corresponding quasi-particle broadening follows from the imaginary part of the MW self-energy:

$$\Gamma^{\lambda}_{\mathbf{k}} = -\text{Im}\,\Sigma^{\text{MW,ret},\lambda}_{\mathbf{k}}(\omega)\Big|_{\omega=\varepsilon^{\lambda}_{\mathbf{k}}/\hbar}. \tag{A.11}$$

For the band-structure energies $\varepsilon^{0,\lambda}_{\mathbf{k}}$ in the absence of excitation-induced renormalizations we apply an effective mass approximation with the effective masses given in the main text following [51]. The correlation terms (A.7)-(A.9) contain the retarded screened potential $W^{\text{ret}}_{|\mathbf{k}-\mathbf{k}'|} = V_{|\mathbf{k}-\mathbf{k}'|}\varepsilon^{-1}_{\text{exc},|\mathbf{k}-\mathbf{k}'|}(\omega)$, where the inverse dielectric function $\varepsilon^{-1}_{\text{exc},\mathbf{q}}(\omega)$ describes screening due to (unbound) excited carriers in random phase approximation (RPA). Additionally, $V_{|\mathbf{k}-\mathbf{k}'|}$

is screened by carriers in filled valence-band states, which we describe by an effective dielectric constant (see Section 3.3). The SBE (Eq. A.6) are numerically solved by matrix inversion for each frequency to obtain the frequency-dependent microscopic polarization and thereby the optical susceptibility using Eq. (A.5).

A.3 Many-body perturbartion theory

The details presented in this Section are kindly provided by Dr. Adriel Dominguez (Hamburg).

Many-body perturbation theory at the level of the GW and the Bethe-Salpeter Equation (BSE) [179] was employed to compute the band structure and the dielectric response of bulk anatase TiO_2. The GW and BSE calculations were performed on-top of eigenvalues and eigenfunctions obtained from DFT. We used the planewave pseudopotential implementation of DFT as provided by the package Quantum Espresso. GW and BSE calculations were performed with the BerkeleyGW package [191].

The DFT calculations were performed using the generalized gradient approximation (GGA) as in the Perdew-Burke-Ernzerhof (PBE) scheme for the exchange-correlation functional. The Ti norm-conserving pseudopotential was generated in the Rappe-Rabe-Kaxiras-Joannopoulos (RRKJ) scheme [192], including semicore 3s and 3p states. While standard structural and electronic quantities are already converged in DFT with an energy cutoff of 90 Ry, the energy cutoff used here was raised to 160 Ry to properly include the high number of bands necessary to reach convergence for the many-body evaluated properties. Bulk anatase TiO_2 was modeled on a body-centered tetragonal lattice containing 2 Ti atoms and 4 O atoms (primitive cell) with lattice parameters (optimized at the PBE level) a = b = 3.79 Å and c = 9.66 Å. The experimental lattice constants at RT are a = b = 3.78 Å and c = 9.51 Å. Scaling these parameters to zero temperature via a linear extrapolation of the temperature dependence of the lattice constant at high temperature, appearing in Ref. [193], yields a = b = 3.78 Å and c = 9.49 Å.

The ground state electronic density is properly described with a coarse 4×4×4 k-point grid for sampling of the BZ. The GW quasiparticle corrections to the DFT eigenvalues were performed at the one-shot level of theory (G_0W_0). For the computation of the polarizability and inverse dielectric matrices in BerkeleyGW, we employed a total of 2474 CBs and G-vectors with kinetic energies up to 46 Ry, whereas the self-energy operator was computed using 2472 unoccupied bands and a G-vector cutoff energy of 46 Ry and 160 Ry for the screened and bare Coulomb matrices, respectively. The coarse 4×4×4 k-point grid sampling is sufficient for the description of the quasiparticle corrections, while a high number of bands is mandatory to get a proper description of screening effects and many-body corrections. The electronic band structure was finally obtained by interpolating GW corrections on top of a more refined DFT calculation with a 16×16×16 grid. The fully converged BSE results shown in the main text were obtained with BerkeleyGW. We used a shifted grid with up to 16×16×16 k-points (4096 irreducible k-points). The six lowest CBs and six topmost VBs were included to solve the excitonic Hamiltonian. Spin-polarized calculations were performed to highlight possible dark excitons due to triplet

excitations but no measurable differences with respect to the spin-restricted results were obtained. More details are provided in Ref. [87].

We solved the Bethe-Salpeter equation (BSE) on top of GW electronic structure calculations to compute the electrodynamic properties of pristine anatase TiO_2. Figure 5.4(a,b) shows the real and imaginary part of the dielectric function calculated in the case of the unstrained unit cell (blue curves), and in the presence of a 0.2% tensile (red curves) and compressive (green curves) strain along the [010] axis, respectively. The calculation was perfomed over the 1.50-5.50 eV energy range, but we display the data between 3.50 eV and 5.50 eV for clarity. The resulting photoelastic coefficients $\mathrm{d}n_1/\mathrm{d}\eta$ and $\mathrm{d}n_2/\mathrm{d}\eta$ for the cases of tensile (red curves) and compressive (green curves) strain are presented in Figure 5.5 , as computed with the method of backward and forward differences, respectively. We observe an asymmetry between the photoelastic coefficients, which suggests a departure from the assumption that the photoelastic coefficients are independent of the applied strain direction. This effect can be understood by considering a Taylor expansion to the complex refractive index $\tilde{n}$

$$\tilde{n} = \tilde{n}_0 + \frac{d\tilde{n}}{d\eta}\eta + \frac{1}{2}\frac{d^2\tilde{n}}{d\eta^2}\eta^2. \tag{A.12}$$

We note that if the strain η changes its sign (compression-expansion), then the existence of non-vanishing second-order term explains the asymmetric variation of the refractive index ($\Delta\tilde{n} = \tilde{n}$ - $\tilde{n}_0$) for compression/expansion.

Bibliography

[1] H. Haug and S. W. Koch, *Quantum Theory of the Optical and Electronic Properties of Semiconductors: Fivth Edition.* World Scientific Publishing Company, 2009.

[2] I. Pelant and J. Valenta, *Luminescence spectroscopy of semiconductors.* Oxford University Press, 2012.

[3] R. Elliott, "Intensity of optical absorption by excitons", *Physical Review*, vol. 108, no. 6, p. 1384, 1957.

[4] *Wikipedia Commons.* [(https://commons.wikimedia.org/wiki/File:Linear_absorption_spectrum_of_bulk_GaAs.png#filelinks) accessed on 1st November 2018].

[5] J. Shah, *Ultrafast spectroscopy of semiconductors and semiconductor nanostructures*, vol. 115. Springer Science & Business Media, 2013.

[6] C. F. Klingshirn, *Semiconductor optics.* Springer Science & Business Media, 2012.

[7] M. Feneberg, S. Osterburg, K. Lange, C. Lidig, B. Garke, R. Goldhahn, E. Richter, C. Netzel, M. D. Neumann, N. Esser, *et al.*, "Band gap renormalization and burstein-moss effect in silicon-and germanium-doped wurtzite gan up to 10 20 cm- 3", *Physical Review B*, vol. 90, no. 7, p. 075203, 2014.

[8] E. A. A. Pogna, M. Marsili, D. De Fazio, S. Dal Conte, C. Manzoni, D. Sangalli, D. Yoon, A. Lombardo, A. C. Ferrari, A. Marini, G. Cerullo, and D. Prezzi, "Photo-Induced Bandgap Renormalization Governs the Ultrafast Response of Single-Layer MoS_2", *ACS Nano*, vol. 10, no. 1, pp. 1182–1188, 2016.

[9] R. Ambigapathy, I. Bar-Joseph, D. Y. Oberli, S. Haacke, M. J. Brasil, F. Reinhardt, E. Kapon, and B. Deveaud, "Coulomb Correlation and Band Gap Renormalization at High Carrier Densities in Quantum Wires", *Phys. Rev. Lett.*, vol. 78, no. 18, p. 3579, 1997.

[10] D. Reynolds, D. C. Look, and B. Jogai, "Combined Effects of Screening and Band Gap Renormalization on the Energy of Optical Transitions in ZnO and GaN", *J. Appl. Phys.*, vol. 88, no. 10, pp. 5760–5763, 2000.

[11] S. D. Sarma and D. W. Wang, "Many-Body Renormalization of Semiconductor Quantum Wire Excitons: Absorption, Gain, Binding, and Unbinding", *Phys. Rev. Lett.*, vol. 84, no. 9, p. 2010, 2000.

[12] M. Stopa, "Band-Gap Renormalization and Excitonic Binding in T-Shaped Quantum Wires", *Phys. Rev. B*, vol. 63, no. 19, p. 195312, 2001.

[13] N. Mott, "Metal-insulator transition", *Reviews of Modern Physics*, vol. 40, no. 4, p. 677, 1968.

[14] S. Glutsch, *Excitons in low-dimensional semiconductors: theory numerical methods applications*, vol. 141. Springer Science & Business Media, 2013.

[15] A. Othonos, "Probing ultrafast carrier and phonon dynamics in semiconductors", *J. Appl. Phys.*, vol. 83, no. 4, pp. 1789–1830, 1998.

[16] J. M. Richter, F. Branchi, F. V. de Almeida Camargo, B. Zhao, R. H. Friend, G. Cerullo, and F. Deschler, "Ultrafast carrier thermalization in lead iodide perovskite probed with two-dimensional electronic spectroscopy", *Nature communications*, vol. 8, no. 1, p. 376, 2017.

[17] L. M. Herz, "Charge-carrier dynamics in organic-inorganic metal halide perovskites", *Annual review of physical chemistry*, vol. 67, pp. 65–89, 2016.

[18] E. Baldini, T. Palmieri, E. Pomarico, G. Auböck, and M. Chergui, "Clocking the ultrafast electron cooling in anatase titanium dioxide nanoparticles", *ACS Photonics*, vol. 5, no. 4, pp. 1241–1249, 2018.

[19] A. Kojima, K. Teshima, Y. Shirai, and T. Miyasaka, "Organometal halide perovskites as visible-light sensitizers for photovoltaic cells", *Journal of the American Chemical Society*, vol. 131, no. 17, pp. 6050–6051, 2009.

[20] "Best Research-Cell Efficiencies", *National Renewable Energy Laboratory (NREL)*, 2018. [Online resource (https://www.nrel.gov/pv/assets/pdfs/pv-efficiencies-07-17-2018.pdf/) accessed on 18 September 2018].

[21] S. D. Stranks and H. J. Snaith, "Metal-halide perovskites for photovoltaic and light-emitting devices", *Nature nanotechnology*, vol. 10, no. 5, p. 391, 2015.

[22] L. Etgar, P. Gao, Z. Xue, Q. Peng, A. K. Chandiran, B. Liu, M. K. Nazeeruddin, and M. Grätzel, "Mesoscopic $CH_3NH_3PbI_3/TiO_2$ heterojunction solar cells", *Journal of the American Chemical Society*, vol. 134, no. 42, pp. 17396–17399, 2012.

[23] S. D. Stranks, G. E. Eperon, G. Grancini, C. Menelaou, M. J. Alcocer, T. Leijtens, L. M. Herz, A. Petrozza, and H. J. Snaith, "Electron-hole diffusion lengths exceeding 1 micrometer in an organometal trihalide perovskite absorber", *Science*, vol. 342, no. 6156, pp. 341–344, 2013.

[24] F. Hao, C. C. Stoumpos, D. H. Cao, R. P. Chang, and M. G. Kanatzidis, "Lead-free solid-state organic-inorganic halide perovskite solar cells", *Nature Photonics*, vol. 8, no. 6, pp. 489–494, 2014.

[25] M. Liu, M. B. Johnston, and H. J. Snaith, "Efficient planar heterojunction perovskite solar cells by vapour deposition", *Nature*, vol. 501, no. 7467, pp. 395–398, 2013.

[26] O. Malinkiewicz, A. Yella, Y. H. Lee, G. M. Espallargas, M. Graetzel, M. K. Nazeeruddin, and H. J. Bolink, "Perovskite solar cells employing organic charge-transport layers", *Nature Photonics*, vol. 8, no. 2, pp. 128–132, 2014.

[27] O. D. Miller, E. Yablonovitch, and S. R. Kurtz, "Strong internal and external luminescence as solar cells approach the shockley–queisser limit", *IEEE Journal of Photovoltaics*, vol. 2, no. 3, pp. 303–311, 2012.

[28] Z.-K. Tan, R. S. Moghaddam, M. L. Lai, P. Docampo, R. Higler, F. Deschler, M. Price, A. Sadhanala, L. M. Pazos, D. Credgington, *et al.*, "Bright light-emitting diodes based on organometal halide perovskite", *Nature nanotechnology*, vol. 9, no. 9, pp. 687–692, 2014.

[29] G. Xing, N. Mathews, S. S. Lim, N. Yantara, X. Liu, D. Sabba, M. Grätzel, S. Mhaisalkar, and T. C. Sum, "Low-temperature solution-processed wavelength-tunable perovskites for lasing", *Nature materials*, vol. 13, no. 5, p. 476, 2014.

[30] F. Deschler, M. Price, S. Pathak, L. E. Klintberg, D.-D. Jarausch, R. Higler, S. Hüttner, T. Leijtens, S. D. Stranks, H. J. Snaith, *et al.*, "High photoluminescence efficiency and optically pumped lasing in solution-processed mixed halide perovskite semiconductors", *The journal of physical chemistry letters*, vol. 5, no. 8, pp. 1421–1426, 2014.

[31] M. Grätzel, "The light and shade of perovskite solar cells", *Nature materials*, vol. 13, no. 9, pp. 838–842, 2014.

[32] M. A. Green, A. Ho-Baillie, and H. J. Snaith, "The emergence of perovskite solar cells", *Nature Photonics*, vol. 8, no. 7, pp. 506–514, 2014.

[33] P. Docampo, S. Guldin, T. Leijtens, N. K. Noel, U. Steiner, and H. J. Snaith, "Lessons learned: from dye-sensitized solar cells to all-solid-state hybrid devices", *Advanced Materials*, vol. 26, no. 24, pp. 4013–4030, 2014.

[34] M. Grätzel, "The rise of highly efficient and stable perovskite solar cells", *Accounts of chemical research*, vol. 50, no. 3, pp. 487–491, 2017.

[35] N. Kitazawa, Y. Watanabe, and Y. Nakamura, "Optical properties of $CH_3NH_3PbX_3$ (X= halogen) and their mixed-halide crystals", *Journal of Materials Science*, vol. 37, no. 17, pp. 3585–3587, 2002.

[36] H.-S. Kim, C.-R. Lee, J.-H. Im, K.-B. Lee, T. Moehl, A. Marchioro, S.-J. Moon, R. Humphry-Baker, J.-H. Yum, J. E. Moser, *et al.*, "Lead iodide perovskite sensitized all-solid-state submicron thin film mesoscopic solar cell with efficiency exceeding 9%", *Scientific reports*, vol. 2, 2012.

[37] J. H. Noh, S. H. Im, J. H. Heo, T. N. Mandal, and S. I. Seok, "Chemical management for colorful, efficient, and stable inorganic–organic hybrid nanostructured solar cells", *Nano letters*, vol. 13, no. 4, pp. 1764–1769, 2013.

[38] H. Thomas and K. Müller, "Structural phase transitions in perovskite-type crystals", *Physical Review Letters*, vol. 21, no. 17, p. 1256, 1968.

[39] Y. Kawamura, H. Mashiyama, and K. Hasebe, "Structural study on cubic–tetragonal transition of $CH_3NH_3PbI_3$", *Journal of the Physical Society of Japan*, vol. 71, no. 7, pp. 1694–1697, 2002.

[40] T. Baikie, Y. Fang, J. M. Kadro, M. Schreyer, F. Wei, S. G. Mhaisalkar, M. Graetzel, and T. J. White, "Synthesis and crystal chemistry of the hybrid perovskite $CH_3NH_3PbI_3$ for solid-state sensitised solar cell applications", *Journal of Materials Chemistry A*, vol. 1, no. 18, pp. 5628–5641, 2013.

[41] C. C. Stoumpos, C. D. Malliakas, and M. G. Kanatzidis, "Semiconducting tin and lead iodide perovskites with organic cations: phase transitions, high mobilities, and near-infrared photoluminescent properties", *Inorganic chemistry*, vol. 52, no. 15, pp. 9019–9038, 2013.

[42] K. Yamada, H. Kawaguchi, T. Matsui, T. Okuda, and S. Ichiba, "Structural phase transition and electrical conductivity of the perovskite $CH_3NH_3Sn_{1-x}Pb_xBr_3$ and $CsSnBr_3$", *Bulletin of the Chemical Society of Japan*, vol. 63, no. 9, pp. 2521–2525, 1990.

[43] K. Tanaka, T. Takahashi, T. Ban, T. Kondo, K. Uchida, and N. Miura, "Comparative study on the excitons in lead-halide-based perovskite-type crystals $CH_3NH_3PbBr_3$ and $CH_3NH_3PbI_3$", *Solid State Communications*, vol. 127, no. 9, pp. 619–623, 2003.

[44] E. Mosconi, A. Amat, M. K. Nazeeruddin, M. Grätzel, and F. De Angelis, "First-principles modeling of mixed halide organometal perovskites for photovoltaic applications", *The Journal of Physical Chemistry C*, vol. 117, no. 27, pp. 13902–13913, 2013.

[45] C. Quarti, G. Grancini, E. Mosconi, P. Bruno, J. M. Ball, M. M. Lee, H. J. Snaith, A. Petrozza, and F. D. Angelis, "The raman spectrum of the $CH_3NH_3PbI_3$ hybrid perovskite: interplay of theory and experiment", *The Journal of Physical Chemistry Letters*, vol. 5, no. 2, pp. 279–284, 2013.

[46] J. Even, L. Pedesseau, J.-M. Jancu, and C. Katan, "Importance of spin–orbit coupling in hybrid organic/inorganic perovskites for photovoltaic applications", *The Journal of Physical Chemistry Letters*, vol. 4, no. 17, pp. 2999–3005, 2013.

[47] J. Even, L. Pedesseau, and C. Katan, "Analysis of multivalley and multibandgap absorption and enhancement of free carriers related to exciton screening in hybrid perovskites", *The Journal of Physical Chemistry C*, vol. 118, no. 22, pp. 11566–11572, 2014.

[48] J. M. Frost, K. T. Butler, F. Brivio, C. H. Hendon, M. Van Schilfgaarde, and A. Walsh, "Atomistic origins of high-performance in hybrid halide perovskite solar cells", *Nano letters*, vol. 14, no. 5, pp. 2584–2590, 2014.

[49] F. Brivio, K. T. Butler, A. Walsh, and M. Van Schilfgaarde, "Relativistic quasiparticle self-consistent electronic structure of hybrid halide perovskite photovoltaic absorbers", *Physical Review B*, vol. 89, no. 15, p. 155204, 2014.

[50] M. R. Filip and F. Giustino, "GW quasiparticle band gap of the hybrid organic-inorganic perovskite $CH_3NH_3PbI_3$: Effect of spin-orbit interaction, semicore electrons, and self-consistency", *Physical Review B*, vol. 90, no. 24, p. 245145, 2014.

[51] M. Bokdam, T. Sander, A. Stroppa, S. Picozzi, D. Sarma, C. Franchini, and G. Kresse, "Role of polar phonons in the photo excited state of metal halide perovskites", *Scientific reports*, vol. 6, p. 28618, 2016.

[52] F. Brivio, A. B. Walker, and A. Walsh, "Structural and electronic properties of hybrid perovskites for high-efficiency thin-film photovoltaics from first-principles", *Apl Materials*, vol. 1, no. 4, p. 042111, 2013.

[53] D. B. Mitzi, K. Chondroudis, and C. R. Kagan, "Organic-inorganic electronics", *IBM journal of research and development*, vol. 45, no. 1, pp. 29–45, 2001.

[54] Q. Lin, A. Armin, R. C. R. Nagiri, P. L. Burn, and P. Meredith, "Electro-optics of perovskite solar cells", *Nature Photonics*, 2014.

[55] Z. Xiao, R. A. Kerner, L. Zhao, N. L. Tran, K. M. Lee, T.-W. Koh, G. D. Scholes, and B. P. Rand, "Efficient perovskite light-emitting diodes featuring nanometre-sized crystallites", *Nature Photonics*, vol. 11, no. 2, p. 108, 2017.

[56] P. Odenthal, W. Talmadge, N. Gundlach, R. Wang, C. Zhang, D. Sun, Z.-G. Yu, Z. V. Vardeny, and Y. S. Li, "Spin-polarized exciton quantum beating in hybrid organic–inorganic perovskites", *Nature Physics*, vol. 13, no. 9, p. 894, 2017.

[57] M. Kim, J. Im, A. J. Freeman, J. Ihm, and H. Jin, "Switchable s= 1/2 and j= 1/2 rashba bands in ferroelectric halide perovskites", *Proceedings of the National Academy of Sciences*, p. 201405780, 2014.

[58] D. Niesner, M. Wilhelm, I. Levchuk, A. Osvet, S. Shrestha, M. Batentschuk, C. Brabec, and T. Fauster, "Giant rashba splitting in $CH_3NH_3PbI_3$ organic-inorganic perovskite", *Physical review letters*, vol. 117, no. 12, p. 126401, 2016.

[59] M. Hirasawa, T. Ishihara, T. Goto, K. Uchida, and N. Miura, "Magnetoabsorption of the lowest exciton in perovskite-type compound $CH_3NH_3PbI_3$", *Physica B: Condensed Matter*, vol. 201, pp. 427–430, 1994.

[60] V. D Innocenzo, G. Grancini, M. J. Alcocer, A. R. S. Kandada, S. D. Stranks, M. M. Lee, G. Lanzani, H. J. Snaith, and A. Petrozza, "Excitons versus free charges in organo-lead tri-halide perovskites", *Nature Communications*, vol. 5, 2014.

[61] T. J. Savenije, C. S. Ponseca Jr, L. Kunneman, M. Abdellah, K. Zheng, Y. Tian, Q. Zhu, S. E. Canton, I. G. Scheblykin, T. Pullerits, *et al.*, "Thermally activated exciton dissociation and recombination control the carrier dynamics in organometal halide perovskite", *The journal of physical chemistry letters*, vol. 5, no. 13, pp. 2189–2194, 2014.

[62] A. Miyata, A. Mitioglu, P. Plochocka, O. Portugall, J. T.-W. Wang, S. D. Stranks, H. J. Snaith, and R. J. Nicholas, "Direct measurement of the exciton binding energy and effective masses for charge carriers in an organic-inorganic tri-halide perovskite", *Nature Physics*, 2015.

[63] M. Saba, M. Cadelano, D. Marongiu, F. Chen, V. Sarritzu, N. Sestu, C. Figus, M. Aresti, R. Piras, A. G. Lehmann, *et al.*, "Correlated electron–hole plasma in organometal perovskites", *Nature Communications*, vol. 5, 2014.

[64] N. Sestu, M. Cadelano, V. Sarritzu, F. Chen, D. Marongiu, R. Piras, M. Mainas, F. Quochi, M. Saba, A. Mura, *et al.*, "Absorption f-sum rule for the exciton binding energy in methylammonium lead halide perovskites", *The journal of physical chemistry letters*, vol. 6, no. 22, pp. 4566–4572, 2015.

[65] M. B. Price, J. Butkus, T. C. Jellicoe, A. Sadhanala, A. Briane, J. E. Halpert, K. Broch, J. M. Hodgkiss, R. H. Friend, and F. Deschler, "Hot-carrier cooling and photoinduced refractive index changes in organic–inorganic lead halide perovskites", *Nature communications*, vol. 6, p. 8420, 2015.

[66] G. Grancini, A. R. S. Kandada, J. M. Frost, A. J. Barker, M. De Bastiani, M. Gandini, S. Marras, G. Lanzani, A. Walsh, and A. Petrozza, "Role of microstructure in the electron–hole interaction of hybrid lead halide perovskites", *Nature Photonics*, vol. 9, no. 10, pp. 695–701, 2015.

[67] Y. Yang, D. P. Ostrowski, R. M. France, K. Zhu, J. Van De Lagemaat, J. M. Luther, and M. C. Beard, "Observation of a hot-phonon bottleneck in lead-iodide perovskites", *Nature Photonics*, vol. 10, no. 1, pp. 53–59, 2016.

[68] C. L. Davies, M. R. Filip, J. B. Patel, T. W. Crothers, C. Verdi, A. D. Wright, R. L. Milot, F. Giustino, M. B. Johnston, and L. M. Herz, "Bimolecular recombination in methylammonium lead triiodide perovskite is an inverse absorption process", *Nature communications*, vol. 9, no. 1, p. 293, 2018.

[69] M. Hirasawa, T. Ishihara, and T. Goto, "Exciton features in 0-, 2-, and 3-dimensional networks of PbI_6 4-octahedra", *Journal of the Physical Society of Japan*, vol. 63, no. 10, pp. 3870–3879, 1994.

[70] E. A. Muljarov, S. Tikhodeev, N. Gippius, and T. Ishihara, "Excitons in self-organized semiconductor/insulator superlattices: PbI-based perovskite compounds", *Physical Review B*, vol. 51, no. 20, p. 14370, 1995.

[71] M. E. Ziffer, J. C. Mohammed, and D. S. Ginger, "Electroabsorption spectroscopy measurements of the exciton binding energy, electron–hole reduced effective mass, and band gap in the perovskite $CH_3NH_3PbI_3$", *ACS Photonics*, vol. 3, no. 6, pp. 1060–1068, 2016.

[72] J. Tilchin, D. N. Dirin, G. I. Maikov, A. Sashchiuk, M. V. Kovalenko, and E. Lifshitz, "Hydrogen-like wannier–mott excitons in single crystal of methylammonium lead bromide perovskite", *ACS nano*, vol. 10, no. 6, pp. 6363–6371, 2016.

[73] Q. Lin, A. Armin, R. C. R. Nagiri, P. L. Burn, and P. Meredith, "Electro-optics of perovskite solar cells", *Nature Photonics*, vol. 9, no. 2, p. 106, 2015.

[74] S. M. Vorpahl, S. D. Stranks, H. Nagaoka, G. E. Eperon, M. E. Ziffer, H. J. Snaith, D. S. Ginger, *et al.*, "Impact of microstructure on local carrier lifetime in perovskite solar cells", *Science*, p. aaa5333, 2015.

[75] T. Yamada, T. Aharen, and Y. Kanemitsu, "Near-band-edge optical responses of ch 3 nh 3 pbcl 3 single crystals: Photon recycling of excitonic luminescence", *Physical review letters*, vol. 120, no. 5, p. 057404, 2018.

[76] A. M. Leguy, P. Azarhoosh, M. I. Alonso, M. Campoy-Quiles, O. J. Weber, J. Yao, D. Bryant, M. T. Weller, J. Nelson, A. Walsh, *et al.*, "Experimental and theoretical optical properties of methylammonium lead halide perovskites", *Nanoscale*, vol. 8, no. 12, pp. 6317–6327, 2016.

[77] J.-S. Park, S. Choi, Y. Yan, Y. Yang, J. M. Luther, S.-H. Wei, P. Parilla, and K. Zhu, "Electronic structure and optical properties of α-$CH_3NH_3PbBr_3$ perovskite single crystal", *The journal of physical chemistry letters*, vol. 6, no. 21, pp. 4304–4308, 2015.

[78] H. Kunugita, T. Hashimoto, Y. Kiyota, Y. Udagawa, Y. Takeoka, Y. Nakamura, J. Sano, T. Matsushita, T. Kondo, T. Miyasaka, *et al.*, "Excitonic feature in hybrid perovskite $CH_3NH_3PbBr_3$ single crystals", *Chemistry Letters*, vol. 44, no. 6, pp. 852–854, 2015.

[79] T. Ishihara, J. Takahashi, and T. Goto, "Exciton state in two-dimensional perovskite semiconductor $(C_{10}H_{21}NH_3)2PbI_4$", *Solid state communications*, vol. 69, no. 9, pp. 933–936, 1989.

[80] L. Dou, A. B. Wong, Y. Yu, M. Lai, N. Kornienko, S. W. Eaton, A. Fu, C. G. Bischak, J. Ma, T. Ding, *et al.*, "Atomically thin two-dimensional organic-inorganic hybrid perovskites", *Science*, vol. 349, no. 6255, pp. 1518–1521, 2015.

[81] M. C. Gélvez-Rueda, E. M. Hutter, D. H. Cao, N. Renaud, C. C. Stoumpos, J. T. Hupp, T. J. Savenije, M. G. Kanatzidis, and F. C. Grozema, "Interconversion between free charges and bound excitons in 2 D hybrid lead halide perovskites", *The Journal of Physical Chemistry C*, vol. 121, no. 47, pp. 26566–26574, 2017.

[82] B. O. Reagen and M. Grätzel, "A Low-Cost, High-Efficiency Solar Cell Based on Dye-Sensitized Colloidal TiO_2 Films", *Nature*, vol. 353, no. 6346, p. 737, 1991.

[83] F. Di Giacomo, V. Zardetto, A. D'Epifanio, S. Pescetelli, F. Matteocci, S. Razza, A. Di Carlo, S. Licoccia, W. M. Kessels, M. Creatore, *et al.*, "Flexible perovskite photovoltaic modules and solar cells based on atomic layer deposited compact layers and uv-irradiated TiO_2 scaffolds on plastic substrates", *Advanced Energy Materials*, vol. 5, no. 8, p. 1401808, 2015.

[84] A. Fujishima and K. Honda, "Electrochemical Photolysis of Water at a Semiconductor Electrode", *Nature*, vol. 238, pp. 37–38, 1972.

[85] E. Pelizzetti and C. Minero, "Mechanism of the Photo-Oxidative Degradation of Organic Pollutants Over TiO_2 Particles", *Electrochim. Acta*, vol. 38, no. 1, pp. 47–55, 1993.

[86] J. Bai and B. Zhou, "Titanium Dioxide Nanomaterials for Sensor Applications", *Chem. Rev.*, vol. 114, no. 19, pp. 10131–10176, 2014.

[87] E. Baldini, L. Chiodo, A. Dominguez, M. Palummo, S. Moser, M. Yazdi-Rizi, G. Auböck, B. P. Mallett, H. Berger, A. Magrez, *et al.*, "Strongly bound excitons in anatase TiO_2 single crystals and nanoparticles", *Nature communications*, vol. 8, no. 1, p. 13, 2017.

[88] E. Baldini, T. Palmieri, T. Rossi, M. Oppermann, E. Pomarico, G. Auböck, and M. Chergui, "Interfacial Electron Injection Probed by a Substrate-Specific Excitonic Signature", *J. Am. Chem. Soc.*, vol. 139, no. 33, pp. 11584–11589, 2017.

[89] E. Baldini, T. Palmieri, A. Dominguez, P. Ruello, A. Rubio, and M. Chergui, "Phonon-driven selective modulation of exciton oscillator strengths in anatase TiO_2 nanoparticles", *Nano Letters*, vol. 18, no. 8, pp. 5007–5014, 2018.

[90] M. H. Rittmann-Frank, C. J. Milne, J. Rittmann, M. Reinhard, T. J. Penfold, and M. Chergui, "Mapping of the photoinduced electron traps in TiO_2 by picosecond x-ray absorption spectroscopy", *Angewandte Chemie International Edition*, vol. 53, no. 23, pp. 5858–5862, 2014.

[91] F. G. Santomauro, A. Lübcke, J. Rittmann, E. Baldini, A. Ferrer, M. Silatani, P. Zimmermann, S. Grübel, J. A. Johnson, S. O. Mariager, *et al.*, "Femtosecond x-ray absorption study of electron localization in photoexcited anatase TiO_2", *Scientific reports*, vol. 5, p. 14834, 2015.

[92] D. P. Colombo, K. A. Roussel, J. Saeh, D. E. Skinner, J. J. Cavaleri, and R. M. Bowman, "Femtosecond Study of the Intensity Dependence of Electron-Hole Dynamics in TiO_2 Nanoclusters", *Chem. Phys. Lett.*, vol. 232, no. 3, pp. 207–214, 1995.

[93] A. Furube, T. Asahi, H. Masuhara, H. Yamashita, and M. Anpo, "Charge Carrier Dynamics of Standard TiO_2 Catalysts Revealed by Femtosecond Diffuse Reflectance Spectroscopy", *J. Phys. Chem. B*, vol. 103, no. 16, pp. 3120–3127, 1999.

[94] X. Yang and N. Tamai, "How Fast is Interfacial Hole Transfer? In Situ Monitoring of Carrier Dynamics in Anatase TiO_2 Nanoparticles by Femtosecond Laser Spectroscopy", *Phys. Chem. Chem. Phys.*, vol. 3, no. 16, pp. 3393–3398, 2001.

[95] E. Hendry, F. Wang, J. Shan, T. F. Heinz, and M. Bonn, "Electron transport in TiO_2 probed by thz time-domain spectroscopy", *Phys. Rev. B*, vol. 69, no. 8, p. 081101, 2004.

[96] Y. Tamaki, A. Furube, R. Katoh, M. Murai, K. Hara, H. Arakawa, and M. Tachiya, "Trapping Dynamics of Electrons and Holes in a Nanocrystalline TiO_2 Film Revealed by Femtosecond Visible/Near-Infrared Transient Absorption Spectroscopy", *Cr. Chim.*, vol. 9, no. 2, pp. 268–274, 2006.

[97] Y. Tamaki, K. Hara, R. Katoh, M. Tachiya, and A. Furube, "Femtosecond Visible-to-IR Spectroscopy of TiO_2 Nanocrystalline Films: Elucidation of the Electron Mobility before Deep Trapping", *J. Phys. Chem. C*, vol. 113, no. 27, pp. 11741–11746, 2009.

[98] Y. Yamada and Y. Kanemitsu, "Determination of Electron and Hole Lifetimes of Rutile and Anatase TiO_2 Single Crystals", *Appl. Phys. Lett.*, vol. 101, no. 13, p. 133907, 2012.

[99] H. Matsuzaki, Y. Matsui, R. Uchida, H. Yada, T. Terashige, B.-S. Li, A. Sawa, M. Kawasaki, Y. Tokura, and H. Okamoto, "Photocarrier Dynamics in Anatase TiO_2 Investigated by Pump-Probe Absorption Spectroscopy", *Jpn. J. Appl. Phys.*, vol. 115, no. 5, p. 053514, 2014.

[100] V. Zajac, H. Němec, and P. Kužel, "Picosecond Charge Transport in Rutile at High Carrier Densities Studied by Transient Terahertz Spectroscopy", *Phys. Rev. B*, vol. 94, p. 115206, Sep 2016.

[101] F. Nunzi, F. De Angelis, and A. Selloni, "Ab Initio Simulation of the Absorption Spectra of Photoexcited Carriers in TiO_2 Nanoparticles", *J. Phys. Chem. Lett.*, vol. 7, no. 18, pp. 3597–3602, 2016.

[102] P. Zawadzki, "Absorption Spectra of Trapped Holes in Anatase TiO_2", *J. Phys. Chem. C*, vol. 117, no. 17, pp. 8647–8651, 2013.

[103] H. Tang, F. Levy, H. Berger, and P. E. Schmid, "Urbach tail of anatase TiO_2", *Phys. Rev. B*, vol. 52, no. 11, p. 7771, 1995.

[104] N. A. Deskins and M. Dupuis, "Electron Transport via Polaron Hopping in Bulk TiO_2: A Density Functional Theory Characterization", *Phys. Rev. B*, vol. 75, no. 19, p. 195212, 2007.

[105] C. Di Valentin and A. Selloni, "Bulk and Surface Polarons in Photoexcited Anatase TiO_2", *J. Phys. Chem. Lett.*, vol. 2, no. 17, pp. 2223–2228, 2011.

[106] J. Jaćimović, C. Vaju, A. Magrez, H. Berger, L. Forró, R. Gaal, V. Cerovski, and R. Žikić, "Pressure Dependence of the Large-Polaron Transport in Anatase TiO_2 Single Crystals", *EPL Europhys. Lett.*, vol. 99, no. 5, p. 57005, 2012.

[107] S. Moser, L. Moreschini, J. Jaćimović, O. S. Barišić, H. Berger, A. Magrez, Y. J. Chang, K. S. Kim, A. Bostwick, and E. Rotenberg, "Tunable Polaronic Conduction in Anatase TiO_2", *Phys. Rev. Lett.*, vol. 110, no. 19, p. 196403, 2013.

[108] M. Setvin, C. Franchini, X. Hao, M. Schmid, A. Janotti, M. Kaltak, C. G. van de Walle, G. Kresse, and U. Diebold, "Direct View at Excess Electrons in TiO_2 Rutile and Anatase", *Phys. Rev. Lett.*, vol. 113, no. 8, p. 086402, 2014.

[109] V. P. Zhukov and E. V. Chulkov, "*Ab Initio* Calculations of the Electron-Phonon Interaction and Characteristics of Large Polarons in Rutile and Anatase", *Phys. Sol. State*, vol. 56, no. 7, pp. 1302–1309, 2014.

[110] M. Watanabe, S. Sasaki, and T. Hayashi, "Time-Resolved Study of Photoluminescence in Anatase TiO_2", *J. Lumin.*, vol. 87, pp. 1234–1236, 2000.

[111] M. Watanabe and T. Hayashi, "Time-Resolved Study of Self-Trapped Exciton Luminescence in Anatase TiO_2 under Two-Photon Excitation", *J. Lumin.*, vol. 112, no. 1, pp. 88–91, 2005.

[112] K. Wakabayashi, Y. Yamaguchi, T. Sekiya, and S. Kurita, "Time-Resolved Luminescence Spectra in Colorless Anatase TiO_2 Single Crystal", *J. Lumin.*, vol. 112, no. 1, pp. 50–53, 2005.

[113] N. Harada, M. Goto, K. Iijima, H. Sakama, N. Ichikawa, H. Kunugita, and K. Ema, "Time-Resolved Luminescence of TiO_2 Powders with Different Crystal Structures", *Jap. J. Appl. Phys.*, vol. 46, no. 7R, p. 4170, 2007.

[114] L. Cavigli, F. Bogani, A. Vinattieri, V. Faso, and G. Baldi, "Volume versus Surface-Mediated Recombination in Anatase TiO_2 Nanoparticles", *J. Appl. Phys.*, vol. 106, no. 5, p. 053516, 2009.

[115] L. Cavigli, F. Bogani, A. Vinattieri, L. Cortese, M. Colocci, V. Faso, and G. Baldi, "Carrier Recombination Dynamics in Anatase TiO_2 Nanoparticles", *Solid State Sciences*, vol. 12, no. 11, pp. 1877–1880, 2010.

[116] R. Gonzales, R. Zallen, and H. Berger, "Infrared reflectivity and lattice fundamentals in anatase TiO_2", *Phys. Rev. B*, vol. 55, no. 11, pp. 7014–7, 1997.

[117] S. Roberts, "Dielectric constants and polarizabilities of ions in simple crystals and barium titanate", *Physical Review*, vol. 76, no. 8, p. 1215, 1949.

[118] H. Haug and S. Schmitt-Rink, "Basic Mechanisms of the Optical Nonlinearities of Semiconductors Near the Band Edge", *JOSA B*, vol. 2, no. 7, pp. 1135–1142, 1985.

[119] S. Schmitt-Rink, D. S. Chemla, and D. A. B. Miller, "Linear and Nonlinear Optical Properties of Semiconductor Quantum Wells", *Adv. Phys.*, vol. 38, no. 2, pp. 89–188, 1989.

[120] E. Baldini, A. Mann, S. Borroni, C. Arrell, F. van Mourik, and F. Carbone, "A versatile setup for ultrafast broadband optical spectroscopy of coherent collective modes in strongly correlated quantum systems", *Structural Dynamics*, vol. 3, no. 6, 2016.

[121] S. Borroni, E. Baldini, V. M. Katukuri, A. Mann, K. Parlinski, D. Legut, C. Arrell, F. van Mourik, J. Teyssier, A. Kozlowski, *et al.*, "Coherent generation of symmetry-forbidden phonons by light-induced electron-phonon interactions in magnetite", *Physical Review B*, vol. 96, no. 10, p. 104308, 2017.

[122] A. Mann, E. Baldini, A. Odeh, A. Magrez, H. Berger, and F. Carbone, "Probing the coupling between a doublon excitation and the charge-density wave in TaS_2 by ultrafast optical spectroscopy", *Physical Review B*, vol. 94, no. 11, p. 115122, 2016.

[123] E. Baldini, A. Mann, B. P. Mallett, C. Arrell, F. Van Mourik, T. Wolf, D. Mihailovic, J. L. Tallon, C. Bernhard, J. Lorenzana, *et al.*, "Clocking the onset of bilayer coherence in a high-t c cuprate", *Physical Review B*, vol. 95, no. 2, p. 024501, 2017.

[124] E. Baldini, A. Mann, L. Benfatto, E. Cappelluti, A. Acocella, V. M. Silkin, S. V. Eremeev, A. B. Kuzmenko, S. Borroni, T. Tan, *et al.*, "Real-time observation of phonon-mediated σ- π interband scattering in MgB_2", *Physical review letters*, vol. 119, no. 9, p. 097002, 2017.

[125] M. Oppermann, N. S. Nagornova, A. Oriana, E. Baldini, L. Mewes, B. Bauer, T. Palmieri, T. Rossi, F. Van Mourik, and M. Chergui, "The louvre laboratory: state-of-the-art ultrafast ultraviolet spectroscopies for molecular and materials science", *CHIMIA International Journal for Chemistry*, vol. 71, no. 5, pp. 288–294, 2017.

[126] G. Auböck, C. Consani, F. van Mourik, and M. Chergui, "Ultrabroadband Femtosecond Two-Dimensional Ultraviolet Transient Absorption", *Opt. Lett.*, vol. 37, no. 12, pp. 2337–2339, 2012.

[127] G. Auböck, C. Consani, R. Monni, A. Cannizzo, F. Van Mourik, and M. Chergui, "Femtosecond pump/supercontinuum-probe setup with 20 khz repetition rate", *Review of Scientific Instruments*, vol. 83, no. 9, p. 093105, 2012.

[128] E. Baldini, *Nonequilibrium Dynamics of Collective Excitations in Quantum Materials.* Springer, 2018.

[129] M. Kollár, L. Ćirić, J. H. Dil, A. Weber, S. Muff, H. M. Ronnow, B. Náfrádi, B. P. Monnier, J. S. Luterbacher, L. Forró, and E. Horváth, "Clean, cleaved surfaces of the photovoltaic perovskite", *Scientific Reports*, vol. 7, no. 1, p. 695, 2017.

[130] H. Berger, H. Tang, and F. Lévy, "Growth and Raman Spectroscopic Characterization of TiO_2 Anatase Single Crystals", *J. Cryst. Growth*, vol. 130, no. 1-2, pp. 108–112, 1993.

[131] G. Mahan, "Excitons in degenerate semiconductors", *Physical Review*, vol. 153, no. 3, p. 882, 1967.

[132] H. Kalt, K. Leo, R. Cingolani, and K. Ploog, "Fermi-edge singularity in heavily doped gaas multiple quantum wells", *Physical Review B*, vol. 40, no. 17, p. 12017, 1989.

[133] P. Grivickas, V. Grivickas, and J. Linnros, "Excitonic absorption above the mott transition in si", *Physical review letters*, vol. 91, no. 24, p. 246401, 2003.

[134] A. Schleife, C. Rödl, F. Fuchs, K. Hannewald, and F. Bechstedt, "Optical absorption in degenerately doped semiconductors: Mott transition or Mahan excitons?", *Physical review letters*, vol. 107, no. 23, p. 236405, 2011.

[135] J. S. Manser and P. V. Kamat, "Band filling with free charge carriers in organometal halide perovskites", *Nature Photonics*, vol. 8, no. 9, pp. 737–743, 2014.

[136] D. A. Valverde-Chávez, C. S. Ponseca, C. C. Stoumpos, A. Yartsev, M. G. Kanatzidis, V. Sundström, and D. G. Cooke, "Intrinsic femtosecond charge generation dynamics in single crystal $CH_3NH_3PbI_3$", *Energy & Environmental Science*, vol. 8, no. 12, pp. 3700–3707, 2015.

[137] Y. Yang, Y. Yan, M. Yang, S. Choi, K. Zhu, J. M. Luther, and M. C. Beard, "Low surface recombination velocity in solution-grown $CH_3NH_3PbBr_3$ perovskite single crystal", *Nature communications*, vol. 6, p. 7961, 2015.

[138] B. Wenger, P. K. Nayak, X. Wen, S. V. Kesava, N. K. Noel, and H. J. Snaith, "Consolidation of the optoelectronic properties of ch 3 nh 3 pbbr 3 perovskite single crystals", *Nature communications*, vol. 8, no. 1, p. 590, 2017.

[139] A. D. Wright, C. Verdi, R. L. Milot, G. E. Eperon, M. A. Pérez-Osorio, H. J. Snaith, F. Giustino, M. B. Johnston, and L. M. Herz, "Electron–phonon coupling in hybrid lead halide perovskites", *Nature communications*, vol. 7, p. 11755, 2016.

[140] N. Onoda-Yamamuro, T. Matsuo, and H. Suga, "Dielectric study of ceCH3NH3PbX3 (X= Cl, Br, I)", *Journal of Physics and Chemistry of Solids*, vol. 53, no. 7, pp. 935–939, 1992.

[141] D. Semkat, F. Richter, D. Kremp, G. Manzke, W.-D. Kraeft, and K. Henneberger, "Ionization equilibrium in an excited semiconductor: Mott transition versus Bose-Einstein condensation", *Physical Review B*, vol. 80, no. 15, p. 155201, 2009.

[142] G. Jellison Jr, V. Merkulov, A. Puretzky, D. Geohegan, G. Eres, D. Lowndes, and J. Caughman, "Characterization of thin-film amorphous semiconductors using spectroscopic ellipsometry", *Thin Solid Films*, vol. 377, pp. 68–73, 2000.

[143] F. Jahnke, M. Kira, and S. Koch, "Linear and nonlinear optical properties of excitons in semiconductor quantum wells and microcavities", *Zeitschrift für Physik B Condensed Matter*, vol. 104, no. 3, pp. 559–572, 1997.

[144] W. Schäfer and M. Wegener, *Semiconductor optics and transport phenomena.* Springer Science & Business Media, 2013.

[145] G. Manzke, T. Klähn, and K. Henneberger, "Quantum kinetics and linear optical response of semiconductors", *physica status solidi (c)*, no. 5, pp. 1480–1483, 2003.

[146] F. Sekiguchi and R. Shimano, "Excitonic correlation in the Mott crossover regime in Ge", *Physical Review B*, vol. 91, no. 15, p. 155202, 2015.

[147] S. Chatterjee, C. Ell, S. Mosor, G. Khitrova, H. Gibbs, W. Hoyer, M. Kira, S. Koch, J. Prineas, and H. Stolz, "Excitonic photoluminescence in semiconductor quantum wells: Plasma versus excitons", *Physical review letters*, vol. 92, no. 6, p. 067402, 2004.

[148] P. Maity, O. F. Mohammed, K. Katsiev, and H. Idriss, "Study of the bulk charge carrier dynamics in anatase and rutile TiO_2 single crystals by femtosecond time-resolved spectroscopy", *The Journal of Physical Chemistry C*, vol. 122, no. 16, pp. 8925–8932, 2018.

[149] W. Brütting, *Introduction to the Physics of Organic Semiconductors.* Wiley Online Library, 2006.

[150] J. R. Schaibley, H. Yu, G. Clark, P. Rivera, J. S. Ross, K. L. Seyler, W. Yao, and X. Xu, "Valleytronics in 2D materials", *Nat. Rev. Mat.*, vol. 1, p. 16055, 2016.

[151] C. Klingshirn, R. Hauschild, J. Fallert, and H. Kalt, "Room-Temperature Stimulated Emission of ZnO: Alternatives to Excitonic Lasing", *Phys. Rev. B*, vol. 75, p. 115203, Mar 2007.

[152] P. K. Gogoi, L. Sponza, D. Schmidt, T. C. Asmara, C. Diao, J. C. Lim, S. M. Poh, S.-i. Kimura, P. E. Trevisanutto, V. Olevano, *et al.*, "Anomalous Excitons and Screenings Unveiling Strong Electronic Correlations in $SrTi_{1-x}Nb_xO_3$ ($0 \leq x \leq 0.005$)", *Phys. Rev. B*, vol. 92, no. 3, p. 035119, 2015.

[153] Y. Toyozawa, *Optical Processes in Solids.* Cambridge University Press, 2003.

[154] K. S. Song and R. T. Williams, *Self-Trapped Excitons*, vol. 105. Springer Science & Business Media, 2013.

[155] R. Merlin, "Generating Coherent THz Phonons with Light Pulses", *Sol. State Comm.*, vol. 102, no. 2, pp. 207–220, 1997.

[156] P. Ruello and V. E. Gusev, "Physical Mechanisms of Coherent Acoustic Phonons Generation by Ultrafast Laser Action", *Ultrasonics*, vol. 56, pp. 21–35, 2015.

[157] A. Mann, E. Baldini, A. Tramontana, E. Pomjakushina, K. Conder, C. Arrell, F. Van Mourik, J. Lorenzana, and F. Carbone, "Probing the Electron-Phonon Interaction in Correlated Systems with Coherent Lattice Fluctuation Spectroscopy", *Phys. Rev. B*, vol. 92, no. 3, p. 035147, 2015.

[158] A. Yamamoto, T. Mishina, Y. Masumoto, and M. Nakayama, "Coherent Oscillation of Zone-Folded Phonon Modes in GaAs-AlAs Superlattices", *Phys. Rev. Lett.*, vol. 73, no. 5, p. 740, 1994.

[159] G. Cerullo, S. De Silvestri, and U. Banin, "Size-Dependent Dynamics of Coherent Acoustic Phonons in Nanocrystal Quantum Dots", *Phys. Rev. B*, vol. 60, no. 3, p. 1928, 1999.

[160] P. Tyagi, R. R. Cooney, S. L. Sewall, D. M. Sagar, J. I. Saari, and P. Kambhampati, "Controlling Piezoelectric Response in Semiconductor Quantum Dots via Impulsive Charge Localization", *Nano Lett.*, vol. 10, no. 8, pp. 3062–3067, 2010.

[161] L. Dworak, V. Matylitsky, M. Braun, and J. Wachtveitl, "Coherent Longitudinal-Optical Ground-State Phonon in CdSe Quantum Dots Triggered by Ultrafast Charge Migration", *Phys. Rev. Lett.*, vol. 107, no. 24, p. 247401, 2011.

[162] S. Ge, X. Liu, X. Qiao, Q. Wang, Z. Xu, J. Qiu, P.-H. Tan, J. Zhao, and D. Sun, "Coherent Longitudinal Acoustic Phonon Approaching THz Frequency in Multilayer Molybdenum Disulphide", *Sci. Rep.*, vol. 4, 2014.

[163] A. A. Bakulin, S. E. Morgan, T. B. Kehoe, M. W. Wilson, A. W. Chin, D. Zigmantas, D. Egorova, and A. Rao, "Real-Time Observation of Multiexcitonic States in Ultrafast Singlet Fission Using Coherent 2D Electronic Spectroscopy", *Nat. Chem.*, vol. 8, no. 1, pp. 16–23, 2016.

[164] A. V. Akimov, A. V. Scherbakov, D. R. Yakovlev, C. T. Foxon, and M. Bayer, "Ultrafast Band-Gap Shift Induced by a Strain Pulse in Semiconductor Heterostructures", *Phys. Rev. Lett.*, vol. 97, no. 3, p. 037401, 2006.

[165] A. V. Scherbakov, P. J. S. Van Capel, A. V. Akimov, J. I. Dijkhuis, D. R. Yakovlev, T. Berstermann, and M. Bayer, "Chirping of an Optical Transition by an Ultrafast Acoustic Soliton Train in a Semiconductor Quantum Well", *Phys. Rev. Lett.*, vol. 99, no. 5, p. 057402, 2007.

[166] D. M. Sagar, R. R. Cooney, S. L. Sewall, E. A. Dias, M. M. Barsan, I. S. Butler, and P. Kambhampati, "Size Dependent, State-Resolved Studies of Exciton-Phonon Couplings in Strongly Confined Semiconductor Quantum Dots", *Phys. Rev. B*, vol. 77, no. 23, p. 235321, 2008.

[167] M. Setvin, C. Franchini, X. Hao, M. Schmid, A. Janotti, M. Kaltak, C. G. Van de Walle, G. Kresse, and U. Diebold, "Direct View at Excess Electrons in TiO_2 Rutile and Anatase", *Phys. Rev. Lett.*, vol. 113, no. 8, p. 086402, 2014.

[168] E. Portuondo-Campa, A. Tortschanoff, F. van Mourik, and M. Chergui, "Ultrafast Nonresonant Response of TiO_2 Nanostructured Films", *J. Chem. Phys.*, vol. 128, no. 24, p. 244718, 2008.

[169] K. Ishioka and H. Petek, "Raman Generation of Coherent Phonons of Anatase and Rutile TiO_2 Photoexcited at Fundamental Absorption Edges", *Phys. Rev. B*, vol. 86, no. 20, p. 205201, 2012.

[170] C.-K. Sun, J.-C. Liang, and X.-Y. Yu, "Coherent Acoustic Phonon Oscillations in Semiconductor Multiple Quantum Wells with Piezoelectric Fields", *Phys. Rev. Lett.*, vol. 84, no. 1, p. 179, 2000.

[171] A. Devos, F. Poinsotte, J. Groenen, O. Dehaese, N. Bertru, and A. Ponchet, "Strong Generation of Coherent Acoustic Phonons in Semiconductor Quantum Dots", *Phys. Rev. Lett.*, vol. 98, no. 20, p. 207402, 2007.

[172] J. A. Gupta, R. Knobel, N. Samarth, and D. D. Awschalom, "Ultrafast Manipulation of Electron Spin Coherence", *Science*, vol. 292, no. 5526, pp. 2458–2461, 2001.

[173] J. Kim, X. Hong, C. Jin, S.-F. Shi, C.-Y. S. Chang, M.-H. Chiu, L.-J. Li, and F. Wang, "Ultrafast Generation of Pseudo-Magnetic Field for Valley Excitons in WSe_2 Monolayers", *Science*, vol. 346, no. 6214, pp. 1205–1208, 2014.

[174] E. J. Sie, J. W. McIver, Y. H. Lee, L. Fu, J. Kong, and N. Gedik, "Valley-Selective Optical Stark Effect in Monolayer WS_2", *Nat. Mat.*, vol. 14, no. 3, pp. 290–294, 2015.

[175] Y. Yang, M. Yang, K. Zhu, J. C. Johnson, J. J. Berry, J. Van De Lagemaat, and M. C. Beard, "Large Polarization-Dependent Exciton Optical Stark Effect in Lead Iodide Perovskites", *Nat. Comm.*, vol. 7, p. 12613, 2016.

[176] L. Brillouin, "Diffusion de la Lumière et des Rayons X par un Corps Transparent Homogène. Influence de l'Agitation Thermique", *Ann. Phys.(Paris)*, vol. 17, no. 88-122, p. 21, 1922.

[177] C. Thomsen, H. T. Grahn, H. J. Maris, and J. Tauc, "Surface Generation and Detection of Phonons by Picosecond Light Pulses", *Phys. Rev. B*, vol. 34, no. 6, p. 4129, 1986.

[178] E. Baldini, A. Dominguez, L. Chiodo, E. Sheveleva, M. Yazdi-Rizi, C. Bernhard, A. Rubio, and M. Chergui, "Anomalous Anisotropic Exciton Temperature Dependence in Rutile TiO_2", *Phys. Rev. B*, vol. 96, p. 041204, Jul 2017.

[179] L. Hedin, "New Method for Calculating the One-Particle Green's Function with Application to the Electron-Gas Problem", *Phys. Rev.*, vol. 139, no. 3A, p. A796, 1965.

[180] G. Onida, L. Reining, and A. Rubio, "Electronic Excitations: Density-Functional Versus Many-Body Green's-Function Approaches", *Rev. Mod. Phys.*, vol. 74, no. 2, p. 601, 2002.

[181] W.-J. Yin, S. Chen, J.-H. Yang, X.-G. Gong, Y. Yan, and S.-H. Wei, "Effective Band Gap Narrowing of Anatase TiO_2 by Strain Along a Soft Crystal Direction", *Appl. Phys. Lett.*, vol. 96, no. 22, p. 221901, 2010.

[182] A. Bojahr, M. Herzog, D. Schick, I. Vrejoiu, and M. Bargheer, "Calibrated Real-Time Detection of Nonlinearly Propagating Strain Waves", *Phys. Rev. B*, vol. 86, no. 14, p. 144306, 2012.

[183] K. F. MacDonald, Z. L. Sámson, M. I. Stockman, and N. I. Zheludev, "Ultrafast Active Plasmonics", *Nat. Phot.*, vol. 3, no. 1, pp. 55–58, 2009.

[184] A. Steinhoff, M. Florian, M. Rösner, G. Schönhoff, T. O. Wehling, and F. Jahnke, "Exciton fission in monolayer transition metal dichalcogenide semiconductors", *Nature communications*, vol. 8, no. 1, p. 1166, 2017.

[185] D. Kremp, W. Kraeft, and A. Lambert, "Equation of state and ionization equilibrium for nonideal plasmas", *Physica A Statistical Mechanics and its Applications*, vol. 127, pp. 72–86, 1984.

[186] H. Stolz and R. Zimmermann, "Correlated pairs and a mass action law in two-component fermi systems excitons in an electron-hole plasma", *physica status solidi (b)*, vol. 94, no. 1, pp. 135–146, 1979.

[187] M. Schlanges, M. Bonitz, and A. Tschttschjan, "Plasma phase transition in fluid hydrogen-helium mixtures", *Contributions to Plasma Physics*, vol. 35, no. 2, pp. 109–125, 1995.

[188] D. Kremp, M. Schlanges, and W.-D. Kraeft, *Quantum statistics of nonideal plasmas*, vol. 25. Springer Science & Business Media, 2006.

[189] G. Strinati, "Effects of dynamical screening on resonances at inner-shell thresholds in semiconductors", *Physical Review B*, vol. 29, no. 10, p. 5718, 1984.

[190] T. Bornath, M. Schlanges, P. Hilse, and D. Kremp, "Nonlinear collisional absorption in dense laser plasmas", *Physical Review E*, vol. 64, no. 2, p. 026414, 2001.

[191] J. Deslippe, G. Samsonidze, D. A. Strubbe, M. Jain, M. L. Cohen, and S. G. Louie, "BerkeleyGW: A Massively Parallel Computer Package for the Calculation of the Quasiparticle and Optical Properties of Materials and Nanostructures", *Comput. Phys. Commun.*, vol. 183, no. 6, pp. 1269–1289, 2012.

[192] A. M. Rappe, K. M. Rabe, E. Kaxiras, and J. D. Joannopoulos, "Optimized Pseudopotentials", *Phys. Rev. B*, vol. 41, no. 2, p. 1227, 1990.

[193] K. V. K. Rao, S. V. N. Naidu, and L. Iyengar, "Thermal Expansion of Rutile and Anatase", *J. Am. Ceram. Soc.*, vol. 53, no. 3, pp. 124–126, 1970.

Tania Palmieri

Rue de la Pontaise 25, 1018 Lausanne (CH) | +41787138246 | tania.palmieri@alumni.epfl.ch

Education

2018	**PhD in Photonics,** École Polytechnique Fédérale de Lausanne (EPFL), Switzerland Laboratory of Ultrafast Spectroscopy
2014	**Master's degree in Bioengineering,** EPFL, Switzerland Minor in Biomedical Technologies, specialization in biophotonics and bioimaging Graduated with *mention of excellence* (5.52/6)
2012	**Bachelor's degree in Bioengineering,** University of Pavia, Italy Graduated *cum laude (110/110)*

Experience

Nov '14 – now	**Doctoral assistant - Laboratory of Ultrafast Spectroscopy, EPFL** "Nonequilibrium exciton physics in hybrid lead-halide perovskites and TiO_2" - Measurement and interpretation of time-resolved absorption/reflectivity spectra of single crystals, thin films and nanoparticles of semiconductors (hybrid organic-inorganic perovskites and titanium dioxide). - Maintenance of and optimization of an ultrafast fluorescence up-conversion setup. - Developed a software/GUI for laser lab automation and CCD data acquisition.
Feb '17 – now	**Vice-President (2017), President (2018) - EPFL Photonics Chapter (OSA/SPIE)** Coordinator of the photonics student association at EPFL. Direction and co-organization of academic talks, career development events, large-scale industry events, outreach, recruitment, and social/networking events on monthly basis. Organizer of the Swissphotonics workshops held at Forum EPFL.
Feb '14 – Jul '14	**Master thesis - Laboratory of Nanoscale Biology, EPFL** "Investigation of the electro-osmotic flow from glass nanocapillaries using optical trapping" - Optimization of the electron-beam lithography for the fabrication of birefringent nanostructures and fabrication/shaping of glass nanocapillaries with SEM - Preparation and characterization of PDMS microfluidic cells for conductance measurements. - Measure of the nanostructures by recording change in light polarization with optical tweezer setup.
Sep '13 – Jan '14	**Trainee - Laboratory of Optics, EPFL** Investigation and manipulation of chloroplasts movement in response to light.
Jul '13 – Sep '13	**R&D Internship - Bright Solutions SRL (Pavia, Italy)** Development of a long-range autocorrelator for measurement of ultra-short laser pulses.
Feb '13 – Jul '13	**Trainee - Laboratory of Life Science Electronics, EPFL** Fabrication of SU-8 micropillars for impedance-based microfluidic biosensors
Feb '12 – Jul '12	**Master Thesis - Laboratory of Quantum Electronics and Nonlinear Optics, University of Pavia (Italy)** "Design of an optical system for Low Level Laser Therapy and in-vitro effects of irradiation on human osteoblast-like cells growth".

Awards and Grants

2015	**Photonics Day Award** - First Prize for the best Flash Presentation in 180 seconds, EPFL
2014	**Mention of Academic Excellence** - for outstanding academic records for the Master studies, EPFL
2012, 2013	**Excellence Fellowship** - awarded to applicants with outstanding academic records, EPFL

Teaching activities

2014 - 2018	**Teaching assistant of "General Physics I-II", "Atoms and Radiations", "Solid State Physics I"** Section of Physics, EPFL
2013 - 2014	**Teaching assistant of "Biomedical optics"** Section of Life Sciences and Technologies, EPFL
2011 - 2012	**Teaching assistant of "Physics" and "Electronics"** Engineering Faculty, University of Pavia (Italy).

Technical Skills

Experimental	Excellent skills in multidimensional data analysis, signal and image processing; Extensive expertise in optics (femotosecond laser systems, Ti:Sapphire oscillators, regenerative amplifiers, nonlinear optics, static and time-resolved UV-VIS spectroscopy, wide-field and confocal microscopy, ellipsometry, optical trapping) Experience in characterizing optical and electronic properties of materials.
Cleanroom	Photolithography, e-beam lithography, wet and dry etching, metal evaporation, PDMS microchannels fabrication, scanning electron microscope (SEM).
IT	Advanced user of MATLAB (>10 yrs), Igor PRO (>5 yrs). Very good knowledge of C, C++, LabWindows/CVI, Image J, LaTex, Adobe llustrator, SQL, MS Office, Adobe Illustrator, Latex. Good knowledge of Python, Labview, Origin.

Languages

English	Fluent spoken (C1) and written (C2)
French	Fluent spoken and written (C1)
German	Basic knowledge (A2)
Italian	Native

Personal information

Born on 21st April 1990 (28 years) in Modugno (Bari), Italy.
Italian citizenship, Swiss B permit, driving licence.

Beyond my passion for science and outreach, I am fund of art-house cinemas, little-attended music concerts and charcoal pencils. I am an excellent cook (traditional Italian cuisine) and give my best in baking cakes. After moving to Switzerland, I discovered myself to be a passionate skier, climber and mountain hiker.

Academic records

Journals	T. Palmieri†, E. Baldini†, A. Steinhoff, A. Akrap, M. Kollar, E. Horvath, F. Jahnke, M. Chergui, "Mahan Excitons in Room-Temperature Methylammonium Lead Bromide Perovskites" - Submitted to Science.
	E. Baldini, A. Dominguez, T. Palmieri, O. Cannelli, A. Rubio, P. Ruello, M. Chergui, "Exciton Control in a Room-Temperature Bulk Semiconductor with Coherent Strain Pulses" -arxiv.org/abs/1803.07666 – Submitted to Nature Communications.
	E. Baldini, T. Palmieri, A. Dominguez, P. Ruello, A. Rubio, M. Chergui, "Phonon-Driven Selective Modulation of Exciton Oscillator Strengths in Anatase TiO_2 Nanoparticles", Nano Letters 18, 5007-5014 (2018).
	E. Baldini, T. Palmieri, E. Pomarico, G. Auböck, M. Chergui, "Clocking the Ultrafast Electron Cooling in Anatase Titanium Dioxide Nanoparticles", ACS Photonics 5, 1241-1249 (2018)
	E. Baldini, T. Palmieri, T. Rossi, M. Oppermann, E. Pomarico, G. Auböck, M. Chergui, "Ultrafast Interfacial Electron Injection Probed by a Substrate-Specific Excitonic Signature", Journal of American Chemical Society 139, 11584-11589 (2017)
	M. Oppermann, N. S. Nagornova, A. Oriana, E. Baldini, L. Mewes, B. Bauer, T. Palmieri, T. Rossi, F. van Mourik, M. Chergui, "The LOUVRE Laboratory: State-of-the-Art Ultrafast Ultraviolet Spectroscopies for Molecular and Materials Science", CHIMIA International Journal for Chemistry 71, 5, 288-294 (2017)
Proceedings	E. Baldini, T. Palmieri, E. Pomarico, G. Auböck, M. Chergui "Electron Dynamics in Anatase TiO_2 Nanoparticles by Ultrafast Broadband Deep-Ultraviolet Spectroscopy", Proceedings of the XXIst International Conference on Ultrafast Phenomena (2018).
Unpublished work	E. Baldini†, T. Palmieri†, A. Dominguez, P. Narang, A. Rubio, M. Chergui, "Exciton renormalization dynamics in Highly Photoexcited Anatase TiO_2".
	T. Palmieri, E. Baldini, M. Chergui, "Ultrafast Optical Nonlinearities and Many-Body Dynamics in $CsPbX_3$ Nanocrystals".
	E. Baldini, T. Palmieri, M. Chergui, "Fate of the Excitonic States in Amorphous TiO2 Nanoparticles".
Oral presentations	XXI International Conference on Ultrafast Phenomena (Hamburg, 2018)
	Annual meeting of the Swiss Physical Society (Lausanne, 2018)

Ce document a été imprimé au Centre d'impression EPFL,
imprimerie climatiquement neutre, certifiée myClimate.